5-2014

Bridging the Nano- and Macro-Worlds: Thermal Property Measurement Using Thermal Microscopy and Photothermal Radiometry – Application to Particle-Irradiation Damage Profile in Zirconium Carbide

Colby Bruce Jensen
Utah State University

Recommended Citation

Jensen, Colby Bruce, "Bridging the Nano- and Macro-Worlds: Thermal Property Measurement Using Thermal Microscopy and Photothermal Radiometry – Application to Particle-Irradiation Damage Profile in Zirconium Carbide" (2014). *All Graduate Theses and Dissertations*. 3105.
https://digitalcommons.usu.edu/etd/3105

BRIDGING THE NANO- AND MACRO-WORLDS: THERMAL PROPERTY MEASUREMENT USING THERMAL MICROSCOPY AND PHOTOTHERMAL RADIOMETRY – APPLICATION TO PARTICLE-IRRADIATION DAMAGE PROFILE IN ZRC

by

Colby Bruce Jensen

A dissertation submitted in partial fulfillment
of the requirements for the degree

of

DOCTOR OF PHILOSOPHY

in

Mechanical Engineering

Approved:

Dr. Heng Ban Major Professor	Dr. Mihai Chirtoc Committee Member
Dr. Byard Wood Committee Member	Dr. Sebastian Volz Committee Member
Dr. Stephen Bialkowski Committee Member	Dr. Jean Ebothé Committee Member

Dr. Mark R. McLellan
Vice President for Research and
Dean of the School of Graduate Studies

UTAH STATE UNIVERSITY
Logan, Utah

2014

ABSTRACT

Bridging the Nano- and Macro-Worlds: Thermal Property Measurement Using Thermal Microscopy and Photothermal Radiometry – Application to Particle-Irradiation Damage Profile in Zirconium Carbide

by

Colby Bruce Jensen, Doctor of Philosophy

Utah State University, 2014

Major Professor: Dr. Heng Ban
Department: Mechanical and Aerospace Engineering
Co-Major Professor: Dr. Mihai Chirtoc
University: Université de Reims Champagne-Ardenne, Reims, France

Multiscaled experimental investigations of heat transfer from nanoscales to macroscales are requisite to progress in energy technologies. In nuclear applications, material properties can undergo significant alteration due to destructive interaction with irradiating particles at microstructural levels that affect bulk properties. Correlating material microstructure to bulk material properties remains a crucial hurdle for obtaining first-principles-based, full-scale material property predictive capability. Ion-irradiated material studies provide valuable insight into material behavior under irradiation conditions that can be correlated to neutron irradiation effects. Through such studies, the need of costly (money and time) studies of neutron interaction with materials can be mitigated significantly. One of the challenges associated with studies of ion-irradiated materials is that the affected layer, or penetration depth, is typically very thin (~0.1-100μm for laboratory accelerators). Few investigations have been reported of ion-irradiation effects on thermal transport properties, in part, due to the challenge associated with measurements at the spatial scales of the zones of interest.

This study expands the current knowledge base regarding thermal transport in ion-irradiated materials through the use of a multiscaled experimental approach using thermal wave methods. In a manner not previously explored, four thermal wave methods are used to characterize the proton-irradiated layer in ZrC including scanning thermal microscopy, spatial-scanning front-detection photothermal radiometry (PTR), lock-in IR thermography (lock-in IRT), and tomographic, frequency-based PTR. For the first time, the in-depth thermal conductivity profile of an ion-irradiated sample is measured directly. The profiles obtained by each of the spatial scanning methods are compared to each other and the numerical prediction of the ion-damage profile. The complementary nature of the various techniques validates the measured profile and the measured degradation of thermal conductivity in the ZrC sample showing the viability of such complementary studies.

(140 pages)

PUBLIC ABSTRACT

Bridging the Nano- and Macro-Worlds: Thermal Property Measurement Using Thermal Microscopy and Photothermal Radiometry – Application to Particle-Irradiation Damage Profile in Zirconium Carbide

by

Colby Bruce Jensen, Doctor of Philosophy

Utah State University, 2014

Major Professor: Dr. Heng Ban
Department: Mechanical and Aerospace Engineering
Co-Major Professor: Dr. Mihai Chirtoc
University: Université de Reims Champagne-Ardenne, Reims, France

Multiscaled experimental investigations of heat transfer from nanoscales to macroscales are requisite to progress in energy technologies. In nuclear applications, material properties can undergo significant alteration due to destructive interaction with irradiating particles at microstructural levels that affect bulk properties. This study expands the current knowledge base regarding thermal transport in ion-irradiated materials through the use of a multiscaled experimental approach using four complementary thermal wave methods. For the first time, the in-depth thermal conductivity profile of an ion-irradiated sample is measured directly.

ACKNOWLEDGMENTS

Acknowledging all who have in some way contributed to my work over the past several years is no easy task and certainly a few words does little to acknowledge their help or to fully express my gratitude. I had no foresight of the path I would take, both rich and diverse in experiences: with people, in the laboratory, and of travels.

Firstly, my deepest and sincerest gratitude is extended to my two major professors and mentors, Dr. Heng Ban and Prof. Mihai Chirtoc. It has been a privilege to have the opportunity to work with professionals of their caliber. What I have gained from them goes well beyond the laboratory in molding my goals and aspirations. I cannot overstate their beneficial and lasting influence on my life.

I recognize and express appreciation for the sources of funding for my work, which was provided through a Nuclear Energy University Program Graduate Fellowship, the Chateaubriand Fellowship from the Embassy of France in the U.S., and an NSF International Travel Fellowship from the International Center for Materials Research.

I am grateful to many kind faculty who have provided example, support, criticism, expertise, and guidance along the way: from the USA – Dr. Byard Wood, from France – Jean-Stéphane Antoniow and Nicolas Horny; from Poland – Prof. Jerzy Bodzenta and Anna Kaźmierczak-Bałata; as well as all other dissertation committee members, and many others (too many to list) from the three institutions that have been my host during my PhD studies.

I feel very fortunate to have worked with many extraordinary friends and colleagues in the laboratory. Those deserving of special acknowledgment for my work include: Changhu Xing, Charlie Folsom, Austin Fleming, and Zilong Hua.

Finally, I owe all that I am and all that I have accomplished to my family. The unconditional love and support of good parents is an immeasurable blessing in my life. Most

especially, I acknowledge the innumerable sacrifices made by my wife, Penny, who has carried far more than her fair share of parenting and household responsibilities through these years. Her patience, support, and companionship have been key to achieving this goal. My boys are my inspiration to keep moving forward.

Colby Bruce Jensen

CONTENTS

LIST OF TABLES

LIST OF FIGURES

ACRONYMS

AC	alternating current
AFM	atomic force microscopy
AOM	acousto-optical modulator
BD-PTR	back-detection-photothermal radiometry
DC	direct current
FD-PTR	front-detection-photothermal radiometry
IR	infrared
IRT	infrared thermography
MOR	modulated optical reflectance
NDT	non-destructive technique
PA	photoacoustic spectroscopy
PBD	photothermal beam deflection
PKA	primary knock-on atom
PPE	photopyroelectric
PTD	photothermal displacement
PTR	photothermal radiometry
SPM	scanning probe microscopy
SThEM	scanning thermal expansion microscopy
SThM	scanning thermal microscopy
STM	scanning tunneling microscopy
SUT	Silesian University of Technology, Gliwice, Poland
TEM	transmission electron microscopy
TRIM	transport of ions in matter

TRISO	tri-structural isotropic
URCA	Université de Reims Champagne-Ardenne, Reims, France
USU	Utah State University, Logan, Utah, USA
ZrC	zirconium carbide

NOMENCLATURE

a_c	SThM probe physical contact radius with sample, [m]
A	”11” position in quadrupole matrix of a plane wall
Amp	Generic amplitude
b	Thermal exchange radius for SThM probe, [m]
B	”12” position in quadrupole matrix of a plane wall
C	”21” position in quadrupole matrix of a plane wall
c_p	Specific heat capacity at constant pressure, [$J\cdot kg^{-1}\cdot K^{-1}$]
C_p	Volumetric heat capacity, [$J\cdot m^{-3}$]
D	”22” position in quadrupole matrix of a plane wall
e	Thermal effusivity, [$J\cdot m^{-2}\cdot K^{-1}\cdot s^{-1/2}$]
E_D	Threshold displacement energy, [J or eV]
f	Frequency, [Hz]
f_T	Transition frequency for thermal thin-thick, [Hz]
F	Generic function
G	Tip-sample thermal conductance, [W/K]
G_g	Tip-sample thermal conductance through surrounding gas, [W/K]
G_{Pt}	Thermal conductance of one PtRh leg of wire probe, [W/K]
h	Heat transfer coefficient, [$W\cdot m^{-2}\cdot K^{-1}$]
i_ω	Frequency modulated current, [A]
I_0	Heating flux intensity, [$W\cdot m^{-2}$]

Lz	Lorenz constant, [W·Ω·K^{-2}]
L	Thickness of a homogeneous sample, [m]
L_{irr}	Thickness of a irradiated layer, [m]
L_{ZrC}	Thickness of a virgin ZrC, [m]
k	Thermal conductivity, [W·m^{-1}·K^{-1}]
k_e	Electron thermal conductivity, [W·m^{-1}·K^{-1}]
k_{irr}	Thermal conductivity of irradiated layer, [W·m^{-1}·K^{-1}]
k_p	Phonon thermal conductivity, [W·m^{-1}·K^{-1}]
k_{Pt}	Thermal conductivity of platinum, [W·m^{-1}·K^{-1}]
k_S	Thermal conductivity of sample, [W·m^{-1}·K^{-1}]
k_{ZrC}	Thermal conductivity of virgin ZrC, [W·m^{-1}·K^{-1}]
M	Matrix representing product of quadrupole, resistance, and heat loss matrices
P_0	Heating power, [W]
P_c	Probe power in contact with the surface, [W]
P_a	Probe power far from contact surface (air), [W]
P_{irr}	Probe power on irradiated ZrC surface, [W]
P_{ZrC}	Probe power on virgin ZrC surface, [W]
Q	Quadrupole matrix
r	Radial directional coordinate, [m]
r_0	Heating radius at 1/e^{2} of maximum intensity, [m]
R	Thermal resistance of a layer, [m^{2}·K·W^{-1}]

R_{1or2}	Resistors in Wheatstone bridge, [Ω]
R_c	Potentiometer in Wheatstone bridge, [Ω]
R_i	Output impedance, [Ω]
R_{th}	Thermal resistance, [$m^2 \cdot K \cdot W^{-1}$]
$S_{Amp,p}$	Relative sensitivity of the amplitude of a complex function to parameter "*p*"
S_p	Relative sensitivity to parameter "*p*"
$S_{\psi,p}$	Relative sensitivity of the phase of a complex function to parameter "*p*"
t	Generic time, [s]
T	Generic temperature, [K]
T_a	Absolute temperature of a body, [K]
T_0	Temperature at heated surface of a sample, [K]
u	Hankel transform coordinate, [m^{-1}]
v_c	Energy carrier velocity, [$m \cdot s^{-1}$]
v_t	Thermal phase velocity, [$m \cdot s^{-1}$]
V_{A-B}	Differential voltage, [V]
V_{DC}	DC voltage, [V]
z	Axial directional coordinate, [m]
Z	Thermal impedance, [$m^2 \cdot K \cdot W^{-1}$]
Z_C	Capacitive thermal impedance component of a material, [$m^2 \cdot K \cdot W^{-1}$]
Z_{irr}	Thermal impedance of thermally-thick irradiated layer, [$m^2 \cdot K \cdot W^{-1}$]
Z_{irrZrC}	Thermal impedance of two-layer, irradiated ZrC with R_{th}, [$m^2 \cdot K \cdot W^{-1}$]

Z_{ml}	Thermal impedance of a multilayered material, [$m^2 \cdot K \cdot W^{-1}$]
Z_{ZrC}	Thermal impedance of thermally-thin ZrC sample, [$m^2 \cdot K \cdot W^{-1}$]
$\tilde{T}$	Hankel transformed temperature
$\tilde{Z}$	Hankel transformed thermal impedance
α	Thermal diffusivity, [$m^2 \cdot s^{-1}$]
δT	Incremental temperature rise above T_a, [K]
ΔP	Probe power difference between contact and suspended in air, [W]
ε	Total hemispherical emissivity
θ_D	Debye temperature, [K]
λ_c	Mean free path, [m]
λ_t	Thermal wavelength, [m]
μ	Thermal diffusion length, [m]
ρ	Density, [$kg \cdot m^{-3}$]
σ	Complex thermal wave number, [m^{-1}]
σ_e	Electrical conductivity, [$m^{-1} \cdot \Omega^{-1}$]
σ_m	Hankel space wave number, [m^{-1}]
σ_{SB}	Stephan-Boltzmann constant, [$W \cdot m^{-2} \cdot K^{-4}$]
τ	Relaxation time, [s]
φ	Heat flux, [$W \cdot m^{-2}$]
φ_0	Net heat flux at exposed surface of sample, [$W \cdot m^{-2}$]
φ_{in}	Heat flux at exposed surface of sample, [$W \cdot m^{-2}$]
ψ	Generic phase

ω	Angular frequency, [rad·s^{-1}]
$\widetilde{\varphi}_0$	Hankel transformed net heat flux at the heated surface
$\widetilde{\varphi}_{in}$	Hankel transformed heat flux at the heated surface

CHAPTER 1

INTRODUCTION

Thermal transport plays a critical role in energy generation and conversion processes. The development of new technologies in these fields relies on our understanding and ability to predict these transport processes. This work presents a detailed experimental study of thermal transport on ion-irradiated material using a combination of techniques providing multi-scaled measurement results. This chapter lays out the motivation for this work and overviews the materials and methods used to accomplish the objectives, found in Chapter 2.

1.1. Motivation

Many technological and scientific advances occurring in the world today rely on the synthesis, processing, and characterization of materials at nanoscales [1, 2]. In many applications, understanding the thermal performance of such materials is crucial. For example, the development of improved electronic devices is strongly correlated with Moore's law, showing an exponential growth for the number of transistors on integrated circuits with transistor count doubling every 18 months. Such increase in transistor density is marked by a reduction of size, $<$ 30 nm today, having gate thickness ~ 1.2 nm, notably resulting in increasing power densities ($\propto L^2$) that places greater burden on thermal management. Understanding material behavior at these small scales is pushing scientific understanding and creates great experimental challenges for data collection.

In many technologies, materials are pushed to their limits such as those found inside a nuclear reactor, which experience varying temperatures, pressures, and harsh irradiation conditions over long time scales where, again, experimental data is difficult to collect. The conditions experienced by these materials can result in modification of the material structure from the atomic/nano-level to macro-levels [3]. These changes affect, among other properties, the thermal transport capability, a critical property since the main objective of a power plant is to transfer heat from the fuel to produce electricity. Both scientific advancement and technological development increasingly call for bridging the gap between the nano- and macroscale worlds. The bridge will be built using data from improved multi-scaled experimental techniques as well as advancing theory and computational predictive capabilities.

The irradiation process provides a unique opportunity to change material structure at the molecular level in such a way that material structure can be correlated to material behavior [4]. Additionally, ion irradiation (defined here as any charged particle) has provided a feasible alternative to neutron irradiation for time- and cost-saving studies of irradiation effects in materials [5]. The achievable penetration depth for laboratory-scale accelerators and implanters is between 0.1-100 μm. In the case of neutron-irradiated samples, using samples of small size will reduce overall sample radioactivity, allowing for easier (and cheaper) handling of the material through characterization experiments. In either case, the small sizes and geometries of such samples create special metrological challenges for extracting desired data.

To date, significant progress has been made in the development of thermal measurements capable of high spatial resolution [2, 6-8]. Still much work is being directed toward improving and innovating new methodologies to meet the challenge of nanoscale measurement. Photothermal techniques and thermal microscopy represent some of the most promising technologies to achieve this goal [2].

1.2. Overview

In a manner not previously studied, four thermal wave methods will be used in this work to characterize the proton-irradiated layer in zirconium carbide (ZrC) including: scanning thermal microscopy (SThM), spatial-scanning front-detection photothermal radiometry (PTR), lock-in IR thermography (lock-in IRT), and tomographic, frequency-based PTR. Due to a combination of acceptable neutronic performance, thermal properties, chemical behavior, and physical properties, ZrC is being considered in tri-structural isotropic (TRISO) fuel as an oxygen getter in the kernel, as a coating layer for fission product retention, or a combination of these two functions as a direct coating on the fuel kernel [9]. However, the understanding of the irradiation defects, especially the degradation of the thermophysical properties of irradiated ZrC, is under-studied.

The intent is to explore the ability of each measurement system to thermally characterize ion-irradiated samples. In fact, the combination of systems is intended to provide a multi-scaled measurement approach to measure the irradiation damage profile in the sample with resolution down to ~ 1 μm as well as to provide quantitative, macroscopic thermal conductivity of the damaged/undamaged regions of the sample. SThM measurements have been performed by three different SThM systems located at Utah State University (USU) in Logan, UT, the Silesian University of Technology in Gliwice, Poland, and the Université de Reims Champagne-Ardenne (URCA) in Reims France. PTR and lock-in IRT were also performed at URCA.

CHAPTER 2

OBJECTIVES

The purpose of this work is to use thermal wave techniques for the thermophysical characterization of ion-irradiated materials. Scanning thermal microscopy, spatial-scanning front-detection photothermal radiometry (PTR), lock-in IR thermography (lock-in IRT), and tomographic, frequency-based PTR are used to measure thermal conductivity of proton-irradiated zirconium carbide.

The objectives of this work include:

- Development of a methodology to measure the thermal property change within a proton-irradiated layer of metal-ceramic materials using thermal wave techniques including: scanning thermal microscopy, spatial-scanning PTR, lock-in IRT, and tomographic, frequency-based PTR;
- Measurement of the thermal conductivity profile in the irradiated zone of proton-irradiated ZrC to establish an appropriate theoretical description for proton irradiated ZrC for tomographic PTR and quantify change of the irradiation-damaged zone of proton-irradiated ZrC.

CHAPTER 3

THEORETICAL BACKGROUND AND CONSIDERATIONS

The objectives of this study require a cross-disciplinary approach with knowledge of subjects of heat transfer in solids, particle-radiation effects in materials, and advanced thermometry techniques. This chapter presents a foundational background for these subjects illustrating relevant aspects of each. The final section of the chapter presents a brief summary of related works performed simultaneously with the work herein.

3.1. Thermal Conduction in Solids

Heat conduction is one of the primary modes of heat transfer and plays a crucial role in innumerable applications as it occurs in all mediums containing a temperature gradient. In this work, the application limits the focus to conduction in solids. As a means of understanding irradiation-damage effects on thermal transport, the purpose of this section is to only briefly introduce relevant topics regarding macroscopic views of thermal properties [10, 11], thermal resistance [12, 13], thermal energy carriers, and carrier scattering mechanisms [14, 15].

3.1.1. Material Properties

Four interrelated material properties are important for conduction in solids at continuum scales, of which only two are independent. These temperature-dependent properties include: thermal conductivity, k, volumetric heat capacitance, $C_\mathrm{p} = \rho c_\mathrm{p}$ (not discussed in detail here), thermal diffusivity, $\alpha = k/\rho c_\mathrm{p}$, and thermal effusivity, $e = \sqrt{k \rho c_p}$. However, despite their importance in engineering applications, accurate measurement and usage of thermal properties remains an engineering challenge that requires careful consideration. Perhaps, the most complete and referenced database of material thermophysical properties is those compiled in the 1970's by the Thermophysical Properties Research Center [16]. Specific sample geometries, sizes, types, non-destructive requirements, etc. present additional challenges that must be overcome in measurement, to which great investment has been devoted over the past century from industry and research ventures alike [17, 18].

Thermal conductivity, which is the measure of a material's ability to transport heat energy, is an intrinsic property of any material. The thermal conductivity of a material represents the constitutive constant relating the vector quantity of heat flux to the gradient of a temperature field, a relationship more commonly known as Fourier's Law. Therefore, steady-state measurement techniques directly measure thermal conductivity. More formally, it is defined as the quantity of heat energy transmitted per unit time per unit distance per unit temperature change over that distance in the direction of heat transfer.

The thermal diffusivity of a material is a lesser understood parameter representing the ratio of a material's ability to conduct heat versus store energy during changes of temperature. It is, therefore, associated with the speed of propagation of heat in a material. Materials of high thermal diffusivity will respond rapidly to changes in thermal environment, while the opposite is true as well. Although for most solid materials thermal diffusivity maintains a nearly linear relationship to thermal conductivity (indicating small variation of heat capacitance), it is significant to note that the thermal diffusivity of air is approximately equivalent to that of many metals such as Pt and Ni.

The thermal effusivity of a material is probably the least known of the important conduction properties. The thermal effusivity of a material is the primary parameter determining temperature relationships of heat transfer processes across boundaries between differing media (neglecting Kapitza/contact resistances). It is a measure of the heat stored in a solid per degree of temperature rise from the start of a surface heating process. For example, when two semi-infinite solids at different uniform temperatures, T_1 and T_2, are brought together, the temperature at the contact, T_c, assuming no thermal resistance is governed by the relationship: $T_c = (T_1e_1 + T_2e_2)/(e_1$

+ e_2). Here $\underline{e}_i$ represents the thermal effusivity of the materials. From this equation, the thermal effusivity can then be viewed as a weighting factor in determining which material most influences the resulting contact temperature. Therefore, thermal effusivity plays a critical role in heat transfer processes in multilayered materials. Both thermal diffusivity and thermal effusivity may be obtained using transient measurement techniques.

3.1.2. Thermal Resistance

Thermal resistances at interfaces also play a critical role in heat transfer processes at any interface. The formal definition of a thermal resistance, R_{th}, is the ratio of the temperature difference to the heat flux. At an interface, the thermal resistance results in a temperature discontinuity. A thermal contact resistance [12] is a thermal resistance that is the result of mechanical contact between two materials, which, due to variations of surface roughness, is most reliably determined by experimental measurement. Thermal boundary resistance [13, 19, 20], or Kapitza resistance [21] is distinguished from thermal contact resistance as it is found at the atomically adjoined interfaces. In such cases, the thermal resistance arises due to mismatched electronic and vibrational properties of the adjoined materials having the effect of scattering an energy carrier passing through it. In the scope of ion-irradiated materials, the existence of a thermal boundary resistance is a possibility in a location where material structure undergoes a significant transition as may be the case at the end of the ion-stopping zone.

3.1.3. Energy Carriers

For conduction in solid materials, energy is transported by two types of energy carriers: electrons (dominant mode in metals) and phonons (dominant mode in non-metals). A phonon is a particle view of quantized lattice vibrations (elastic waves that only exist at discrete energies). In a solid material, atoms are bound in a periodic arrangement called a lattice. It is the periodicity of the atoms that dictates the allowed energy states of thermal carriers in a solid. For a detailed description of crystallography and solid lattices see [22]. Heat transfer involves the motion of heat carriers generated by temperature differences and distributed randomly in all directions. In the case of metal-ceramics, carriers of both types contribute significantly to overall thermal conductivity, which is commonly represented as the sum of the electronic and the lattice vibration contributions,

$$k = k_e + k_p \,. \tag{3.1}$$

3.1.3.1. Kinetic Theory

A rudimentary, but surprisingly useful relationship for thermal conductivity may be derived using simple kinetic theory [14]. With this description energy carriers are viewed as particles traveling with some average random velocity, v_c. The particles travel for an average time, τ_c or relaxation time, before being scattered (energetic interactions with other particles, boundaries, or the material structure causing energy exchange and changes of direction). The average distance traveled between each interaction is called the mean free path, $\lambda_c = v_c\tau_c$. Then considering 1-D flow of energy across an imaginary plane, a relationship relating the gradient of energy in this direction to temperature through volumetric specific heat, ρc_p results in a Fourier's Law relationship giving the thermal conductivity as

$$k = \rho_c c_p v_c \lambda_c / 3 \,. \tag{3.2}$$

This simple relationship shows the direct dependence of thermal conductivity on the mean free path of the solid. Importantly, the mean free path of electronic and phononic energy carriers are different. In irradiation-damaged materials, the mean free path will be affected by types and densities of defect structures formed in the process [4].

3.1.3.2. Scattering Effects

The physics of scattering events in a solid is detailed in several sources [14, 22, 23]. The scattering mechanisms include events between energy carriers themselves and between the energy carriers and defects or imperfections in the crystalline structure of the material (boundary effects can also be important if geometry length scales ~ λ). Generalized scattering effects on mean free path as a function of temperature are presented in Fig. 3.1. At high temperatures, phonon scattering events play a dominant role in determining mean free path, as increasing temperature means increasing phonons ($k \propto 1/T$). For non-metals in particular, phonon-phonon interactions termed Umklapp processes are most responsible for reduced overall energy flux. At low temperatures, phonon-boundary scattering dominates and transport is proportional to specific heat and crystal size ($k \propto T^3$). The effects of material defects play a greater role with increasing temperature as well, however, they are generally dominated by phonon scattering events.

As mentioned above, the periodicity of the crystalline structure in a solid determines the available energy states responsible for energy transport. Naturally, defect structures, which are present in all but pure crystalline materials, play a critical role in modifying thermal transport processes. These defect structures are classified as: (0-D) point - interstitial, vacancies, or impurities, (1-D) linear - screw and edge dislocations, (2-D) planar - grain boundaries, external

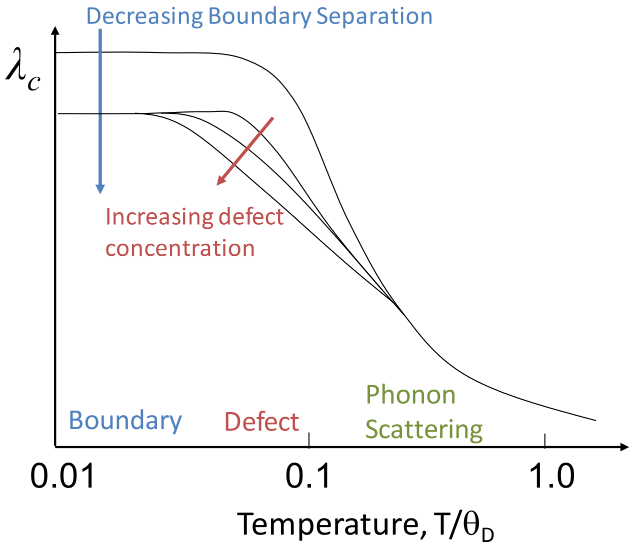

Fig. 3.1. Representative effects of boundaries, defects, and phonon scattering events on mean free path, λ_c. θ_D is the debye temperature.

surfaces, or (3-D) volume - pores, cracks. The effects of each of these on thermal transport is has been and remains an important area of ongoing research. The irradiation process provides a unique ability to generate defect structures, which can be characterized and correlated to thermal transport properties. In ceramic materials where phonon transport dominates the irradiation-induced defect scattering can exceed phonon-phonon scattering, so that the temperature dependence of thermal conductivity may be nearly removed [24]. A summary of phonon relaxation relationships for different defect types is found in [4].

3.1.3.3. Wiedemann-Franz Law

The Wiedemann-Franz Law provides a relationship between the free electrons responsible for electrical conductivity and for the electronic thermal carriers. It states that the ratio of thermal conductivity, *k*, to electrical conductivity, σ_e, is directly proportional to temperature or

$$LzT = k / \sigma_e . \tag{3.3}$$

where $Lz = 2.44 \cdot 10^{-8}\ \mathrm{W \cdot \Omega \cdot K^{-2}}$ at room temperature.

Frequently this relationship is used to estimate thermal conductivity from the easier-to-measure electrical conductivity in metals. In the case of materials with energy carriers of both types such as metal-ceramics, it is used to estimate the electronic contribution of thermal conductivity.

3.2. Particle-Radiation Effects

The subject of particle-radiation effects in materials is broad covering topics from displacement energies and cascade formations to the resulting changes to physical properties. These effects vary depending on the form of irradiation and the types of materials undergoing the irradiation process. The spans of length and time scales associated with radiation processes are also great, on the order of 10^{-10} m to 1 m and 10^{-13} s to 10^{8} s. This section will introduce the subject of ion studies of irradiation damage as well as some of the basic processes that occur at an atomic level as a means of providing a framework for understanding the effect on thermal transport. Extensive descriptions of radiation effects in various materials can be found in [3, 25-27].

3.2.1. Defect Formation

The primary microstructural effect of radiation on solids is the production of atomic displacements. As an irradiating particle passes through a material, its energy is transferred to the material through direct nuclear interactions transferring momentum to the surrounding lattice or by a process termed radiolysis, which is a response to electronic excitations by ionizing radiation. The transfer of energy to the lattice can result in the removal of an atom from its lattice site to form a vacancy. The freed atom may then end up in a stable, interstitial location. The resulting vacancy and interstitial results in the basic unit of radiation damage called the Frenkel pair. The displaced atom is called a primary knock-on atom (PKA) and can have sufficient energy to cause further atom displacements, resulting in a collision cascade event.

The minimum amount of energy required in a collision event to displace an atom from its lattice site is called the threshold displacement energy, E_d. If the energy transferred is less than this threshold, then the atom will not be displaced, but will vibrate interactively with neighboring atoms to dissipate this energy as heat (phonons). The threshold energy is dependent on the potential fields of the atoms in the lattice. Thus, within the lattice of a polyatomic material, different atoms have different threshold displacement energies.

During an irradiation process, the formation of Frenkel pair defects usually results in self-recombination or in recombination with other nearby Frenkel pairs to return to a lower energy state. At times, the defects undergo aggregation, which also lowers the elastic energy in the lattice. The product of the localization of defect structures between planes of lattice atoms is the formation of dislocation loops. For the case of the "insertion" (or removal) of a circular plane of atoms between existing planes in a lattice, the dislocation loop is called a prismatic or Frank loop [3]. In a cross-section perpendicular to the plane of the loop, a frank loop in a lattice appears as an edge dislocation. In ionic and particularly covalent bonding materials, the growth of these loops is limited due the localized, directional bonding that takes priority in terms of lowering energy. The short-range strain field created from the loops is energetically more favorable than open bonds. Irradiation temperature plays a critical role in the formation and growth process of point defects. At high temperatures the irradiation-induced defect structures will anneal out of the material

Other common radiation effects in materials are termed volume defect condensation effects, which include voids and precipitates. Voids result for the accumulation of vacancies in a 3-D space, which are stabilized by gases formed in the irradiation process. In some cases, precipitates may be formed from nonstoichiometric displacement of a sublattice in polyatomic materials.

As a result of these atomic processes, several macroscopic effects may be witnessed in irradiated materials. Significant and varied effects on mechanical, electrical, optical, thermal properties can result and have been the topics of many works. Swelling can result from the aggregation of vacancies (usually at higher temperatures where point defects have higher mobility). More common at lower temperatures, amorphization may result when a material loses long range order in the lattice.

As a means of quantifying radiation damage, the displacements per atom (dpa) is the dose unit used as a means to correlate damage irradiation produced under different conditions. It represents the ratio of atoms displaced by irradiation to the number of atoms present.

3.2.2. Ion-Irradiation Studies

Since the 1960s, ion-irradiation studies have been developed for the purpose of simulating neutron damage [5]. More recently, such studies have been used to study the irradiation assisted stress corrosion cracking in light water reactors, characterize effects in reactor pressure vessel steels, Zircaloy fuel cladding, materials for GenIV reactors and the advanced fuel cycle initiative [5].

Identification of basic mechanisms involved in a material's response in the initial stages of irradiation can be done efficiently using ion irradiation. The time and cost savings of these studies can be enormous. Ion irradiations can be carried out in a matter of hours compared to 1-2 years for neutron experiments. No special handling requirements are needed for ion-irradiated samples as little or no residual radioactivity is produced. The resulting savings is about 99% for cost and 90% for time. Still, the problem remains to show equivalency of results for ion and neutron studies [28].

Ions of different types have distinct differences in terms of the irradiation damage effects they produce. Fundamental differences between ion and neutron irradiation are: the particle energy spectrum of the particles and their associated depth of the penetration. Ion sources are have very narrow energy range; while neutron energy cover several orders of magnitude of energy. The electronic interactions experienced by ions through matter cause them to lose energy quickly and to interact with the material in a spatially varying manner. Neutrons can pass through long distances and produce spatially flat profiles.

The ion particles considered here include electrons (not a true ion), heavy ions, and protons. A detailed overview of the characteristics of each ion type can be found in [5]. Characteristics of electron irradiation include advantages of a simple source (TEM), high dosage rates allowing for short times. Disadvantages include a ~1 MeV energy limitation, no cascades or transmutation, a high temperature requirement that is not easy to control, and a non-uniform beam profile. Characteristic advantages of heavy ions include high dose rates (short times), high average temperature, and the production of cascades. Important disadvantages are a very limited penetration depth, strongly peaked damage profile (varies significantly with depth), high temperature requirement, no transmutation, and a potential for composition changes.

Over the past two decades, significant effort has been performed to refine proton irradiation as a radiation damage tool. Proton irradiation effects demonstrate characteristics that should be advantageous for studies of material properties such as thermal transport. The advantages include a relatively long penetration depth and flat damage profile over most of depth. This characteristic should lend well to a layered structure approximation of proton-irradiated materials. Other primary advantages are moderate dose rate (moderate times), moderate temperature requirements. The disadvantages of proton irradiations are minor sample activation, smaller and spread out cascades, and no transmutation.

3.2.3. Radiation Effects on Thermal Transport in Ceramics

The radiation defects in ceramics are considerably more complicated than in metals due to the presence of multi-sublattices, strong bonding orientation and the greater importance of chemical and ionization effects [26]. Due to a low density of valence band electrons, thermal conductivity of ceramic materials is mainly based on phonon transport. The effect of irradiation on ceramics at relatively low temperatures is to produce simple defects and defect clusters that very effectively scatter phonons, resulting in a significant degradation in thermal conductivity of material [4]. The electrical conductivity of ceramic materials shows little or no permanent alteration [26]. In metal-ceramic materials where phonons and electrons contribute to heat conduction, phonon thermal transport is expected to be most significantly affected by irradiation damage defects. Relatively few studies of radiation effects in metal-ceramics exist in literature with silicon carbide having the most investigations [24]. A more detailed review of literature regarding thermal transport studies in irradiated ZrC will follow in Section 4.1.1.

3.3. Thermal Wave Techniques

Thermal wave techniques encompass an important range of applications from physics, chemistry, biology, medicine, etc., for non-destructive characterization / evaluation of thin films, interfaces, surfaces [29]. As a thermal characterization tool, thermal waves have been used for over a century and half, since Angstrom measured the thermal diffusivity of a long copper bar [30]. However, most practical applications of photothermal methods appeared after Rosencwaig gave a comprehensive theoretical description of the photoacoustic effect in a solid using the physics of thermal waves [31]. The most familiar concept of a thermal wave is probably represented by periodic temperature oscillations within the surface of the earth. In general, thermal waves are simply temperature distributions oscillating in time and space.

3.3.1. Basics of Thermal Wave Techniques

In thermal wave techniques, periodic heating is applied to a sample inducing a periodic temperature response in the sample. The induced periodicity of the temperature field in the sample follows the mathematical description of evanescent waves, thus, the term thermal wave. Different thermal wave techniques are distinguished by the methods used for exciting and detecting these thermal waves. Although any time-dependent heating source could be used to generate thermal waves, two of the most common methods include using electromagnetic radiation or direct electrical heating [32]. Due to the great flexibility they allow in control and application, lasers or other light sources are common sources of excitation resulting in the classification “photothermal.”

The distance these thermal waves travel before the temperature amplitude decays to 1/e of the amplitude at the heated surface is called the thermal diffusion length,

$$\mu = \sqrt{\alpha / \pi f} \,. \tag{3.4}$$

where α is material thermal diffusivity and f is the heating modulation frequency. Thermal diffusion lengths for most materials are typically in the sub-mm range. Using the frequency-dependent thermal diffusion length, these techniques then have the advantage of non-destructively, depth-profiling the sample with knowledge of sample thermal and geometric parameters. However, the measured signal at a given frequency results from the integrated response of the material to the depth of the thermal diffusion length. For this reason, extracting specific, quantitative information from measured data is frequently an ill-posed problem requiring careful formulation of the thermal models used. Inversion algorithms will not be discussed in detail in this work but has been reported in literature and is an ongoing area of study [33-37] .

3.3.2. Thermal Wave Generation and Propagation

Consider a semi-infinite medium with constant properties experiencing periodic heating on its surface as shown schematically in Fig. 3.2. The temperature field in the solid may be found by solving the 1-D parabolic heat equation,

$$\frac{\partial^2 T}{\partial z^2} = \frac{1}{\alpha}\frac{\partial T}{\partial t} \,, \tag{3.5}$$

with a flux boundary condition having intensity, I_0, and angular frequency, ω, given as

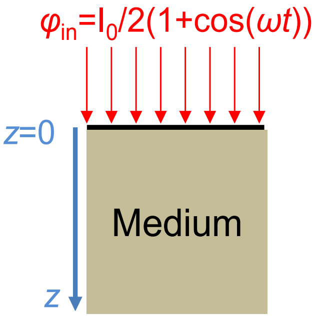

Fig. 3.2. Schematic of 1-D semi-infinite medium experiencing modulated heating.

$$-k\frac{\partial T(z=0,t)}{\partial z}=\mathrm{Re}\left(\frac{I_0}{2}e^{i\omega t}\right). \tag{3.6}$$

The consequence of heating is to produce a dc (constant) and ac (sinusoidal) components of the temperature field. The steady, periodic temperature field above ambient temperature may be assumed to have the form

$$T(z,t)=\mathrm{Re}\left(T(z)e^{i\omega t}\right). \tag{3.7}$$

Substituting this form into Eq. (3.5) and (3.6) gives, respectively,

$$\frac{\partial^2 T(z)}{\partial z^2}-i\frac{\omega}{\alpha}T(z)=0, \tag{3.8}$$

$$-k\frac{\partial T(z=0)}{\partial z}=\frac{I_0}{2}. \tag{3.9}$$

The solution to this equation for the boundary conditions of a periodic heat flux at z = 0 and the semi-infinite condition $T(z\rightarrow\infty)\rightarrow 0$ is

$$T(z,t)=\frac{I_0/2}{k\sigma}\exp(-\sigma z+i\varpi t)=\frac{I_0/2}{\sqrt{\omega e}}\exp(-i\pi/4)\exp(-\sigma z+i\varpi t). \tag{3.10}$$

The solution has the form of an attenuated plane wave and is therefore called a thermal wave. In analogy to acoustics, $\sigma = (i\omega/\alpha)^{1/2} = (1+i)/\mu$ may be considered the complex thermal wave number and $\lambda_t = 2\pi\mu$ is the thermal wavelength. The phase velocity, $v_t = \mu\omega = \sqrt{2\alpha\omega}$, increases with frequency. This simplistic solution illustrates several important features of thermal wave theory: 1) The thermal diffusion length, μ, represents the distance that the temperature propagates from the heated boundary until damped to 1/e = 37% of the value at the heated boundary; 2) the phase between the heat source and the temperature response as a function of distance is dependent only on μ and is $-\pi/4$ rad or -45° at the surface; 3) the temperature at the boundary surface is dependent on the thermal effusivity, e, of the medium; 4) the natural log of the magnitude of the complex temperature result is directly proportional to heating frequency, f, as shown by ($\ln|(T(z))| = -x/\mu + \text{constant} = -x\sqrt{\pi f/\alpha} + \text{constant}$).

Making an analogy to electrical impedance which relates electrical field to current density, the thermal impedance of medium is defined as the ratio of temperature, T, to heat flux, φ. Using thermal impedance to express photothermal signals in place of temperature is convenient as it is *independent of excitation power and of the specific photothermal method* used. The thermal impedance, Z, at the surface determined from Eq. (3.6) and (3.10) is

$$Z(\omega) = \frac{1}{\sqrt{\omega e}} \exp(-i\pi/4)\exp(-\sigma z). \tag{3.11}$$

3.3.3. Theoretical Models of Thermal Waves in Layered Systems

Thermal models used to describe the temperature field in multilayered materials have been derived using direct solutions to the heat diffusion equation, Green's function solutions [38], and the thermal quadrupoles method [39]. This work presents the formulation using thermal quadrupoles. First quadrupoles are introduced for a 1-D case. Next, a 2-D axisymmetric model will be introduced as an extension of the 1-D case.

3.3.3.1. Quadrupoles Method for 1-D Multilayered Materials

As an introduction to the thermal quadrupoles method [39], the temperature field in an opaque, isotropic, homogeneous plane wall (1-D) is derived from the heat equation with a periodic heat source at the surface (Fig. 3.3). The problem of a semi-transparent medium has been solved using quadrupoles in [40]. The heat source has a modulated intensity of $I_0(1+\cos(\omega t))/2$ where I_0 is the intensity of the source and $\omega = 2\pi f$ is the angular frequency of modulation. With this heat source the boundary condition may be written as

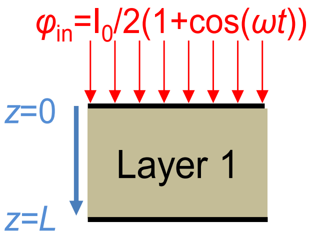

Fig. 3.3. Schematic of 1-D, finite, homogeneous material with modulated heating.

$$\varphi_{in}(z=0,t) = -k\frac{\partial T(z=0,t)}{\partial z} = \mathrm{Re}\left(\frac{I_0}{2}e^{i\omega t}\right). \tag{3.12}$$

As in the previous section, the solution for the temperature field will be comprised of the sum of the DC and AC components. The AC component may be written as

$$T(z,t) = \mathrm{Re}\left(T(z)e^{i\omega t}\right). \tag{3.13}$$

Substituting into the heat equation and solving results in a solution of the form

$$T(z) = A\sinh(\sigma^2 z) + B\cosh(\sigma^2 z), \tag{3.14}$$

where the 1-D complex thermal wave vector is $\sigma = (i\omega/\alpha)^{1/2} = (1+i)/\mu$ with thermal diffusion length, $\mu = (\alpha/\pi f)^{1/2}$ (3.4).

Substituting Eq. (3.14) into the definition of Fourier's law for heat flux and rearranging results in the following matrix relationship for temperature and heat flux between the front (z=0) and back ($z = L$) surfaces

$$\begin{bmatrix} T(z=0) \\ \varphi(z=0) \end{bmatrix} = \begin{bmatrix} A & B \\ C & D \end{bmatrix} \begin{bmatrix} T(z=L) \\ \varphi(z=L) \end{bmatrix}, \tag{3.15}$$

where $A = D = \cosh(\sigma L)$, $B = \sinh(\sigma L)/k\sigma$, and $C = k\sigma\sinh(\sigma L)$. The 'ABCD' matrix is called the quadrupole matrix of a plane wall, which will now be termed the $\boldsymbol{Q}$ matrix.

Now suppose as in the case of a multilayered material as shown in Fig. 3.4, several layers are connected in series. The relation of Eq. (3.15) may be applied successively to each layer of a composite of n layers resulting in an expression of the form

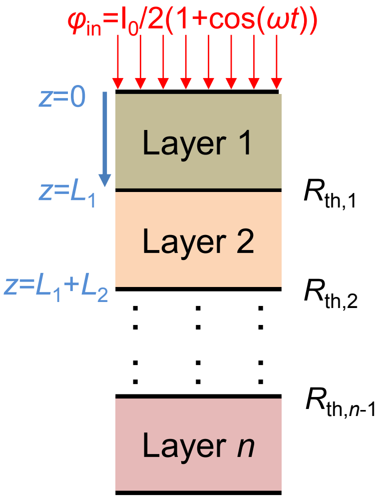

Fig. 3.4. Schematic of 1-D, multilayered material with modulated heating.

$$\begin{bmatrix} T_0 \\ \varphi_0 \end{bmatrix} = \prod_{j=1}^{n} [Q]_n \begin{bmatrix} T_n \\ \varphi_n \end{bmatrix}, \tag{3.16}$$

where subscripts *0* and *n* in the input and output matrices (containing T and φ) represent the front and rear surface temperatures and fluxes. Heat losses from the surfaces may be accounted for using the relationship, $\varphi_0 = -hT_0 + \varphi_{in}$ and $\varphi_n = hT_n$, where h is the heat transfer coefficient and T_0 and T_n represent the temperatures of the front and rear surfaces exposed to a gas. The gas temperature is assumed to be zero. Writing these relationships in matrix form and combining with Eq. (3.16) gives

$$\begin{bmatrix} T_0 \\ \varphi_{in} \end{bmatrix} = \begin{bmatrix} 1 & 0 \\ h & 1 \end{bmatrix} \prod_{j=1}^{n} [Q]_n \begin{bmatrix} 1 & 0 \\ h & 1 \end{bmatrix} \begin{bmatrix} T_n \\ 0 \end{bmatrix}. \tag{3.17}$$

The presence of a thermal resistance, $R_{th,j}$, at an interface may be accounted for using the relationship

$$\begin{bmatrix} T_j \\ \varphi_j \end{bmatrix} = \begin{bmatrix} 1 & R_{th,j} \\ 0 & 1 \end{bmatrix} \begin{bmatrix} T_{j+1} \\ \varphi_{j+1} \end{bmatrix}, \tag{3.18}$$

in the proper sequence of matrix multiplication. Defining matrix ***M*** as the matrix resulting from multiplication of the heat loss, quadrupole, and resistance matrices, the overall relationship can be written as

$$\begin{bmatrix} T_0 \\ \varphi_{in} \end{bmatrix} = \begin{bmatrix} M_{11} & M_{12} \\ M_{21} & M_{22} \end{bmatrix} \begin{bmatrix} T_n \\ 0 \end{bmatrix}. \tag{3.19}$$

The thermal impedance of the multilayered composite may then be defined as

$$Z_{ml} = \frac{T_0}{\varphi_{in}} = \frac{M_{11}}{M_{21}}, \tag{3.20}$$

where φ_{in} is the heating flux at $I_0/2$.

3.3.3.2. Extension for 2-D, Axisymmetric, Multilayered Materials

For each layer in a multilayered material as shown in Fig. 3.5, heated with a Gaussian intensity profile, the 2-D axisymmetric heat equation (assuming no volumetric absorption) takes the form

$$\frac{\partial^2 T}{\partial r^2} + \frac{1}{r}\frac{\partial T}{\partial r} + \frac{\partial^2 T}{\partial z^2} = \frac{1}{\alpha}\frac{\partial T}{\partial r}, \tag{3.21}$$

where z is in the through-thickness direction and r is the radial coordinate extending from the axis of the heating. The total power of the laser, P_0, is modulated as $P_0(1+\cos(\omega t))/2$. In this case, the modulated heat is assumed to be absorbed at the surface only, defined by the flux boundary condition for the AC component as

$$\varphi_{in}(r, z=0, t) = -k\frac{\partial T(r, z=0, t)}{\partial z} = \mathrm{Re}\left[\frac{P_0}{\pi r_0^2} e^{-2r^2/r_0^2 + i\omega t}\right], \tag{3.22}$$

where P_0 is the total heating power and r_0 is the heating radius at $1/e^2$ of the maximum intensity.

As with previous cases discussed, the temperature solution to Eq. (3.21) will be composed of DC and AC components. Substituting the assumed form of the AC component into

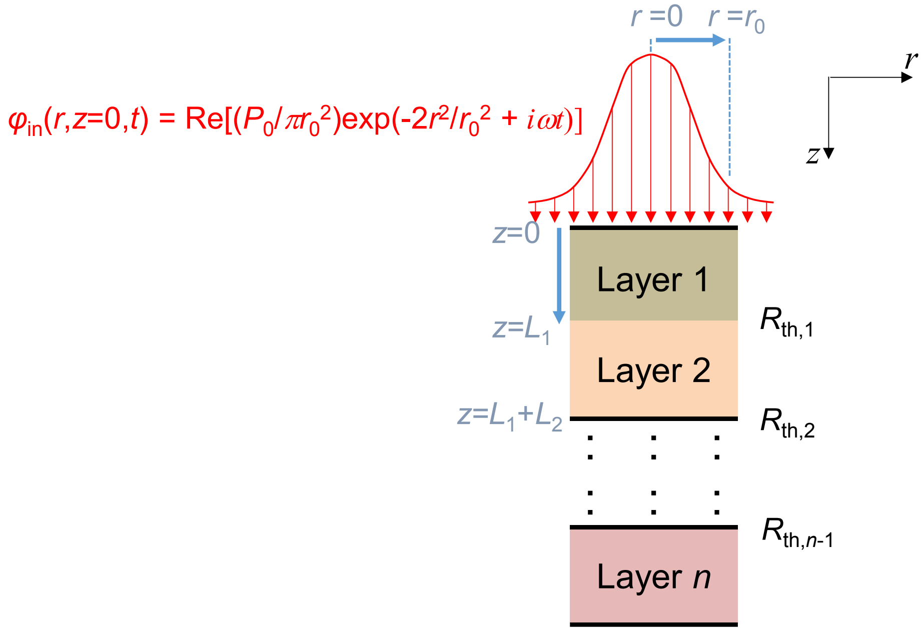

Fig. 3.5. Schematic of 2-D, multilayered material with modulated, Gaussian heating.

Eq. (3.21) and applying the Hankel transform to the heat equation and the periodic component of the heating boundary condition, respectively, gives

$$\frac{\partial^2 \tilde{T}(u,z)}{\partial z^2} - \sigma_m^2 \tilde{T}(u,z) = 0, \tag{3.23}$$

where $\sigma_m = (u^2 + i\omega/\alpha)^{1/2}$ and

$$\tilde{\varphi}_{in} = -k\frac{\partial \tilde{T}(u,z=0)}{\partial z} = \frac{P_0}{4\pi} e^{-u^2 r_0^2/8}, \tag{3.24}$$

where $\tilde{T}$ and $\tilde{\varphi}$ are the zero-order Hankel transform of temperature and flux. The zeroth order Hankel transform of $T(r,z)$ is defined by

$$H[T(r,z)] \equiv \tilde{T}(u,z) \equiv \int_0^\infty rJ_0(ru)T(r,z)dr, \tag{3.25}$$

where J_0 is the zero-order Bessel function. The inverse Hankel transform is defined as

$$H^{-1}[\tilde{T}(u,z)] \equiv T(r,z) \equiv \int_0^\infty uJ_0(ru)\tilde{T}(u,z)du. \tag{3.26}$$

Solving Eq. (3.23) for the temperature in Hankel space is completely analogous to the preceding discussion for the 1-D quadrupoles case with the primary difference lying in the definitions of the complex wave vector: 1-D case → $\sigma = (i\omega/\alpha)^{1/2} = (1+i)/\mu$, 2-D case → $\sigma_{\mathrm{m}} = (u^2 + i\omega/\alpha)^{1/2}$; and the heating amplitude: 1-D case → $I_0/2$, 2-D case → $P_0 e^{-u^2 r_0^2/8}/4\pi$.

Therefore, using the previous quadrupoles derivation for the 1-D case and using the inverse Hankel transform, the solution for the sample temperature at any radial location may be written as

$$T_0(r, z=0) = \frac{P_0}{4\pi}\int_0^\infty uJ_0(ru)\widetilde{Z}(u)e^{-u^2 r_0^2/8}du, \tag{3.27}$$

where $\widetilde{Z}(u) = \widetilde{T}_0/\widetilde{\varphi}_{in} = M_{11}/M_{21}$ is the thermal impedance at $z = 0$ of the multilayered material in Hankel space.

3.3.3.3. 1-D vs 2-D Considerations

The foregoing analysis presents 1-D and 2-D solutions for the thermal impedance at the surfaces of a sample undergoing periodic excitation. Mathematically, multidimensional heat flow has been shown to be equivalent to the 1-D case under the condition of capturing the entire temperature response of the heated surface at $z = 0$ [41]. This result has useful implications for many thermal wave techniques, simplifying the analysis for cases where this condition is met as is intrinsic to photoacoustic and photopyroelectric techniques. For photothermal radiometry, this condition may be met by ensuring the detection area has a radius ~ greater than the thermal diffusion length + the heating radius.

3.3.4. Thermal Wave Detection Techniques

Modulated thermal wave techniques most commonly employ a laser as an excitation source for heating a sample. The process of heating a solid by photothermal means is through the absorption of photons resulting in heating and temperature changes in the material. The advantage of using a light source for heating is non-contact excitation. In this work, thermal wave techniques of interest are classified as either photothermal or scanning probe microscopy (SPM). Scanning thermal microscopy techniques use a probe having a contact diameter approximately < 1 μm. The probe may act passively to detect temperature or actively to locally heat a sample. The temperature changes can lead to modification of thermophysical properties. Over the course of nearly four decades, a variety of thermal wave techniques have been developed with fundamental differences in the types of excitation sources, but more predominately, with differences in the detection of the thermal waves.

The temperature changes induced by modulated heating in the sample generate distinct physical phenomena (summarized in Fig. 3.6) including: acoustic waves, changes in thermal expansion (thermoelastic effect), changes of infrared emission, pyroelectric effect, changes of refractive index in gases or transparent media, changes of optical reflectivity, etc. The following presents a brief overview of common thermal wave techniques including photothermal and SPM types. For more detailed reviews of thermal wave techniques see [29, 42-44].

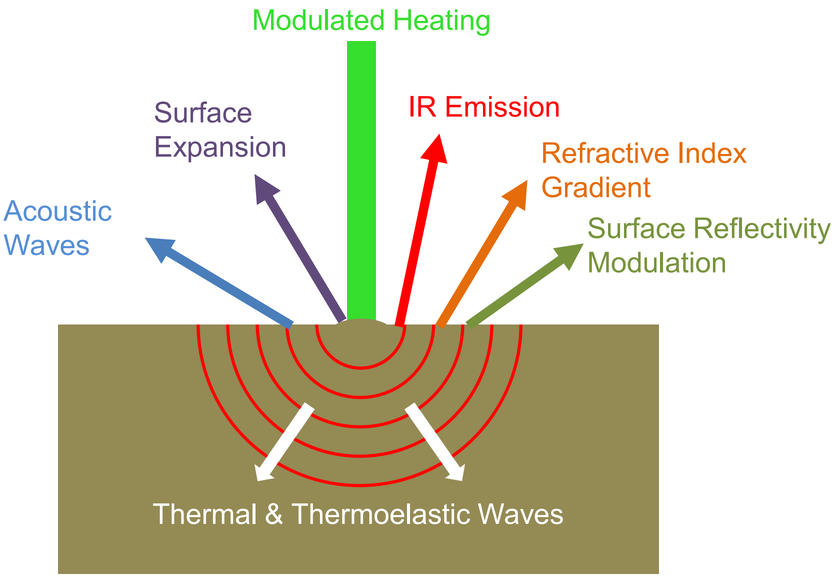

Fig. 3.6. Schematic of sample with modulated heating showing resulting thermal wave phenomena used for detection.

3.3.4.1. Photothermal Techniques

Photoacoustic Spectroscopy (PA) – Stemming from the discovery of the photoacoustic affect by Alexander Graham Bell in 1880 [45], the photoacoustic sensing technique utilizes a microphone to detect the pressure fluctuations induced in the gas at the solid/gas interface experiencing optical heating. Performing the measurement in a sealed enclosure allows the acoustic waves generated at the surface of a sample (acoustic piston) to pass through the gas to the microphone where they are converted to an electrical signal. The signal level is proportional to the temperature rise in the sample. Almost one hundred years after the discovery of the effect, pioneering work into quantitative theoretical and experimental work emerged [31, 46, 47] and expanded rapidly giving birth to a revival of photothermal techniques. The PA technique can measure thermal phenomena in solids, liquids, and gases. In materials of large surface area to volume ratios such as gases and powdered solids, temperature fluctuations $\sim 10^{-6}$ °C are detectable. The need for an enclosed measurement cell is a disadvantage of this technique.

Photothermal Displacement (PTD) – The photothermal displacement detection mechanism relies on the detection of the local thermal expansion at the location of heating [48]. Detection schemes are by use of a secondary laser probe beam that is reflected from the surface location experiencing thermal expansion. An interferometer or a bi/quad-cell photodiode detect changes of the surface conformation from the probe beam.

Photothermal Radiometry (PTR) – The thermal radiation emitted from matter having a temperature associated with is the basis for photothermal radiometry (PTR) [49, 50]. For temperatures near room temperature, the emitted radiation has dominant wavelengths in the near and mid-infrared spectral range as calculated from Planck’s Law. Local detection of the infrared emission is generally by means of using mirrors or optics to pass the IR emission from a sample to a liquid nitrogen cooled semiconductor detector. Frequency response can be from mHz to MHz providing good sensitivity to coatings and layered materials. Due to its non-contact, relatively less complex, and versatile setup, PTR has been used extensively over the previous several decades on a wide variety of applications. As this technique is of particular interest for this work, a more detailed description follows in Section 4.2.1.

Photopyroelectric Technique (PPE) – The photopyroelectric technique utilizes a pyroelectic transducer, which generates an electric charge proportional to the volume-averaged, incremental temperature within it [51-53]. The sensor (commonly polyvinylidene diflouride PVDF or $LiTaO_3$ single crystals) is placed in direct contact on the front or back of a sample. The PPE technique has been used widely to characterize solids, liquids, and gases. Advantages of the technique include: high sensitivity, high signal to noise ratio, large bandwidth of mHz to kHz, and simple setup.

Photothermal Beam Deflection (PBD) – Based on the mirage effect, photothermal or optical beam deflection detects the temperature-dependent, incremental changes of the index of refraction in a gas/liquid medium next to a heated surface [54, 55]. A secondary probe laser beam is passed parallel to the sample surface through the affected gas, into a position sensitive photodetector. The probe beam can be passed directly through transparent samples to detect changes of refractive index. The technique is limited to applications on smooth planar surfaces.

Modulated Optical Reflectance (MOR) – The optical reflectivity of materials can have temperature dependency providing the basis for the modulated optical reflectance method. A typical MOR detection scheme consists of a pump (heating) laser beam focused on a sample surface. A secondary probe laser beam is reflected from the sample surface and measured to capture the temperature-dependent intensity of the reflected beam [56, 57]. The advantages of this technique are that it is non-contact and can have excellent spatial resolution. Disadvantages are that it requires a reflective surface and very accurate alignment.

3.3.4.2. Scanning Probe Microscopy

Scanning probe microscopy (SPM) techniques come in a wide variety in an attempt to access information at sub-diffraction limited length scales. In spite of difficulties associated with quantitative measurements, SPM methods are among the most promising for obtaining nanometer-level thermal measurement resolution. These techniques employ a fine probe that is brought into (close) contact with a sample's surface to measure various characteristics. A more detailed introduction to scanning probe microscopy and scanning thermal microscopy will follow in Section 4.2.3. A brief introduction is provided here to two variations of two primary thermal detection techniques using SPM.

Scanning Thermal Microscopy (SThM) – Scanning thermal microscopy makes use of specialized thermal probes, which may be thermoresistive or thermocouple temperature sensors/heaters [58-60]. The resolution of the measurement is governed by the size of the tip, sample surface features, and heat transfer between a tip and sample. Heating in the probe is by an applied DC or AC current. Even for AC heating, SThM, in standard single probe configuration, is not a true tomographic thermal wave method as has been shown in [61]. From the perspective of the solution of a point heat source in a semi-infinite medium, it is shown that the temperature field in the sample decays much quicker than described by the frequency-dependent thermal diffusion length, μ, for $\mu < \sim 1$ MHz. Typically the physical geometry of the thermal probe limits the applied frequency to < few kHz. The conclusion is that DC and AC methods provide equivalent thermal information from a sample.

Scanning Thermoelastic Microscopy (SThEM) – In the case of scanning thermoelastic microscopy [62] or scanning Joule expansion microscopy [63, 64] for Joule heated samples, the thermal expansion of a heated sample is detected by the probe. Heating is provided by either the detecting probe (thermoelastic) or by modulated electric current applied to an electrically conductive sample (Joule expansion). Advantages of this technique compared to conventional

SThM is that the drawbacks of ill-defined contact resistances between the probe tip and the sample surface may be avoided [65]. Measurements of nanometer resolutions have been achieved with this technique [66-68] .

3.4. Additional Studies on Thermal Property Measurement during PhD Period

Many thermal property measurement techniques exist in the literature. In particular, thermal conductivity measurement is of great interest for many applications. Typically these techniques are classified as either steady-state or transient. As the classifications imply, steady-state measurements rely on measuring a steady temperature gradient through a material and using Fourier's law relationships to extract thermal conductivity. Transient measurements utilize a dynamic temperature field, from which thermal diffusivity and thermal effusivity are calculated providing a pathway to obtaining thermal conductivity. Although simple in principle, steady-state measurements typically require complicated experimental details to ensure known heat flow. Still, with proper consideration, steady-state measurement can yield very accurate results for thermal conductivity as they provide the most direct path to it. Transient measurement techniques can be relatively simpler and less sensitive to environmental effects. Measurement times can be short and sample size and temperature gradients are generally smaller. Due to these characteristics, transient techniques such as the hot-wire method and laser flash have attained the most widespread usage.

In conjunction with the primary objectives related to measuring ion-irradiated materials, several other related topics have been explored covering a broad range of measurement techniques. A comparative-guarded-axial heat flow (cut-bar) system was designed to measure bulk (composite) materials up to 1000 °C [69]. During this process, several advancements in the measurement technique were discovered and explored to improve the accuracy of the system [70-73]. These findings disprove several foregone conclusions regarding comparative measurement techniques providing a method to deal with the mismatch of thermal conductivities in meter (comparator) bars and the measured sample. In this way, measurement uncertainty for the system is estimated to be <6% from room temperature up to 1000 °C. Measurement results on certified reference materials verify this uncertainty with deviations of no more than 3% over the measurable temperature range of the samples (< 600 °C).

As a parallel to SThM measurements, the analysis of which is really a form of hot-wire anemometry, two approaches to measurement of thermal properties of thin fibers have been studied including a pure transient type and a 3ω type. Contributions to this work include improving the technique through proper modeling of heat loss mechanisms, experimental evaluations of theoretical models, and comparisons of techniques. These techniques allow for the extraction of thermal conductivity, thermal diffusivity, and heat capacity of fine diameter samples (both electrically conductive and non-conductive).

Contributions have been made in several other related works including: a parametric study of the modulated optical reflectance (MOR) technique [74] (Section 3.3.4.1); SThM analysis of wood cell walls using phase transition measurements [75]; and the development of a an approach to measuring/modeling surface roughness using PTR measurements [76].

Each of these projects has contributed to a more complete understanding and experience with thermal property measurement techniques ranging from classical techniques to state-of-the-art advanced techniques. It is with this foundation of knowledge that the approach to measurement of the ion-irradiated material was devised and carried out.

CHAPTER 4

MATERIALS AND METHODS

Because of the importance of thermal conductivity (*k*) in characterizing material performance in nearly any engineering and/or science application, a great deal of resources have been expended in efforts to measure/collect thermal conductivity data for innumerable materials. Much of the data presently available and used as reference data dates to the 1950-1970's. In spite of these efforts, uncertainties for thermal conductivity data remain large (typically > 5%) due to the differences inherent to material composition, formation, history, etc. It is for this reason that measurement of thermal properties remains an active field of study with vast amounts of measurement methods and variations of those methods having been developed over the last century. In this chapter, the material of study in this work, zirconium carbide, is summarized in the context of the objectives of this work. Following a description of the material, the multi-scaled techniques applied to its measurement are described in detail.

4.1. Zirconium Carbide

Transition-metal carbides have theoretical and practical interest due to their high melting point, hardness, metallic property, and superconductivity. Applications include cutting and grinding tools, thermal-barrier coatings, diffusion-resistant thin films, interconnects, and superconductivity devices.

Zirconium carbide (ZrC) is a typical transition metal-carbide that takes the NaCl ground-state crystal structure. Prior to irradiation, ZrC has several exceptional characteristics including hardness, corrosion resistance to fission products, high melting point of ~3540 °C (46.5% carbon atoms), and imperviousness to hydrogen attack. Due to a combination of acceptable neutronic performance, thermal properties, chemical behavior, and physical properties, ZrC is being considered in the tri-structural isotropic (TRISO) fuel as an oxygen getter in the kernel, as a coating layer for fission product retention, or a combination of these two functions as a direct coating on the fuel kernel [9]. However, the understanding of the irradiation defects, especially the degradation of the thermophysical properties of irradiated ZrC, is under-studied. ZrC has been studied using fast neutron, proton, and heavy ion irradiation, mainly focusing on the phenomenological change of the microstructures, while very little information was provided on the degradation of thermophysical properties [77]. Previous results from proton irradiated ZrC show that the irradiated microstructure consists of a high density of dislocation loops, and a significant change in the thermophysical properties is expected [78]. For a detailed summary of the properties of ZrC and previous irradiation studies see [77, 79].

As with other transition metal carbides, ZrC intrinsically has a high vacancy concentration in the carbon sublattice, and the properties of ZrC are often sensitive to the stoichiometry (C/Zr ratio). The significant effects of stoichiometry on physical properties means it is critically important that properties be discussed in the context of stoichiometry. For example, for stoichiometries yielding vacancies (C/Zr < 1), the thermal conductivity of hot-pressed ZrC decreases rapidly from ~45-10 $W \cdot m^{-1} \cdot K^{-1}$ with decreasing C/Zr from 1.0 to 0.9, respectively, becoming relatively constant at 8-10 $W \cdot m^{-1} \cdot K^{-1}$ over the range of $0.6 < C/Zr < 0.9$ [80].

As discussed in more detail in Section 3.1.3, the thermal conductivity of metal ceramics may be considered as the sum of the electron thermal conductivity and the phonon thermal conductivity. ZrC demonstrates unusual trend of increasing k with increasing temperature. The unusual trend is attributed to a reduced temperature dependency of the phonon thermal conductivity at higher temperatures and an increasingly dominating electronic contribution at higher temperature. At low temperatures, k is produced mostly by phonons, which are greatly scattered by conduction electrons. At higher temperatures, phonons and electrons both contribute but are scattered by either carbon vacancies (responsible for the large decrease of k seen for decreasing C/Zr ratio) or are affected by excess carbon, both acting to reduce k. At temperatures (> 500 K), the electronic contribution to k predominates [80, 81].

4.1.1. Previous Studies of Irradiation Effects on Thermal Conductivity of ZrC

Few studies have reported measurements of irradiation effects on thermal conductivity of ZrC using fast neutrons and heavy ions [79, 82, 83]. Taubin observed no notable changes in thermal properties in fast neutron irradiated $ZrC_{0.96}$ with a fluence of $\sim 4\cdot 10^{16}$ $n\cdot m^{-2}$. Snead et al. found only minor degradation in α of $ZrC_{0.87}$ irradiated with a fast neutron fluence of $1.8\text{-}9.0\cdot 10^{21}$ $n\cdot cm^{-2}$ with maximum degradation of ~15% at irradiation temperatures ~<1473 K. Higher temperature irradiations showed only slight degradation of α. The non-irradiated thermal conductivity for their sample was between 12-16 $W\cdot m^{-1}\cdot K^{-1}$. They attributed the reduction mainly to phonon scattering as the electronic contribution (electrical resistivity) to thermal conductivity showed no change [79]. David et al. found a 50% and 75% decrease in thermal conductivity for 10^{16} and $6\cdot 10^{16}$ $ions\cdot cm^{-2}$, respectively, on ZrC (virgin k = 20 $W\cdot m^{-1}\cdot K^{-1}$, composition not specified) irradiated by 25.8 MeV krypton ions [83].

4.1.2. ZrC Sample Preparation

The ZrC sample studied in this work is a 3 mm disc of nearly stoichiometric (C/Zr = 1.01), hot-pressed, commercial-grade zirconium carbide (ZrC) cut from a rod having a measured density of 6.58 $g\cdot cm^{-3}$, near the theoretical density of 6.60 $g\cdot cm^{-3}$. The value of specific heat, c_p, has been taken from the literature as 368 $J\cdot kg^{-1}\cdot K^{-1}$ [80, 84, 85]. One face of the 500 μm thick disc was polished and irradiated using a 2.6 MeV proton beam. Both pre- and post-irradiation the sample grain size was studied using scanning electron microscopy (SEM) finding an average size of 24 μm and no indication of grain boundaries, respectively. A more complete description of the irradiation preparations and conditions of the sample is given by Yang et al. [78].

Proton irradiation was performed at 600°C until the damage level reached an approximate level of 1.75 dpa (displacements per atom) in the nearly constant portion of the profile comprising the first several tens of microns of the damage depth profile. The damage profile calculated by TRIM2008 [86] (Transport of Ions in Matter) using threshold displacement energies of 35 eV for zirconium and 25 eV for carbon as given by Yang et al. [78] is shown in Fig. 4.1a. The numerical result is compared to the profiles obtained using thermal transport measurement techniques in Chapter 6. The damage profile will have some proportionality to the degradation of thermal conductivity of the material.

After irradiation, a fragment of the sample was fractured off to reveal the cross section of the damage profile to measure using the spatial scanning techniques. The cross section was mounted in epoxy and polished down to 0.02 μm colloidal silica. The remaining disc was used for the frequency-based PTR measurements. Sample measurement configurations are shown in Fig. 4.1b. Additionally, a disc of undamaged ZrC was used to measure the thermal properties of the virgin ZrC material.

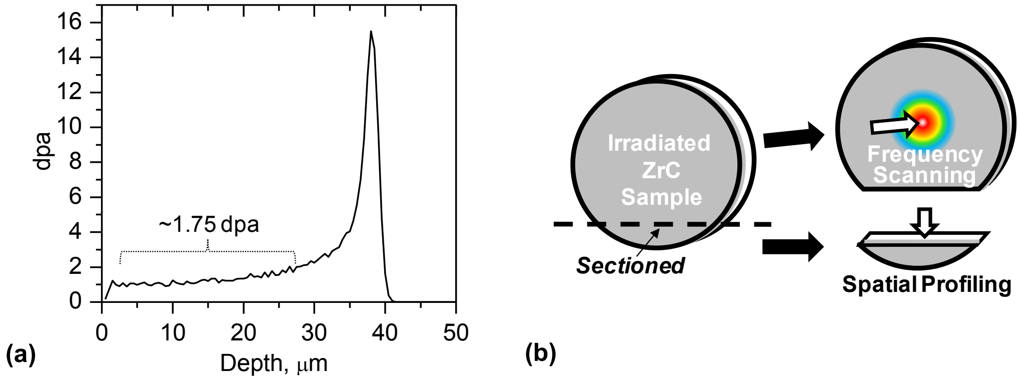

Fig. 4.1. (a) Numerically calculated damage profile for 2.6 MeV protons in ZrC from TRIM2008 [86] (b) Sample measurement configurations for frequency and spatial profiling techniques

4.2. Multiscale Thermal Wave Detection Techniques and Instrumentation

For ion-irradiated materials, the shape, depth, and magnitude of the thermal degradation profile through the irradiated zone of the material is unknown and poses a challenge for traditional measurement techniques. In recent years, frequency-based thermal wave methods have been used to investigate thermophysical properties of ion-irradiated samples [83, 87, 88]. Although, the thermal properties extracted from the thermal diffusion models in such measurements have typically been based on layered descriptions of the ion-damaged surface with layer thicknesses estimated from numerical calculations of the irradiation damage. One study used Transmission Electron Microscopy (TEM) of the in-depth irradiation damage profile to validate the numerically predicted profile [87]. The SThM measurements performed on ion-irradiated samples were done on the irradiated surface measuring from the damaged region to a zone masked from the irradiation. Only for titanium carbide (TiC) was the change of thermal property detectable. For zirconium carbide (ZrC), a degradation of thermal signal was measured but found to be at least partially attributed to oxidation on the irradiated surface [89].

In this work, photothermal radiometry, lock-in IR thermography, scanning thermal microscopy are investigated for the thermophysical characterization of the proton-irradiated ZrC. In particular, complementary approaches are to be explored. The first two measurement techniques discussed fall under the classification of IR detection while the third represents a type of scanning probe microscopy. The following section summarizes the relevant literature pertaining to these methodologies and presents the experimental setups used in this work.

4.2.1. Photothermal Radiometry

Photothermal radiometry (PTR) is one of the most common techniques used for the detection of thermal waves due to its simplicity, robustness, non-contact configuration, and compatibility with many industrial requirements. PTR is distinguished from IR thermography (following section) in that a single monolithic IR sensor is used rather than an IR sensing array. A typical PTR setup utilizes a light source such as a laser to heat a sample. Detection of the temperature response of the sample is accomplished by means of collecting the IR emission and passing it into an IR detector. Further distinction may be made as to whether the sample heating is modulated or pulsed [90]. In this work, modulated (frequency-domain) PTR is used in all cases.

Modulated PTR was first introduced by Nordal and Kanstad [49, 50]. In analogy to theory developed for the photoacoustic method, full modulated PTR theory was developed in [91, 92]. Since then, applications include thermal and optical properties of homogeneous, layered materials, thin films, etc. of both inorganic and organic [93] materials. Two recent studies were performed using frequency-domain PTR on ion-irradiated materials [87, 88]. More recent summaries of the technique can be found in [40, 94].

In modulated PTR, the light source is intensity modulated onto the surface of a sample. An IR detector measures the resulting temperature response of the sample and is connected to a lock-in amplifier, which captures the oscillating component of the response for a given heating modulation frequency. As is shown from the theoretical discussions in Sections 3.3.3 and 4.2.1.2, the measured signal from the lock-in, the thermal wave response, is dependent on the thermal parameters of the sample. This configuration allows for flexibility in configurations, making PTR a versatile tool for a variety of thermophysical characterization approaches. Heating may be focused or defocused and can be applied to the front or back of the sample, allowing differing sensitivities to the thermophysical structure of a sample [95].

4.2.1.1. Description of Measurement System

The PTR system used in this work is located at URCA in Reims, France. A schematic and photography of this PTR system in front detection configuration (FD-PTR), used for both spatial and frequency scanning, is presented in Fig. 4.2. The system uses a DPSS, 532nm laser

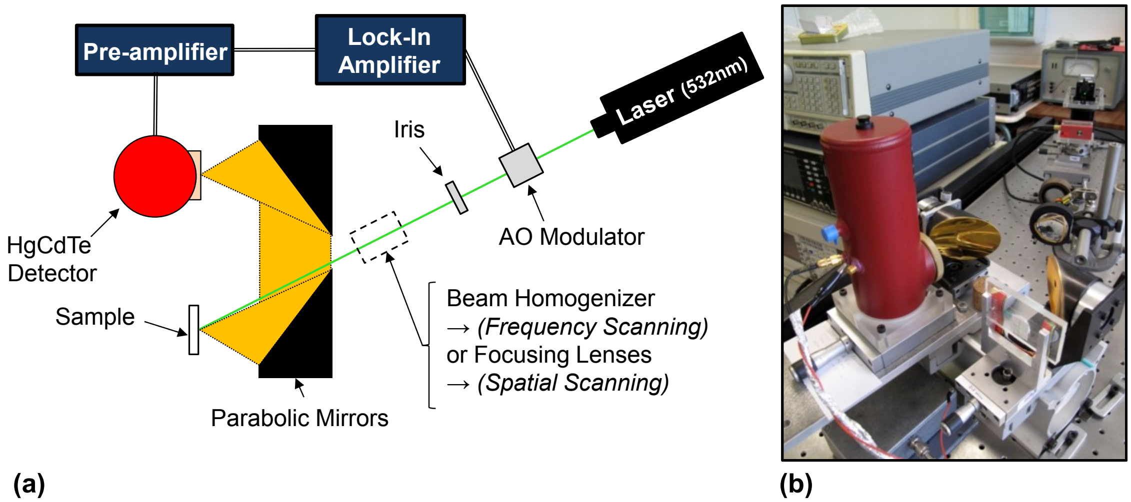

Fig. 4.2. Photothermal radiometry setup at URCA used for measurement: a) schematic view; b) photograph

modulated by an acousto-optical modulator (AOM) at a given frequency to heat the sample surface. Parabolic mirrors capture the emitted IR radiation from the sample, focusing it into an HgCdTe detector with a 1mm^2 detection area. A preamplifier passes the signal from the detector to a lock-in amplifier which measures the temperature amplitude and phase relative to the heat source.

For the frequency-scanning measurements, the Gaussian heating laser beam profile is homogenized using a flat-top beam shaper. In this way, the entire surface of the sample ($<$ 3mm diameter) is heated uniformly creating an approximate 1-D heating condition. Amplitude and phase spectra are then measured for the range of frequencies having the greatest sensitivity to the parameters of interest and used to fit to the thermal model to extract the desired parameters.

For the spatial-scanning measurements, the flat-top beam shaper was replaced with a set of lenses to focus the heating spot to a size of $\approx$50 μm. The sample was then scanned laterally using a micrometer stage at a defined frequency.

4.2.1.2. Photothermal IR Radiometric Signal

When a black body is subjected to modulated radiation, its surface temperature will change periodically as was first observed in [96]. The resulting temperature depends on the thermo-optical properties of the sample near the surface. The resulting temperature change in the sample creates periodic emission from the sample obeying the Stefan-Boltzmann Law defining the total radiant emission from a black body as $E_b = \sigma_{SB} T_a^4$, where $\sigma_{SB} = 5.67 \cdot 10^{-8}$ W·m^{-2}·K^{-1} and T_a is the absolute temperature of the body. This emission is also dependent on the thermo-optical properties of the sample. Assuming emission is from the sample surface only (body is opaque at emission wavelengths), the signal measured by the IR detector results from the IR emission of the sample surface, which for a gray and diffuse body, q_{gd}, is defined as

$$q_{gd} = \varepsilon \sigma_{SB} T_a^4 , \tag{4.1}$$

where ε is the total hemispherical emissivity of the emitting body. For the case of small surface temperature fluctuations, $\delta T << T_a$, the resulting increment in thermal radiation emittance may be found using a Taylor series expansion of Eq. (4.1) giving

$$\delta q_{gd} = 4 \varepsilon \sigma_{SB} T_a^3 \delta T \; . \tag{4.2}$$

The incremental temperature, δT, represents the thermal wave response of the heated body for a given frequency and time. For cases of materials other than those that are opaque see [92]. Written in general form, δT at the surface resulting from modulated heating may be expressed as

$$\delta T(z = 0, \omega, t) = Amp(\omega) \exp\left(i(\left[\omega t + \psi(\omega)\right]\right), \tag{4.3}$$

where $Amp(\omega)$ and $\psi(\omega)$ are the amplitude and phase relative to heating of the thermal wave at the surface of the sample.

However, the overall response measured by the IR detector is influenced by instrumental factors from the detector, modulator, and other electronic components as well as the solid angle from the sample to the capturing optics, resulting in a prefactor, K_{PTR}, incorporating these effects. Thus, the voltage signal measured by the lock-in amplifier may be expressed as

$$V_{PTR}(\omega) = (I_0/2)K_{PTR}4\varepsilon\sigma_{SB}T_a^3 Z(\omega), \tag{4.4}$$

where I_0 represents the magnitude of the heating flux and $Z(\omega) = T(z=0,\omega,t)/\varphi(\omega,t)$ is the thermal impedance of the sample. The heat flux delivered by the light source is assumed to have the form $\varphi(\omega,t) = (I_0/2)\exp(i\omega t)$. To account for the instrumental factors in the measured signal, a normalization procedure is needed.

4.2.1.3. Signal Normalization

Several normalization procedures have been used for PTR measurements to account for instrumental factors summarized in [94]. These include: 1) normalizing to measurements from reference material; 2) direct measurement of the instrumental factor by allowing the heat source to pass directly to the IR detector; 3) self-normalization by normalizing the measured data from the front of the sample to that from the rear; 4) comparison of results obtaining with and without a backing liquid. In this work, the results are normalized using the electro-optical transfer function of the setup at low frequencies obtained by impinging the laser directly on a photodiode connected to the lock-in amplifier. For higher frequencies (>10 kHz) where the IR detector influence is significant for this setup, normalization is done using reference material data, in this case, well-polished steel, which is known to be homogeneous.

In the case of a signal normalized by data from a reference material, the normalized PTR signal can be represented as

$$S_n = \frac{V_{PTR,s}}{V_{PTR,r}} = \frac{P_{0,s}}{P_{0,r}}\frac{\varepsilon_s}{\varepsilon_r}\frac{T_{a,s}^3}{T_{a,r}^3}\frac{Amp_s}{Amp_r}\exp\left[i(\psi_s - \psi_r)\right], \tag{4.5}$$

where subscripts "s" and "r" denote sample and reference data. Assuming equivalent DC temperature of a given sample and reference material, the resulting normalized data is no longer dependent on the instrumetnal factor and retains the important tempereature information.

4.2.2. Lock-in Infrared Thermography

Lock-in IR thermography (lock-in IRT) was first described in [97] and has since been developed in many works [98-101] as a non-destructive testing (NDT) technique for material defects. Whereas for PTR a single IR sensor is used to obtain single signal, IR thermography utilizes an IR camera to obtain a thermal image. The ability to obtain an image in a single measurement is also its advantage over PTR. In lock-in IRT, as with other photothermal wave methods that have been discussed, periodic heating is applied to a sample. The IR camera captures a series of the resulting IR images. The temperature response of each pixel in the image is processed using lock-in techniques to deliver the amplitude and phase of the imaged material in reference to the heat source.

4.2.2.1. Description of Measurement System

For the lock-in IRT measurements, the same laser/AOM used in the PTR setup (described in Section 4.2.1.1) was used to heat the surface of the cross section of the sample at a frequency of 40Hz. A schematic of the measurement setup is shown in Fig. 4.3. An IR (wavelength 3.5 - 5.0

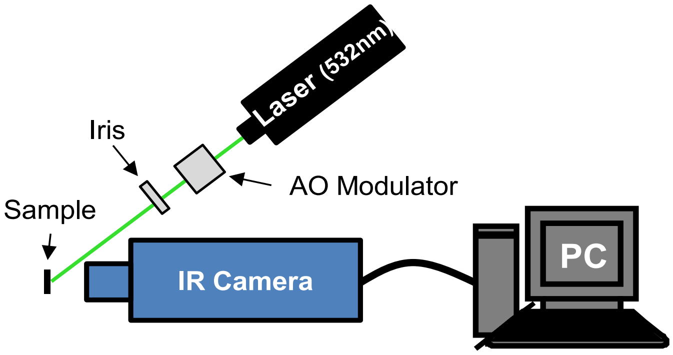

Fig. 4.3. Schematic of the lock-in IR thermography setup at URCA

μm) camera (Titanium model from Cedip Infrared Systems) with a frame rate of 100Hz recorded the periodic heating response of the sample over a period of 10 s. An internally developed software (CAMIR) at URCA was used to calculate the amplitude and phase for each pixel, at the heating frequency, using lock-in techniques. The result is both amplitude and phase images of the entire sample.

4.2.3. Scanning Thermal Microscopy

Scanning thermal microscopy (SThM) falls under the broader classification of scanning probe microscopes (SPM). Although a variety of SPM types exist, the two primary instruments used in applied research are the scanning tunneling microscope (STM) (Nobel Prize for Physics in 1986) [102] and the atomic force microscope (AFM) [103]. The STM and AFM represent some of the foremost tools for imaging, measuring, and manipulating matter at the nanoscale. Since their invention in 1982 and 1986, respectively, many variants of these devices have been proposed with applications across all fields of science. SThM was first invented in 1986 using a thermocouple probe mounted to an STM [58]. Such a configuration suffered from difficulties in distinguishing temperature from topographical variations. Later, the first images of material thermal conductivity at nanoscale were performed by Nonenmacher and Wickramasinghe [104]. Shortly thereafter, Majumdar used a contact AFM as the platform for SThM providing the flexibility to measure both conductive and non-conductive sample materials [60]. This system provided topography as well as a thermal image. Within the last decade, SThM has advanced to have spatial resolutions ~10nm, temperature precision ~50mK, and the ability to measure nanometer-scale heat flows ~10pW [2]. Comprehensive reviews of SThM topics can be found in [61, 65, 105-107].

In this work, three different AFM systems as well as different thermal probe types are used in an attempt to quantify thermal properties of unknown samples. The first AFM system, made by Park Systems, is located at the Silesian University of Technology in Gliwice, Poland. The second system, located at the Université de Reims Champagne-Ardenne in Reims, France, is a Topometrix Explorer from the mid to late 1990's. The third AFM system is made by Nanonics Imaging, Ltd., and is located at Utah State University in Logan, Utah. The following sections will distinguish between the different AFM systems. An explanation of different modes of thermal microscopy follows. As well, the variations of thermal probes used in this work will be overviewed with relation to a review of literature regarding the different approaches used to extract quantitative thermal property measurements.

4.2.3.1. Feedback Mechanisms

The basic principle of scanning probe microscopy is to control a very sharp probe with sub-nanometer precision. Therefore, the sensor, integrator, and effector of the feedback control system consists of, respectively, a tip-sample distance sensor, a computer system to process and store data from the sensor, and an x-y-z capable movement usually accomplished through piezoelectric scanners. The probe is raster scanned across a sample surface with precise control of the tip-surface distance providing maps of topography, electrical, mechanical or thermal properties, etc.

STM accomplishes the necessary feedback through the concept of quantum tunneling. The tip is brought near the surface of a sample in vacuum with a voltage bias applied between the surface and the tip. The result is a tunneling current, which is dependent on tip-sample distance, applied voltage, and the local density of states of the sample. One of the key drawbacks of this method is the requirement of a conductive sample. In the first instance of scanning thermal microscopy, a thermocouple tip was used in place of the traditional electron tunneling probe. In this case, the probe is heated while moving near the surface. The proximity of the surface reduces withdraws heat from the probe, cooling it. Thus, temperature provided the feedback mechanism for tip-surface control.

With the invention of the AFM, the feedback mechanism controlling the tip-surface provided greater flexibility for the types of samples (insulators to conductors) and for the types of thermal (or other) probes that could be used. Two feedback sensing mechanisms for the piezoelectric actuators are used in the AFM systems explored in this work: optical based and tuning fork based.

Optical Detection

The feedback signal/sensor used by the Park Systems and Topometrix AFM systems, which is also the most common from several AFM manufacturers, is the detection of cantilever deflection using optical means. A schematic diagram of this configuration is shown in Fig. 4.4a. Typically, a laser is reflected from the cantilever of the probe onto a bi/quad-cell photodiode. With knowledge of the stiffness of the probe, the force exerted by the probe on the sample surface can be calculated and maintained constant. This is also known as a static mode of operation. Such a configuration allows moving the probe across a surface with precisely controlled pressure and is often times referred to as contact AFM.

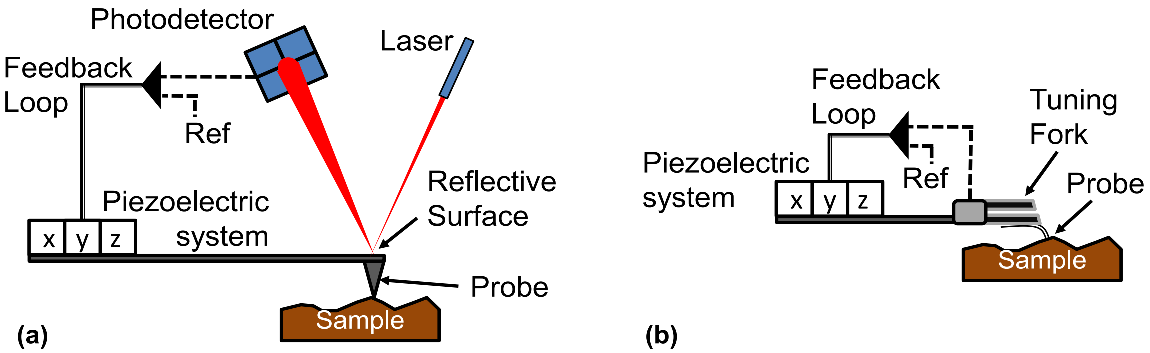

Fig. 4.4. Schematic view of AFM probe feedback mechanisms: a) optical; b) tuning fork

Tuning Fork Detection

The second type of feedback, which is used by the Nanonics AFM, uses a unique piezoelectric tuning fork [108, 109] as is illustrated in Fig. 4.4b. A photograph of the tuning fork is shown in Fig. 4.5. In this case, the probe (discussed in a following section) is rigidly attached to one of the prongs of the tuning fork, which is also rigidly attached to an external piezoelectric vibrator. The fork is vibrated at resonance (~30-40 kHz) as the probe approaches the sample surface. The resonance generates a piezoelectric potential proportional to the tip oscillation amplitude, which is fed into a lock-in amplifier. This piezoelectric signal is the sensor in the control feedback of the system. The implications of the tuning fork tip control mechanism on thermal measurements are less clear than the optical feedback mechanism. The literature states that under feedback control the probe maintains tip-sample distances within tens of nanometers. The effects of tuning fork feedback control system on thermal microscopy merit further consideration, beyond the scope of this work. This mode of operation is a dynamic mode referred to as non-contact AFM.

4.2.3.2. SThM Modes of Operation and Instrumentation

For typical SThM measurements, the probe may act passively as a temperature sensor, and at times, as an active heat source as well. These modes of operation are then distinguished as passive SThM or active SThM. In passive mode, a small current is applied to the probe so the

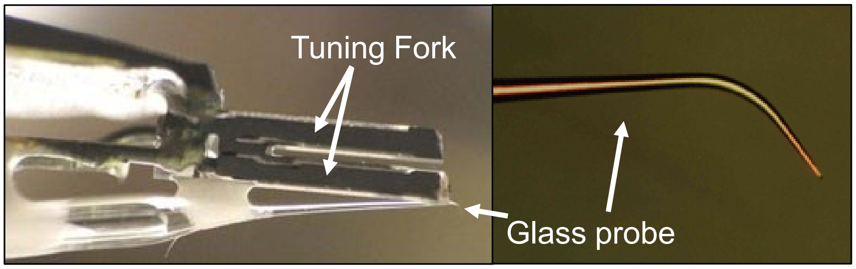

Fig. 4.5. Photograph of (left) glass-pipette probe mounted to piezo-electric tuning fork and (right) glass probe from Nanonics Imaging, Ltd. [109]

change of temperature-dependent electrical resistance may be measured or in the case of thermocouple tips, the Seebeck voltage may be directly measured.

In the active mode, a current is applied to the probe tip to raise its temperature. The current may be applied in a constant fashion or as the feedback-controlled parameter in a constant temperature mode, where the probe resistance ($\propto$ temperature) is maintained constant. The heating of the probe tip drives heat transfer between the tip and a sample under measurement. Measurement of the temperature change of the probe tip (constant current mode) or of the power dissipated into the sample (constant current mode) is then correlated to the thermal conductivity of the sample.

In SThM, the excitation current applied to the probe may be either DC or AC. When using purely thermoresistive probes, both configurations rely on the linearity of the relation between electrical resistance of the probe circuit and its temperature. Using an AFM as a platform, common SThM configuration is to place a thermoresistive probe as one of the legs in a Wheatstone bridge configuration.

DC

In pure DC mode, the heating current is applied to the probe in either constant current or constant temperature modes. In constant current mode, the measured change of voltage across the probe is proportional to the temperature change in the probe sensor. If a thermocouple probe is used the measured Seebeck voltage is directly proportional to temperature. On the other hand, constant temperature mode has the advantage of maintaining a more constant temperature difference between the probe and the sample. This is accomplished through adjusting the heat rate delivered to the sample. In this way the measured changes of power applied to the tip during operation should better represent changes of tip-sample thermal conductance. Typical schematics for the Wheatstone bridge thermal circuits used in DC SThM modes are shown in Fig. 4.6.

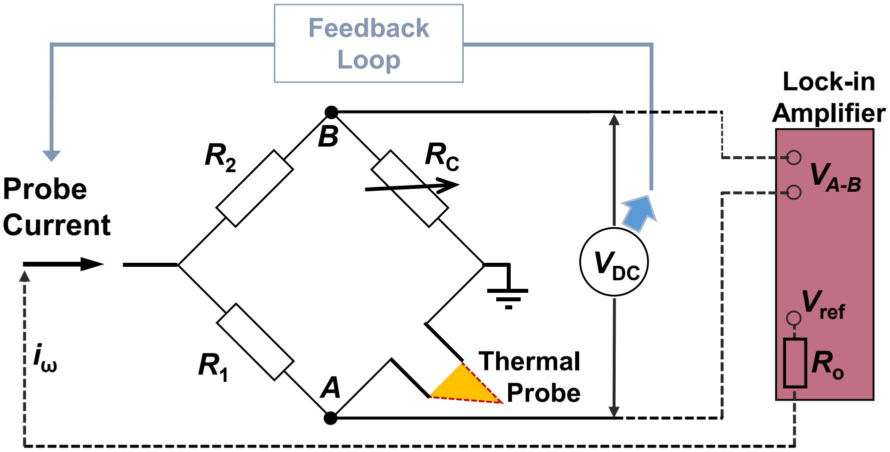

Fig. 4.6. Schematic of typical configurations for SThM measurements in DC mode. The feedback loop is for constant temperature operation while the dashed lines connected to the lock-in amplifier are for AC operation.

AC

AC operation has the advantage of lock-in signal processing, which results in higher sensitivity, stability, and resolution than DC methods. In this mode of operation, a modulated heating current is passed to the thermoresistive probe. For DC+AC excitation, the resulting voltage across the probe has three primary harmonic components including 1ω, 2ω, and 3ω. With pure AC current, only the 1ω and 3ω components are contained in the voltage signal. The resulting amplitude and phase of the harmonic components are measured with a lock-in amplifier. A brief explanation follows regarding the relationship of measured voltage and temperature. For an applied harmonic current, $i_\omega \propto \exp(i\omega t)$, the power generated through a resistance is proportional to the second harmonic, which will also be proportional to the change of temperature, $P \propto \Delta T \propto \exp(i2\omega t)$. Due to temperature dependence of resistance, $\Delta R \propto \exp(i2\omega t)$. The resulting resistance change therefore generates higher harmonics, $\Delta V = i_\omega \Delta R \propto \exp(i3\omega t)$

The third harmonic is directly proportional to the AC temperature rise in the sample. When it is used as the measured signal, the technique is termed 3ω SThM. As is common for DC operation, in AC mode the probe is placed in a Wheatstone bridge configuration in order to cancel the 1ω component of the signal when in 3ω detection. The basic electrical schematic for AC configuration is shown in Fig. 4.6 where R_0 represents the output impedance of the signal generator, V_{ref} is the applied reference voltage, and $V_{\mathrm{A\text{-}B}}$ represents the difference of input voltages across the bridge measured in the lock-in amplifier.

AC excitation is equivalent to DC excitation in terms of the thermal information measured from a sample. The lateral resolution is determined by the size of tip-sample contact area. This statement is valid also when the SThM is operated in the ac mode and is known as the super-resolution effect of thermal wave probing [110]. It is due to the fact that the thermal diffusion length in the sample at the used modulation frequencies (up to tens of kHz) is still much larger than the size of the contact area. The ac and dc modes provide the same information about the sample [61]. Therefore, active (sample heating), single-tip SThM measurement is not a true thermal wave method in the sense that probing (heating) depth is not controlled by heating modulation frequency. In other words, unlike the other thermal wave methods described in this work, the spatial resolution of measurement is not determined by heating frequency, but only by contact radius.

4.2.3.3. Probe types

Over the course of more than two decades, many variations of thermal probes have been explored in the literature. Much of this effort has been driven by the push for smaller spatial resolutions. The primary categories of thermal probes include two types: thermoresistive and thermocouple. Of those that have been studied only a few have been made available commercially. In this work, several commercial probes have been explored for viability in measuring the irradiation damage in an ion-irradiated sample. These probes types include the Wollaston-wire, batch-fabricated-thin-film, and glass-pipette types including both thermocouple and thermoresistive sensors.

Wollaston Wire

Of all SThM probes, the Wollaston wire probes first produced by Dinwiddie et al. [59] are the most studied and well understood (SEM image shown in Fig. 4.7). These probes are commercially available from Bruker Corp. These hand-made probes consist of a Wollaston wire that is bent to form a tip, which is then etched to remove the silver cladding exposing a V-shaped, 5 μm platinum core. Each leg of the two sides of the platinum "V" is approximately 100 μm long. In measurement the apex of the tip is then placed in contact with the sample while the resistance of the exposed platinum is monitored. The manual fabrication process results in less than ideal reproducibility from probe to probe as will be shown in the results of this work.

Thin Film

The second most common thermal probes belong to a class of batch fabricated thin film probes, which are also commercially available [111]. SEM images of the probes are shown in Fig. 4.8. First manufactured by Mills et al. [112], the batch fabrication process has resulted in better reproducibility of probes and improved spatial resolutions. The probe used in this work consists of SiO_2 substrate with a thin palladium (Pd) ribbon near the apex of the tip.

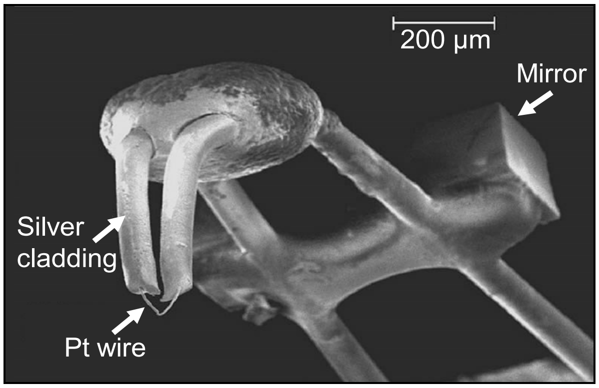

Fig. 4.7. SEM image of Wollaston wire probe

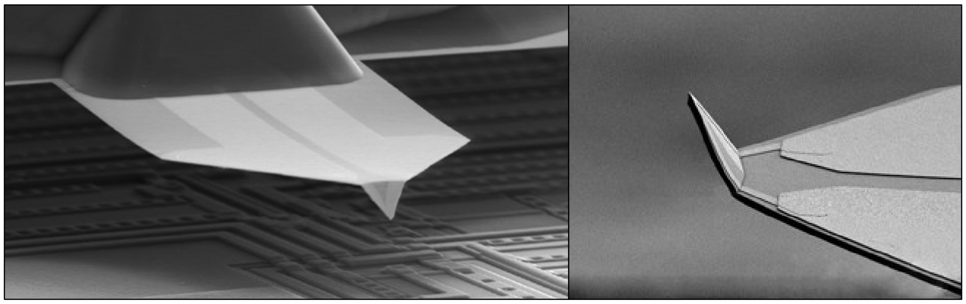

Fig. 4.8. SEM images of batch-fabricated, thin-film probes manufactured by Kelvin Nanotechnology Ltd. [110]

Glass Pipette

The glass-pipette thermal probes [113] are a less common type available from Nanonics Imaging, Ltd [109]. Both thermocouple and thermoresistive thermal probes are available (Fig. 4.9). The thermocouple type are fabricated by placing a platinum wire inside a borosilicate glass tube. Using a pipette puller, the composite wire assembly is drawn down resulting in a probe tip consisting of a platinum core ~100nm in diameter and a surrounding glass tube with outer diameter ~0.5 μm [114]. After pulling the second thermoelectrode for the thermocouple is made by a vacuum-evaporated thin gold film coating over the entire probe tip. Thus, the temperature sensing junction is at the interface of the exposed platinum end and the gold film coating.

The thermoresistive probes are fabricating using similar glass pulling technology as the thermocouple type. However, in this case the two platinum wires insulated from one another are

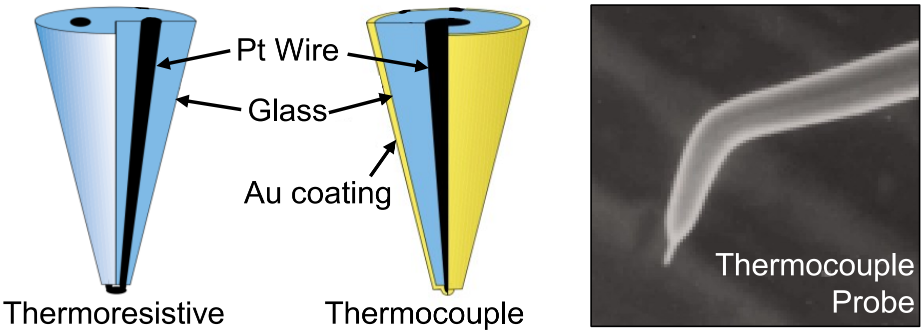

Fig. 4.9. Schematic drawings of (left) thermoresistive and (middle) thermocouple-type probes available from Nanonics Imaging, Ltd. [109] (right) SEM image of thermcouple probe.

contained within the glass during the draw-down operation. After the pulling operation, the isolated wires within the glass are exposed to a length of a few microns by an etching procedure and then fused together by heating. The tip wire diameters are ~100 nm-500 nm [115].

4.2.3.4. Quantitative Analysis

Despite more than twenty years of research focus, quantitative interpretation of SThM results remains a challenge. The key to this challenge is to relate the temperature measured by the probe to the sample temperature [2]. This relationship has been studied by many over the past twenty years with specificities related to each type of thermal probe used. Common to most probe configurations, an energy balance on a thermal probe in contact shows that the key heat losses are through direct conduction from the tip to the sample, conduction/convection from the probe through surrounding air or water meniscus, and conduction through electrical leads and the cantilever, away from the probe apex. Typical heat transfer mechanisms for SThM probes are illustrated in Fig. 4.10. Heat transfer losses from the probe other than those to the sample affect its sensitivity to sample measurement. Effects of radiation heat transfer have been shown to be relatively negligible [106].

The key heat pathway from the probe heating/sensing element to the sample is comprised of several thermal conductances including within the tip itself, tip-sample contact resistance, through a water meniscus formed at the contact, through surrounding gas, and into the sample. Several groups have studied these effects [116, 117]. The effect of the water meniscus for a Wollaston ThP was shown experimentally in [118]. They concluded that up to near the boiling point of water, conduction through the water meniscus is dominant. They also show that the relative magnitudes of heat transferred by each mechanism are influenced by the thermal conductivity of the sample. Later, these conclusions were corroborated by theoretical/experimental work by [119]. They show the importance of the heat path through the

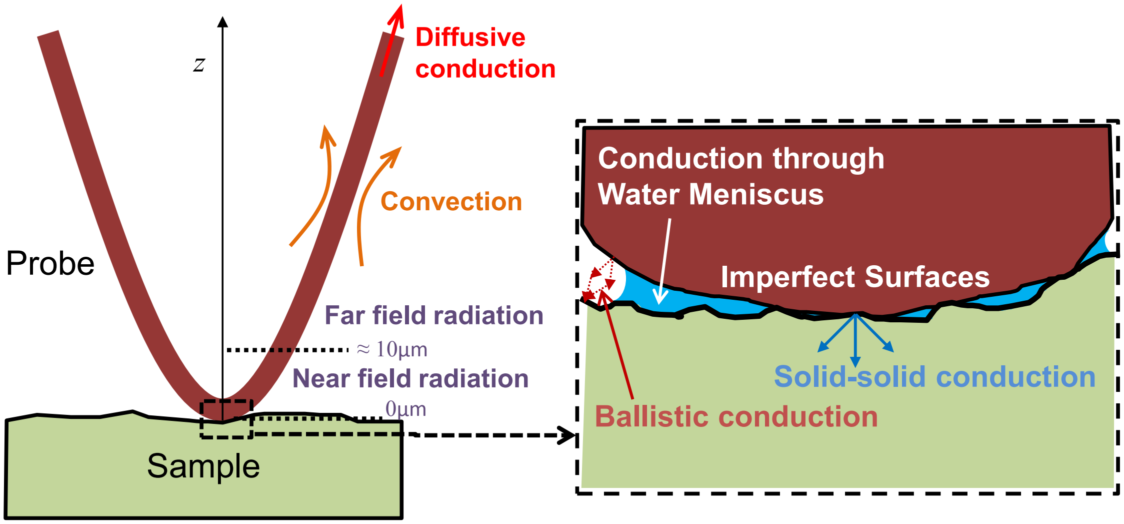

Fig. 4.10. Relevant heat transfer mechanisms for SThM probes (adapted from [106]).

air and its influence on an effective heat transfer radius between a Wollaston wire tip and a sample. This conclusion was further demonstrated for the heat transfer through air between a hot nanometer-sized tip and a sample [120].

More recently, promising results have been obtained using methods intended to isolate the heat path between the probe tip and the sample. In one case, a sophisticated double-scanning procedure allows for the probe to pass over a sample twice. During the second scan, the probe is raised slightly from the surface to provide a background measurement. The second measurement is subtracted from the first to give primarily the effect of the tip-sample contact [121, 122]. The second approach has been to operate in high vacuum, which has been shown to eliminate the influence of air and water on the measurement providing better resolution [8, 123]

One important consideration regarding use of a thermoresistive probe is that the measured signal corresponds to the average temperature of the resistive element, meaning degradation of spatial and temporal resolutions. One implication of an averaged temperature value is a measurement dynamic range = 4 for a Wollaston wire probe [61]. On the other hand, the dynamic range of a thermocouple probe with a local temperature measurement at the probe apex would imply a theoretical dynamic range → ∞. The more localized the temperature sensor is to the probe apex, the greater the dynamic range of the measurement.

4.2.3.5. Modeling Approaches

Proper modeling of the heat transfer in a thermal probe is crucial for extracting quantitative information. Several models have been derived in the literature and should be discussed in context of the probe type as well as whether excitation is DC or AC. In general, most approaches follow the well-known theory of hot-wire anemometry. Common modeling approaches are 1-D fin analysis [61, 124, 125], lumped model [126-128] and numerical approaches [126, 129].

CHAPTER 5

RESEARCH PLAN

This chapter presents a task list for accomplishing the objectives of the work. A key strategy to this work is to draw on the expertise of leading experts in the fields of thermal property measurements. These collaborative efforts will be illustrated through the following task list. Each section in the chapter briefly delineates the process followed for each of the major tasks outlined in Table 5.1.

Table 5.1. Outline of main tasks to accomplish the objectives of the dissertation

Section	*Tasks*
5.1	Material procurement and sample preparation
5.2 & 5.3	In-depth measurement of thermal property profile with SThM • Measure ability of different SThM systems to sense thermal property variation in the proton-irradiated ZrC – Thin-film probes/Contact AFM (SUT, Poland) – Wollaston probes/Contact AFM (URCA, France) – Glass-pipette probes/Non-contact AFM (USU, USA) • Measure in-depth thermal property using lock-in IR thermography • Measure in-depth thermal property using focused-heating, front-detection photothermal radiometry
5.2 & 5.4	Quantify thermal property modification by irradiation effects • Calibration of SThM probe signal • Photothermal radiometry measurements using various configurations
5.5	Correlate irradiation damage effects to measured thermal characteristics

5.1. Material Procurement and Preparation

Proton-irradiated ZrC is to be obtained from the University of Wisconsin-Madison in the form of a 3mm diameter disk. The sample is to be high-purity with well-defined stoichiometry. In order to directly measure the in-depth profile, the sample will need to be section in such a way as to minimize altering the irradiation effects in the interior. This will be accomplished through careful fracturing of the disk to isolate a small piece that will have the exposed cross-section. Using sample preparation equipment at the University of Utah, the cross-section can be mounted in epoxy resin with the exposed cross section on the surface. The remaining ZrC disk can be used directly with tomographic thermal-wave methods.

5.2. SThM Measurement and Calibration

A large focus of this work is to explore the viability of using SThM to measure ion-irradiated materials. Therefore, a significant effort will be placed on exploring the capabilities of various SThM systems to detect these changes. The first step in this process is to perform detailed review of literature related to quantified SThM measurements. The first measurements will be done at the Silesian University of Technology (SUT) in Gliwice, Poland. The Department of Applied Physics at SUT is one of few that is actively pursuing the development and application of using thin-film SThM probes for quantifiable thermal conductivity measurement. Both DC and AC SThM techniques will be utilized. This work will be sponsored through an NSF International Research Fellowship.

The second SThM system to be explored is located at URCA in Reims, France through sponsorship of the Chateaubriand Fellowship from the Embassy of France in the U.S. Wollaston-wire thermal probes will be used to measure the proton-irradiated sample using different SThM configurations including DC, AC, and micro-thermal analysis.

Lastly, the laboratory at USU will be acquiring an AFM system in late 2011. After returning from France, the new AFM system at USU will be explored. This task will require significant effort to gain an understanding of the system control and manipulation as it will be brand new. Thermal measurement capability of the system will be tested, in particular, in relation to the proton-irradiated ZrC.

In all cases, the ability to sense a change of thermal properties on various samples will first be explored to measure their individual sensitivity to sample thermal conductivity. In the case that thermal conductivity variation is detectable in the ZrC sample, thermal models from either the literature will be used/adapted where possible to extract quantified information or will be formulated as needed.

5.3. Other In-Depth Profiling of Thermal Conductivity

As a means of validating and comparing measurements of resolutions small enough to detect sharp variations in irradiation-damage profiles, lock-in IRT and PTR will be used to measure in-depth *k* profile. Each of these systems are available at URCA. The lock-in IRT system is frequency-limited to < 100 Hz. The PTR system is limited by the heating focus size vs. measureable signal. Such measurements have not been performed before on irradiated materials and will be useful to validate a thermal profile that may be obtained from SThM.

5.4. Tomographic Photothermal Radiometry

Associated to a valid thermal model with properly determined parameter dependencies, tomographic PTR measurements will provide quantified thermal property information about the irradiated ZrC that can be compared to quantified data obtained from SThM measurements. The thermal profiles will be obtained from the thermal profiling techniques discussed in Sections 5.2 and 5.3. A parameter sensitivity will be performed to understand the frequency ranges of greatest sensitivity to the parameters of interest. The irradiated ZrC will be measured using the PTR setup at URCA. Effects of 1-D and 2-D heating will be explored to verify appropriate measurement configuration for the thermal models used to extract data. Two normalization procedures will be tested for the proton-irradiated material including comparison with a reference material and self-normalization. A sample of non-irradiated ZrC will be measured to obtain the virgin ZrC, which comprises the substrate layer of the irradiated sample. These data will be used to validate data from the spatial measurements.

5.5. Correlation of Irradiation Effects to Thermal Conductivity

Using the known proton-irradiation characteristics for similar conditions from work done by the University of Wisconsin-Madison, the observed thermal profile and level of degradation of thermal conductivity will be discussed. These results will be placed in the context of the few existing irradiation studies of thermal transport in ZrC and other metal-ceramic materials.

CHAPTER 6

IN-DEPTH THERMAL PROPERTY PROFILE RESULTS

As was discussed in Chapter 3, ion irradiation penetrates a certain depth into a material before losing energy and stopping. The depth is dependent on particle type, energy, target material, etc. The damage level (correlated to thermal transport) at various depths into the material also depends on these parameters. The resulting overall damage profile and depth may be estimated using numerical simulation such as that described in Sec. 4.1.2 or by TEM studies as in [87]. Knowing the exact profile in a given material is crucial for applying various tomographic thermal wave techniques as the results are dependent on the assumed thermal model.

In this chapter, three techniques are explored as spatial profiling tools to directly measure the thermal conductivity profile in a proton-irradiated zirconium carbide sample for the first time. For these measurements, the cross-sectioned sample is measured to capture the in-depth profile as shown in Fig. 6.1. The work presented here has been published in [130, 131]. First, a presentation of SThM results is given. Measurement results follow from two thermal wave techniques, spatial-scanning PTR and lock-in IR thermography, with an overall comparison of the applied techniques. For these measurements, the cross-sectioned sample is measured to capture the in-depth profile.

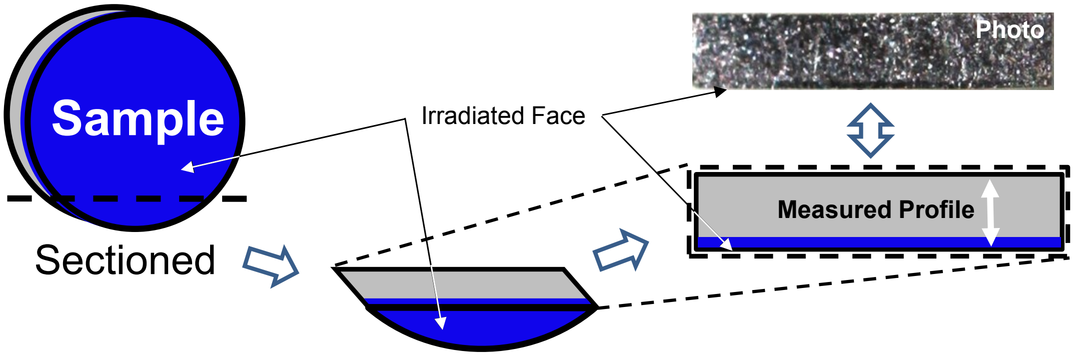

Fig. 6.1. Schematic representation of sample used for in-depth profiling measurements.

The first profile measurement results presented are taken from SThM. Although measurements were taken using three different SThM probes (and several probes of each type), the best results were obtained using a particular Wollaston-wire probe. Due to the thermal conductance relationship being a combination of thermal properties at the contact as well as the physical nature of the contact, great care was taken to verify the measured k profile is independent of imperfect sample topography. Finally, the resulting overall thermal profile is constructed by overlaying several thermal line profiles.

In conjunction with SThM profiles, focused-heating PTR was spatially scanned across the profile and lock-in IRT was used to image the cross-sectional surface. For the PTR spatial scans, the heating spot size was ~50 μm with a heating frequency of 1 MHz. The result of the scans revealed a clear layer of degraded thermal conductivity. Lock-in IRT images were taken at heating frequencies of 10 Hz, 20 Hz, and 40 Hz. From the images the damaged layer is clearly evident. Line profiles were extracted from the image to provide an overall thermal profile that is consistent with the other profiles obtained.

The shape of the numerically calculated, irradiation-damage profile compares well with the resulting profile of k degradation. A relatively thick and constant diminished k value is revealed through the majority of the damaged zone, consistent with characteristics of proton irradiation. A sharp transition of thermal signal to the non-irradiated material was found at the rear of the profile, with no indication of the very thinly peaked damage zone seen in the numerically calculated damage profile.

6.1. Scanning Thermal Microscopy

Due to its capability of high spatial resolution measurement, SThM presents itself an ideal candidate for thermally profiling thin layers by direct means (as opposed to tomographic). Because of the many challenges associated with quantitative measurement, great effort was expended in an attempt to obtain a thermal profile from the proton-irradiated ZrC. In fact, measurements were made from three distinct AFM systems located in laboratories in three different countries. The results presented in this work were primarily obtained using a TA Instruments μTA 2990 Micro-Thermal Analyzer equipped with a Wollaston-type thermoresistive probe. The system platform is based on an atomic force microscope (AFM) using optical feedback to control the probe contact force on the surface. All measurements performed in this work are with the system in the constant temperature mode (i.e. thermal conductance mode). The power dissipated in the probe tip is measured, which is correlated to the *k* of the sample.

The general procedure undertaken in this process was to first attempt to measure variation of thermal conductivity in various reference samples as different probes, even of the same type, showed varying sensitivity. In this section, the topography of the ZrC sample is described in detail through selected AFM measurements. Then, the thermal profiling results will be presented. Lastly, some of the challenges and observations made during these measurements across three different SThM systems will presented.

6.1.1. Topography

Because the measured thermal conductance of a sample is directly proportional to the product of thermal conductivity and the contact size, the topography of a sample plays a key role in measured signals. The effect of the sample surface can alter the contact as the tip moves across the surface. For this reason, it is extremely important to distinguish topography effects from thermal effects of the sample.

Surface topography, characteristic of the ZrC cross-section surface, are presented in Fig. 6.2. In Fig. 6.2(a-b), topography results obtained using a Wollaston-type probe are shown for the first 100 μm from the irradiated surface. Evident from the presented profiles, the surface is not ideal, showing variations in slope and with "hole-like" defects of varying sizes scattered across

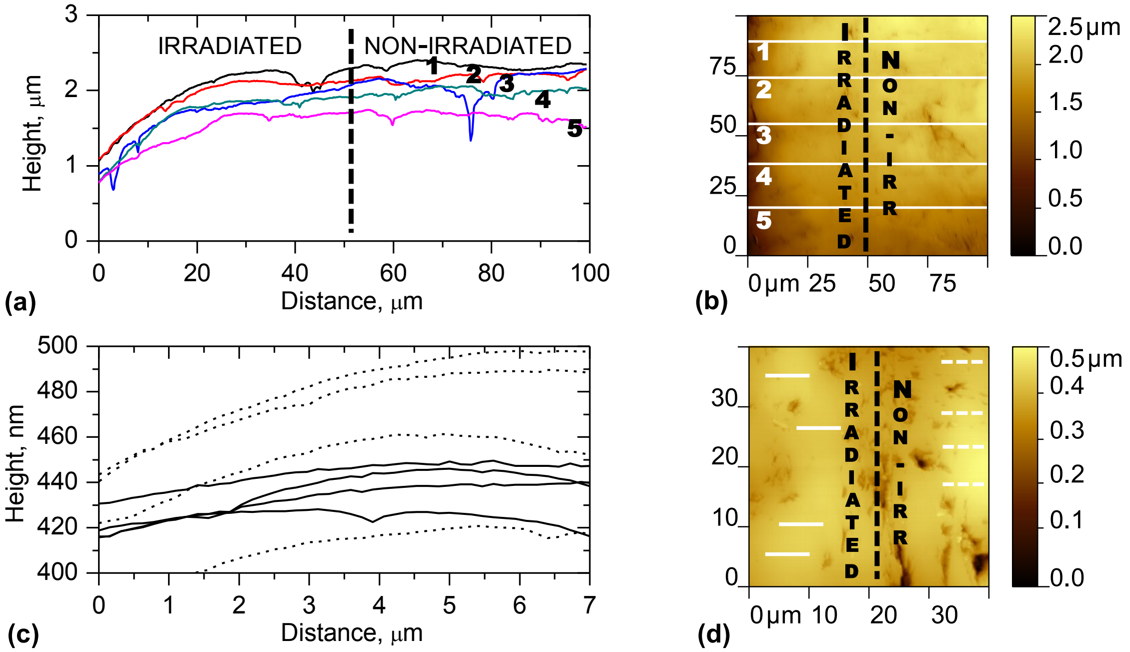

Fig. 6.2. Topographic images of the ZrC cross section with the irradiation damaged zone indicated in the figures. (a) and (b) show line profiles and image for 100 μm square region acquired with Wollaston tip; the left side in both figures is near the edge of the irradiated surface. Numbers indicate corresponding profiles. (c) and (d) show images acquired with higher resolution AFM contact tip showing a roughness value of <5 μm. Line style correlates to image zone: solid – irradiated; dashed – non-irradiated

the surface. Near the edge of the sample, the surface is rounded with an increasing slope towards the irradiated surface. The marked center of the image is the approximate division between the damaged and virgin sample. No clear distinction may be made between the two zones except for concern related to the slope near the edge of the sample, which is found to affect the signal primarily near the edge as will be shown in the thermal results.

In Fig. 6.2(c-d), images are shown that were made by an AFM contact tip having much better spatial resolution than the Wollaston wire tip used in the thermal measurements of this study. Again, the center of the image in Fig. 6.2(d) marks the approximate boundary between damaged and undamaged zones. The profiles extracted from the image as well as surface statistics taken on the smoother regions of the sample show small roughness (Ra < 5 nm) and no clear differences between the two zones.

From these results, the topography will certainly influence the conductivity results between different locations on the sample. However, with careful consideration, the thermal signal over the "flat" regions of the sample should be generally comparable allowing for a quantitative relationship between the two zones. In all cases, great care was also taken to ensure the sample surface was aligned with the lateral scan directions of the microscope.

6.1.2. Thermal Profiles

The measured thermal power profiles with the SThM in active mode (thermal conductance profiles) of the sample are presented in Fig. 6.3. The absolute values of thermal power are irrelevant in these images; and a more quantitative interpretation will follow in Section 7.1.1. The irradiated surface is ~15 μm farther to the left in Fig. 6.3(a-b). The images provide a clear contrast between the two zones and, by inspection with the eye, reveal rather uniform levels in two distinguishable zones. The damaged zone is the darker zone (lower dissipated power meaning lower thermal conductance). The scan direction was left-to-right in all images shown, thus each line contains a good relative contrast between the two regions.

At first glance, the thermal conductance profiles presented in Fig. 6.3(a) appear quite noisy. Upon closer inspection, the upper levels of each of the extracted profiles correspond to regions of the sample where the signal level is most comparable, reproducible, and has relatively good stability, and thus indicating the thermal signal corresponding to the thermal conductance of the sample. A comparison of probe power to measured height is presented in Fig. 6.3(c) to better illustrate their relationship. The many dips in probe power represent many "defect" structures on the sample where thermal conductance decreased (due to surface roughness and/or possible differences of material composition). Therefore, by examining the upper levels and piecing together from different lines in the image, one can see an average profile, directly correlated to the k of the damaged zone into the virgin material. The resulting profile is unique, not found

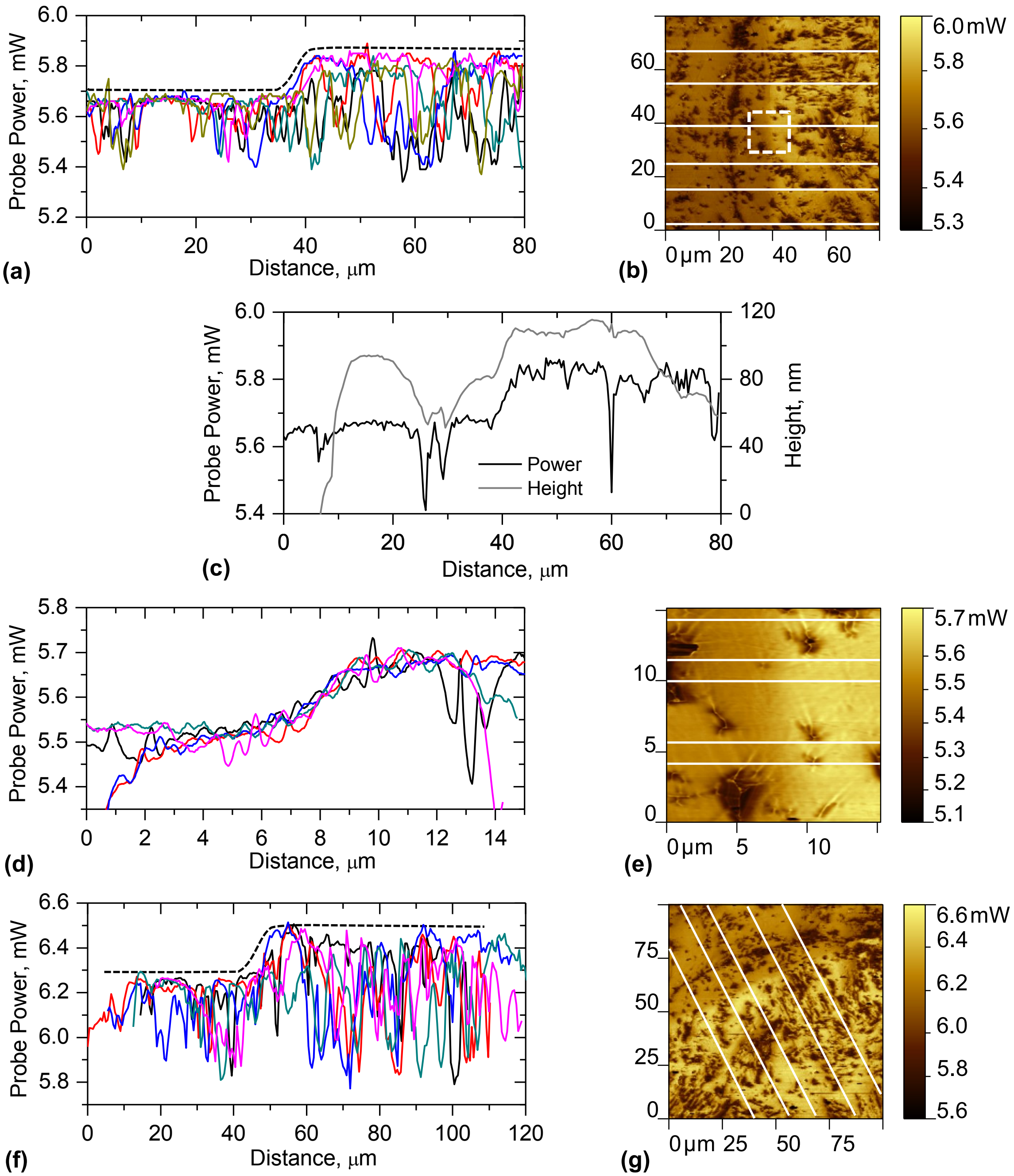

Fig. 6.3. Thermal profiles across irradiation damaged layer showing clear contrast and transition between irradiation-damaged and non-irradiated zones. (a) and (b) show 80 μm square region – left side is ≈15 μm from irradiated surface edge. (c) shows a comparison of probe power to height for a single profile taken from (b). (d) and (f) show a 15 μm square zoom of the boxed location marked in (b). The transition between damaged and undamaged material spans 3-4 μm. (f) and (g) show approximately the same location on the sample, scanned at an oblique angle. Dotted lines in (a) and (f) are to indicate the general thermal conductivity profile in each location represented by the upper level of the combined line profiles.

elsewhere in the open literature. *k* appears quite constant through most of the damaged zone with a small transition zone to the bulk, undamaged material.

For an idea of the uncertainty of the profile measurement, from Fig. 6.3(a), the span between ≈15-20 μm (flat and mostly free of defects) is most representative of good surface conditions on all extracted profiles where the fluctuations are no more than ±0.05 mW from the absolute level of 5.6 mW. In other locations defect-affected signal from other extracted profiles mask the low variation of signal in other flat, smooth surfaces. This idea is illustrated further in Fig. 6.3(c) as it is a zoom on a region where the influence of defects is more obvious.

The results of a zoomed scan of the region indicated by the box in Fig. 6.3(b) are shown in Fig. 6.3(d-e). The extracted profiles shown in Fig. 6.3 show a transition occurring over a zone having ~3-4 μm thickness. Interestingly, no strong evidence of a more damaged intermediary layer was found. Therefore, no intermediary layer of higher damage is assumed in the thermal model used for fitting PTR data in the following chapter. The measurements of Fig. 6.3(f-g) are of approximately the same region as Fig. 6.3(a-b) (look for identifiable features in both images to correlate location) scanned at an oblique angle. The profiles shown in Fig. 6.3(f) have been shifted laterally so that the transition region for each individual profile approximately lines up. The resulting profile is similar to that shown in Fig. 6.3(a) proving the independency from scan orientation. As mentioned in the section discussing topography results, edge effects due to rounding caused by polishing are evident in the reduced signal in the first 10 μm of the profile.

6.1.3. Additional SThM Observations

In this section, the difficulty of obtaining quality SThM measurements is illustrated through comparisons of results from various SThM probes and systems. First several thermal images taken with various Wollaston wire probes are presented and discussed. This will be followed by images taken from thin-film type and glass-pipette type probes. The results presented are taken from the same ZrC sample that was presented previously in exactly the same location. Certain distinguishing features of the location will be apparent in each image allowing for direct comparisons.

6.1.3.1. Probe-to-Probe Variation of Measurement Results

Due to the difficulty in fully characterizing tip-sample contact, results from various SThM tips may vary significantly. In truth, even results from the same tip can vary from one measurement to another due to damage, environmental changes, tip contamination, etc. Therefore, such studies as were done on the ZrC sample require great patience and care in ensuring the quality and accuracy of the results. For this work a series of more than 150 thermal images were recorded using Wollaston wire probes alone. Great variation was found between many of the probes used.

In Fig. 6.4, several images are presented to illustrate the effect of different probes on the sensitivity to the thermal contrast between the irradiated and non-irradiated zones. The figures present the relative contrast of the image in terms of the dissipated power in the irradiated, P_{irr}, and non-irradiated zones, P_{ZrC}, as $(P_{\mathrm{ZrC}}-P_{\mathrm{irr}})/P_{\mathrm{ZrC}}$. These results begin to illustrate the variation of results when using such probes. In each of the images presented, thermal contrast is apparent

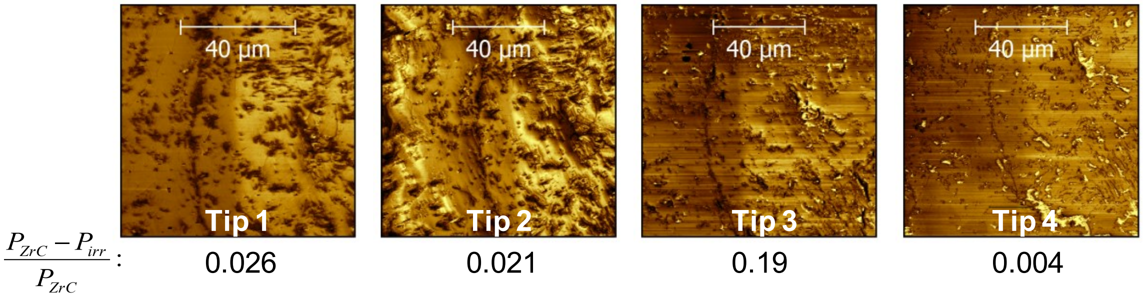

Fig. 6.4. Several SThM images taken in constant temperature mode using different thermal tips. The results illustrate the variation of effects from using different Wollaston probes. P_{irr} and P_{ZrC} are the average power dissipated in the irradiated (left) and non-irradiated (right) zones. Not shown are images from other tips that showed no thermal contrast between the two zones.

between the damaged and undamaged zones. The relative contrast between each of the four images shown is from 0.026 down to 0.004. Not shown are results that had no contrast between the two zones. Such variation can be challenging especially when initially looking for such differences as demonstrated by the irradiated ZrC material.

Also seen in Fig. 6.4, the effect of topography on results varies depending on each tip. For Tip 1 (used for the data presented in Section 6.1.2), the thermal contrast is the best. Also, those results show the least variation due to topography effects. The other images show more variation, which is most likely caused by variation of the probe tip geometry and surface characteristics. For Tip 2, moving towards the left edge the measured signal seems to, on average, rise but then drops off sharply. This is most likely due to a sloping topography that increases tip-surface contact, but then as the edge is approached the contact is reduced to zero. Other variations are observed in the images where “darker” or “lighter” spots vary across the surface.

Due to the large variations observed from tip to tip, several Wollaston wire probes were imaged using an SEM to compare to the tip with the best and most consistent thermal contrast. The images of three probe tips are presented in Fig. 6.5. Tip 1 is from the same probe used for the results in Section 6.1.2. The other two tips were taken from a new box of probes that all showed a general low sensitivity to thermal properties. The images of Tip 1 were taken after much use and it had broken just to the side of the tip extremity. In the top image, the wire running to the left shows slight ridges that seem to disappear at a certain point that has the appearance of being coated.

Using electron-dispersive X-ray spectroscopy (EDS) in the SEM, carbon seems to be a major constituent of the “coating.” The other two tips shown have quite large radii of curvature (also noticeable by the naked eye). Very clear from the images is the “rough” and variable surface. Large ridges run axially down the wire. Coupling these effects with sample surface

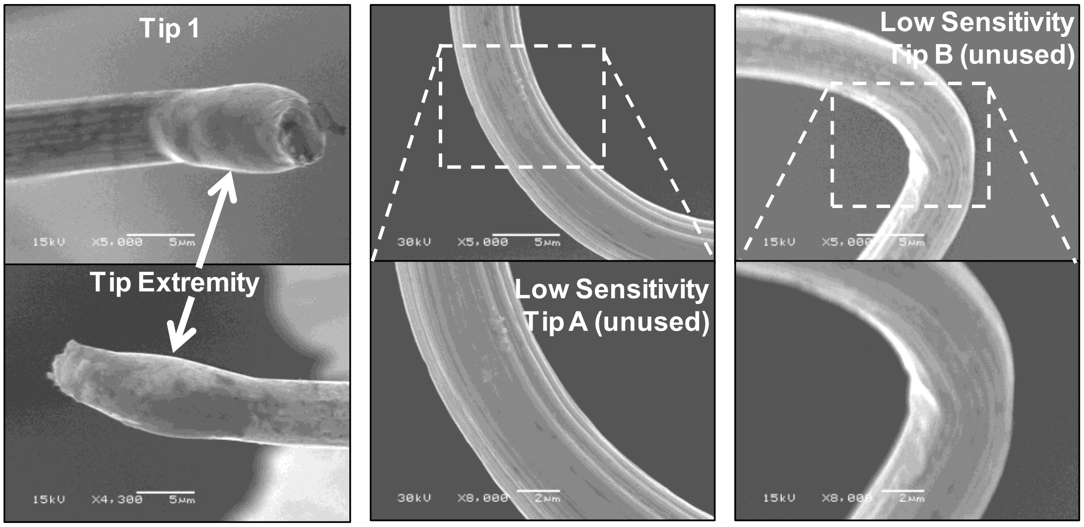

Fig. 6.5. SEM images of various Wollaston wire probe tips – for reference the wire diameter in each is ~5 µm. Tip 1 is from the probe that provided the best and most consistent thermal contrast (shown broken on one end.) It has the appearance of having collected carbon material at the extremity (verified by EDS analysis). The other two tips (A & B) are from new probes that all demonstrated low or no sensitivity to the ZrC material. The images illustrate the variation of probe contact surfaces.

imperfections could have dramatic effects in terms of signal variation as the tip moves across the surface.

The relative good performance and the appearance of Tip 1 has lead to some questioning as to the explanation. Previous to measurements on ZrC, Tip 1 had been used on a polymer material. Therefore, one explanation for its appearance is that the extremity had been coated by a polymer material. To clean the tip, it had been cycled to high temperature ~450°C. In doing so, the polymer may have been reduced to a carbon deposit, the effects of which being unknown. However, the overall sensitivity of the tip was enhanced relative to any other tip tested (>10 tips). Whether a true coating or not, the images also show a much smoother and somewhat more rounded surface near the extremity of the tip. This would imply a lesser variation from the tip side of the tip-sample contact and may explain the low variation of measurement signal seen with Tip 1, even with sloping topography.

Finally, another phenomena observed with all probes tested is demonstrated in Fig. 6.6. In this case, the displayed thermal images show a clear contrast during the scan, which is attributed to contamination of the tip extremity. In both images, the upper portion of the scanned region shows almost a negative result of the lower portion. The defect features exhibit higher signal as compared to the flatter regions. This effect may be explained by the contribution of an additional thermal resistance at the tip extremity. On the flat surfaces, the thermal resistance acts to decrease heat flow to the sample. When passing through the defect regions, the region of the tip in contact with the sample varies to locations with less resistance. The image on the left shows an abrupt transition from "contaminated" to a more typical function. At right, the transition is a bit more gradual. Such effects have been observed with all AFM tips tested during this work (thin film, Wollaston, glass-pipette).

6.1.3.2. Glass-Pipette Probes with Tuning Fork Feedback

The AFM system located at USU has been explored preliminarily to gauge its relative ability to sense thermal contrast. The following is brief summary of thermal measurements to date with only a few thermal measurements made thus far. The first example shown in Fig. 6.7 is a sample of SiO_2 wafer that has a Pt coating (~1 µm thick) on the left side. It was used as a baseline

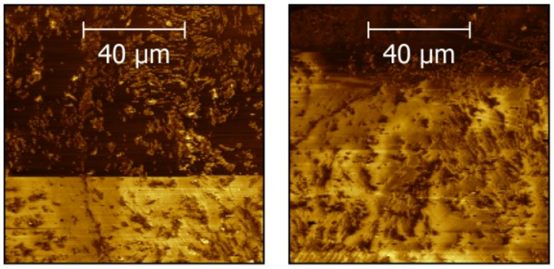

Fig. 6.6. Thermal images on irradiated ZrC cross-section where an abrupt anomaly occurs during the scan. The difference seen in the upper portion of the scan is most likely due to additional thermal resistance at the tip extremity caused by contamination.

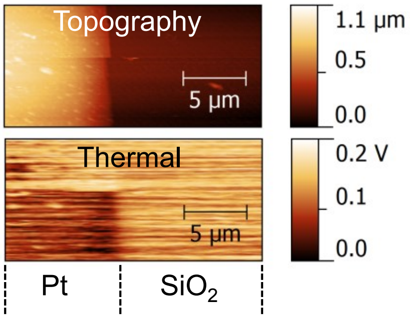

Fig. 6.7. Demonstration of glass-pipette thermoresistive probe using tuning-fork feedback on a Pt/SiO_2 sample. The thermal image was taken in constant current mode showing sensitivity to surface thermal conductivity during the initial scanning and subsequently losing sensitivity during the latter (upper) half.

sample to test the sensitivity of the probes. In these measurements, the tip is placed in the Wheatstone bridge configuration while a constant current is applied to the bridge. The measured thermal signal corresponds to the resulting voltage bias across the bridge (Fig. 4.6) as the tip is scanned on the sample surface. In this case, the sample was scanned from bottom to top. The result is a clear contrast between the two zones in the bottom half. As was seen in Fig. 6.6, the contrast is suddenly lost making the two zones indistinguishable.

Only a few scans were made on the irradiated ZrC sample. As an example, the results in Fig. 6.8, show constant current measurements using a glass-pipette thermoresistive probe. The location is centered on the border between the irradiated and virgin material with the distinguishable line of defects seen in most other images presented in this study, running vertically. Clearly no thermal contrast is observed between the two zones. Thus far, few good thermal images have been obtained from the system due to working on characterizing the overall behavior of the Nanonics system and due to a shortage of thermal probes. Initial testing indicates that the tuning-fork feedback mechanism used by the Nanonics system seems to decrease overall tip-sample conductance due to the gap between the tip and sample surface.

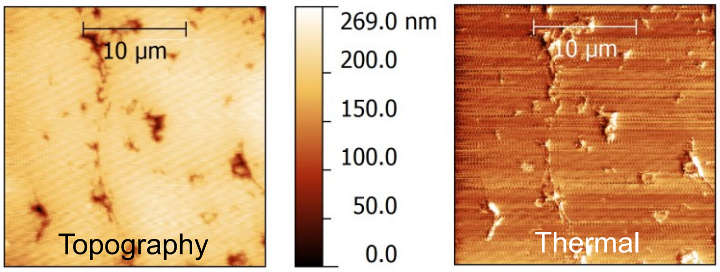

Fig. 6.8. Topography and thermal images in constant current mode on irradiated ZrC from a glass-pipette thermoresistive probe using tuning form feedback. The thermal image shows no contrast between the damaged (left) and undamaged (right) zones.

6.1.3.3. Thin-Film Probe Measurements

The first probe experimented with the irradiated ZrC sample was the thin-film probe in contact mode. This probe type has the smallest contact radius of all the probes tested in this work with an estimated contact radius of ~20 µm. The study performed with this probe focused on obtaining a calibration of the probe signal on several reference materials using DC and AC measurements. While several measurements were made on the irradiated ZrC sample, no thermal conductivity profile related to proton degradation was detected. At that stage, the damage layer thickness was unknown and estimated to be <40 µm (from numerical prediction from TRIM). Therefore, in retrospect, the transition zone of damaged-to-undamaged material was not explored with enough care. An example of a 3ω thermal image is presented in Fig. 6.9. The configuration of the measurement is shown in Fig. 4.6. The thermal image corresponds to the measured amplitude of the third harmonic of the heating frequency, which was set as 169 Hz. The lock-in amplifier used a 3 ms time constant and the AFM was scanned at a rate of 0.18 Hz. The location of the shown image is closest to the transition region. Different than other images presented in this work, the right side of the image is the proton-damaged zone. No noticeable difference is shown in the image to distinguish the two zones.

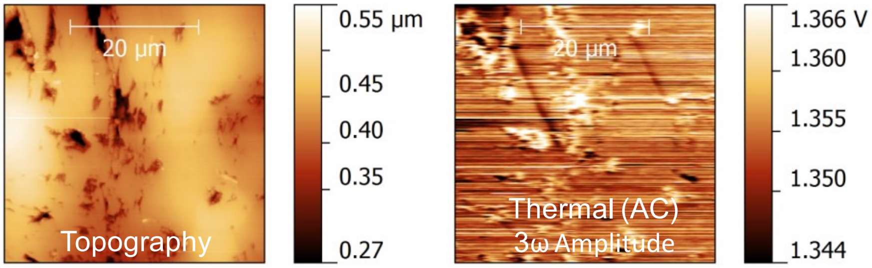

Fig. 6.9. Topography and 3ω amplitude (AC) thermal image of irradiated ZrC measured with a 1ω probe current frequency of 169 Hz. No observable transition between damaged and undamaged zones is observed.

A DC constant temperature result is presented in Fig. 6.10. Unknown at the time, these measurements are far from the boundary of transition (~50 µm depth) from damaged to undamaged ZrC. The maximum x-y range of the Park Systems AFM is 40 µm. No interesting thermal conductivity profile is observed.

6.1.3.4. Summary

The foregoing sections presented a sample of many results obtained in the process of using SThM to extract the in-depth thermal conductivity profile in irradiated ZrC. These results demonstrate that obtaining such a measurement is not trivial and is dependent on many factors that require patience, care, and can be helped by a "good" probe. In all, many measurements were performed on a variety of samples with a variety of probes to explore individual probe

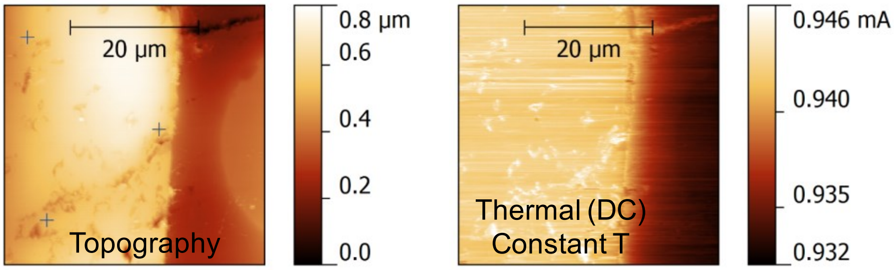

Fig. 6.10. Topography and constant temperature thermal images of irradiated ZrC. Location of measurement is in the irradiation-damaged region near the edge corresponding to the irradiated surface. Damaged-layer transition occurs ~50 µm to the left (out of view). Dark region in both images corresponds to epoxy mount.

sensitivities. At times the inconsistency of a given probe can prove frustrating as calibration is obtained through tedious measurements on many reference samples. Frequently such calibrations were lost for no apparent reason – only the probe no longer demonstrated the same sensitivity or it completely lost sensitivity to thermal properties of the sample. Other times the probe was noticeably damaged and useless for further measurements.

6.2. Spatial-Scanning PTR and Lock-in IR Thermography

Using the PTR system, spatial profiles on the sample surface were made by focusing the laser heating spot diameter to ~50 μm. The normalized amplitude profile measured across the entire thickness of ZrC cross section is displayed in Fig. 6.11. The profile is normalized to the average value of the amplitude in the non-irradiated zone of the sample, and represents the average of three spatial scans with a heating modulation frequency of 1 MHz. The step size between each measurement was 10 μm. At this frequency μ ~ 1-2 μm, meaning thermally thick sample heating case so that the amplitude is inversely $\propto e$ (Eq. (3.10) and (7.8)), assuming the irradiated and non-irradiated zones have similar radiation properties. Although the diffusion

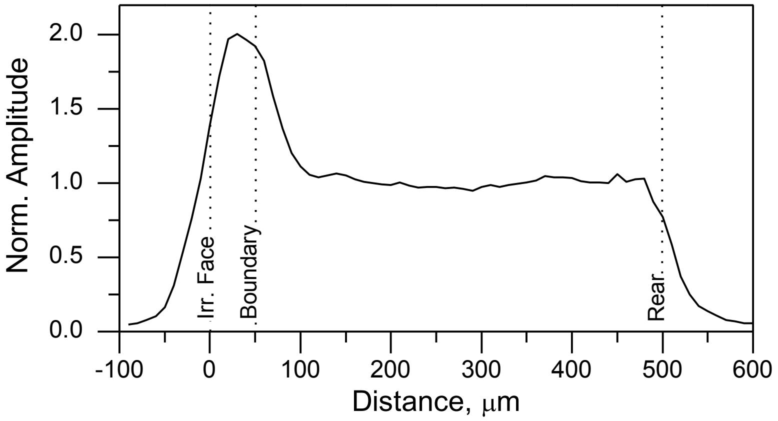

Fig. 6.11. Spatially-scanned profiles of irradiated-ZrC cross-section from PTR amplitude measurements at 1 MHz heating with 50 μm focused spot. Vertical line "Boundary" marks SThM measured thickness of irradiated layer.

length is small in this case, the limitation of lateral resolution was found to be the spot size, which was measured to be ~50 μm (at $1/e^2$) using a DataRay WinCamD profilometer.

In the measured profile, the edges of the sample and the boundary between irradiated and non-irradiated zones evidence the insufficient resolution by gradual changes of signal representing a convolution of the laser spot across the two zones. The peak in the measured profile again shows the damaged layer, a zone of lower e, ($e_{irr}<e_{ZrC}$). The width of the zone is wholly consistent with the measured width found in the SThM profile taking into consideration the heating spot size.

The third direct measurement of the thermal conductivity profile was performed using lock-in IRT. Three heating frequencies were used to image the ZrC cross-section surface: 1Hz ~ μ = 1.25 mm, 10Hz ~ μ = 0.395 mm, 40 Hz ~ μ = 0.198 mm. The calculated amplitudes of the heating response are displayed in Fig. 6.12. The images display several features of the sample. At lower frequency, high signal level is seen on the top and bottom surfaces corresponding to the IR emission from these surfaces. As the sample is embedded in epoxy, which is transparent to IR wavelengths, the emission from these surfaces is strongly manifest, especially at very low frequency (long μ) where much of the surface within the epoxy is heated. At the highest

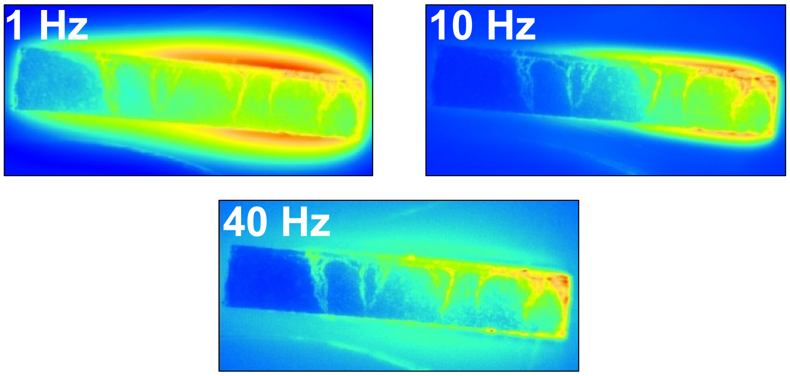

Fig. 6.12. Lock-in IR thermography amplitude images of the cross-section of proton-irradiated ZrC at various frequencies. The proton-damaged, upper layer is evident in each of the images with the strongest contrast between the irradiated and non-irradiated zones in the image at 40 Hz.

frequency, the sample is most distinguishable from these effects. Looking at the sample itself, defect structures provide a stronger signal showing what have the appearance of cracks running through the material.

From these amplitude images, several profiles were extracted in order to map out a spatial profile of the amplitude. Profiles were extracted in regions having less effect from any apparent defect structures. From each image, four representative profiles were extracted and are shown in Fig. 6.13 in terms of absolute signal level. With knowledge of the overall thickness of

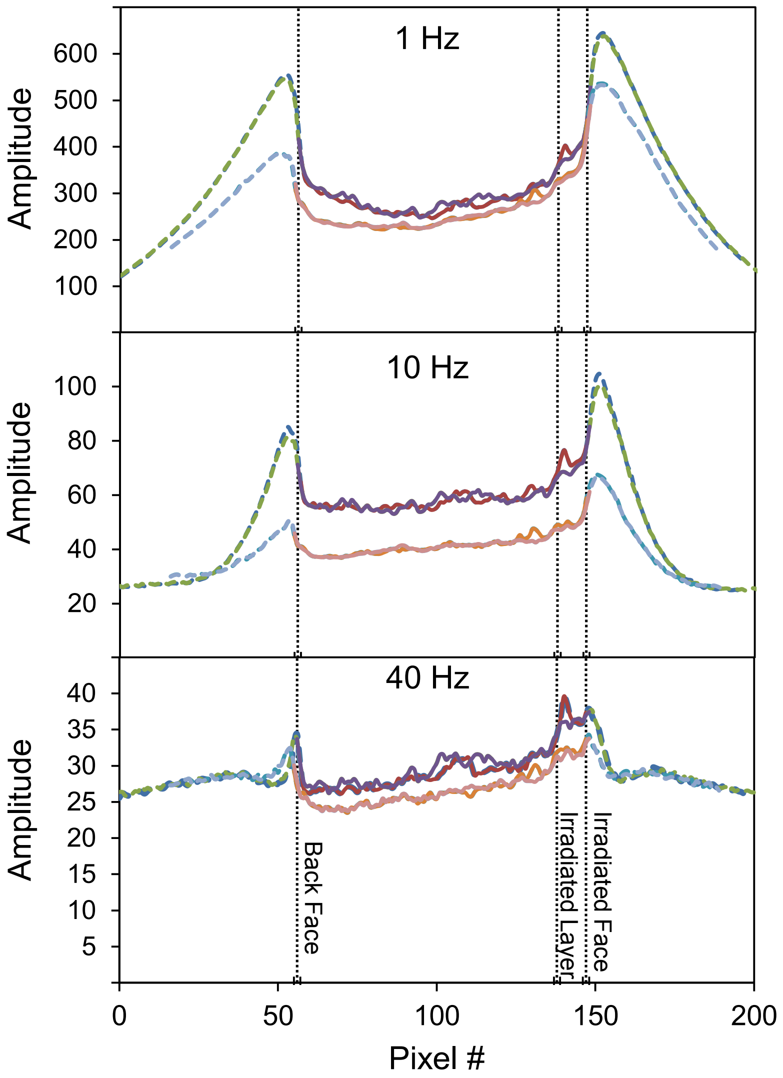

Fig. 6.13. Extracted amplitude profiles from lock-in IR thermography images showing relative values and a comparison of measurements at various frequencies.

the ZrC sample and careful comparison of the various images, various boundaries of the sample are marked in the figure.

As expected due to shortest μ, the higher frequency result shows the greatest sharpness in profile characteristics and was selected to be used as a comparison to the other profiling techniques. The four profiles shown in Fig. 6.13 were used to generate the average profile given in Fig. 6.14, where the linear bias has been subtracted out. The amplitude image of the ZrC sample from which the profiles were extracted, is shown in the inset of the figure. Again, the resulting average of four profiles has been normalized to the level of the virgin ZrC. For this measurement, the heating frequency was limited to 40 Hz, giving μ of the order of L_s. For this reason the spatial resolution of the thermal signal is not as good as the pixel resolution of the camera, which was found to be approximately 5 μm. Also for the same reason, any quantitative interpretation is more difficult to extract from the measurement. The normalized amplitude peak of ~1.2, much less than the PTR result, is expected due to the increased heat spreading due to the large thermal diffusion length, whereas the PTR measurement is confined to a depth of ~1-2 μm

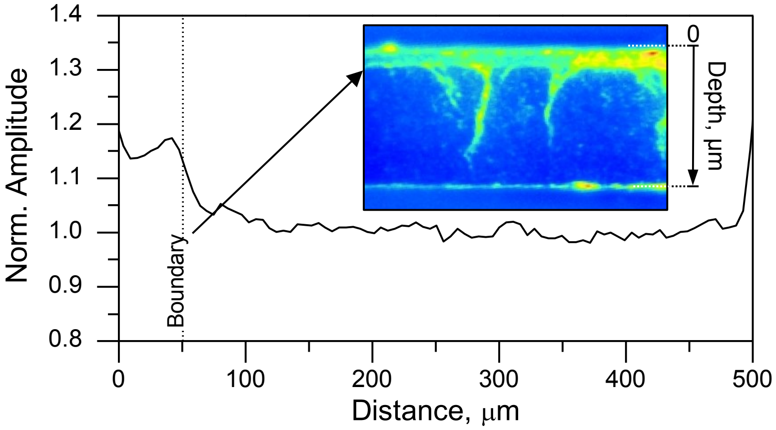

Fig. 6.14. Spatial profiles of irradiated-ZrC cross-section. Vertical line “Boundary” marks SThM measured thickness of irradiated layer. Average of four lock-in IRT profiles at 40Hz heating of entire cross section, taken from amplitude image (inset – amplitude image showing sample cross section).

from the surface. Still, the damaged layer is clearly present with an apparent thickness of the order of ~50 μm.

A direct comparison of the three different spatial profiles along with the numerically calculated profile is found in Fig. 6.15. In this figure, edge effects were removed in the lock-in IRT profiles by subtracting the mirror-inverted, non-irradiated edge from the irradiated edge profile. The SThM profile is represented by an average of the upper levels of the various profiles,

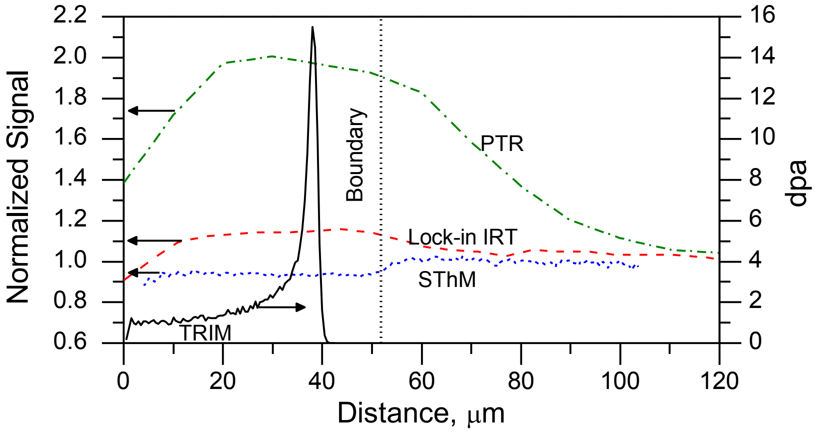

Fig. 6.15. Spatial profiles of irradiated-ZrC cross-section. Vertical line "Boundary" marks SThM measured thickness of irradiated layer. Comparison of measurements from spatial scanning techniques (edge effects removed in lock-in IRT) and numerical prediction of damaged layer.

Table 6.1. Characteristics of thermal conductivity profiling methods used on proton-irradiated ZrC and measured degradation of thermal conductivity.

Method	*Scanning Type*	*Lateral Resolution*	*Probing Depth*
SThM	Spatial	~ contact radius (~ 1 μm)	~contact radius (~1 μm)
Lock-in IR Thermography	Spatial	pixel size = 5 μm μ ~ 300 μm	μ ~ 300 μm
PTR	Spatial	heating spot size ~50 μm	$\mu \approx$ 1-2 μm
PTR	Frequency	measured spot size ~1 mm	$\mu \approx$ 1 mm - 1 μm

considered to be the thermal conductivity profile of the sample. Table 6.1 summarizes the characteristics of each technique's measured profile.

The SThM measurement has the best lateral resolution of the three methods and is, therefore, the most accurate for predicting the irradiation-induced damaged depth (used in Fig. 6.15). For the PTR and lock-in IRT, each has both a strength and a weakness concerning spatial resolution of the measurement that is each other's opposite. The PTR can operate at high frequencies (at the cost of reduced amplitude, $A \propto f^{-1/2}$) allowing for small μ, but the heating spot size used in this measurement is large relative to the needed resolution for measuring L_{irr}. Lock-in IRT has good spatial resolution, but frame rate limits the possibility of decreasing μ. For decreasing heating spot size, PTR resolution will have the inherit limitation from the IR wavelengths involved in detection (8-12μm) as well as the conflict of diminishing IR signal vs. excessive sample heating.

6.3. Thickness of Thermally Affected Layer

To obtain a more precise estimation of the thickness of the thermally affected zone, a scan was made using SThM to include the transition from the epoxy to the sample. The resulting topographic and thermal images as well as line profiles (both topographic and thermal from the same locations) from these images are shown in Fig. 6.16. Due to the V-shape of the Wollaston probe tip, the contact surface is elliptical. Therefore, the spatial resolution in the direction perpendicular to the "V"-plane of the Wollaston tip is better than in the other. The tip orientation for these figures was such to provide the best resolution in the profile. All line profiles in Fig. 6.16(c) have been shifted negatively so that the sample edge indicated by the topographic image is at 0 μm. The transition zone from damaged to undamaged material is marked in the figure and occurs between 50-54 μm from the irradiated surface. This result was found consistent at different locations along the sample confirming a damaged layer of very uniform thickness.

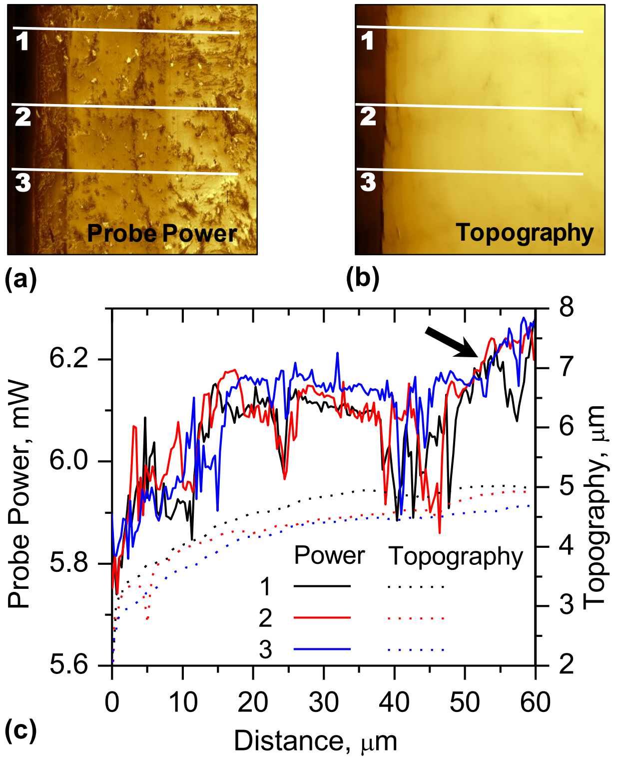

Fig. 6.16. Figures used for damaged depth measurement. (a) and (b) Probe power and topographic images (100 µm × 100 µm) and (c) corresponding, extracted profiles used to measure precise thickness of irradiation damaged layer of ZrC sample. The arrow indicates the transition zone marking the limit of ion penetration at a depth of 50-55 µm.

An optical microscope was used to verify the measured thickness. A photograph of the damaged layer is shown in Fig. 6.17, the boundary of which is roughly marked by an apparent higher concentration of defects. This boundary is confirmed to approximately 50 µm from the edge of the sample.

In comparing these results to those calculated by TRIM in Fig. 4.1(a), the obtained thermal profiles are very consistent with the numerical results. The numerical profile shows very uniform damage spanning most of the affected zone (> 30 µm) in agreement with the measured *k* profile and characteristic of proton-irradiation damage [5]. The zone affected by irradiation is ≈25% deeper than estimated from TRIM, but the discrepancy is reasonable due to uncertainty in the simulation. These results illustrate the significance of zone thickness identification when

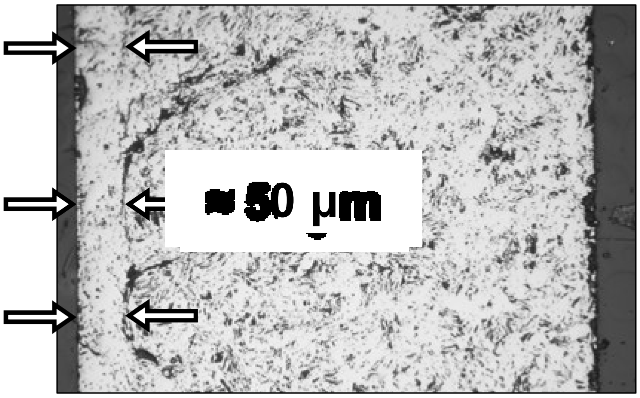

Fig. 6.17. Optical micrograph confirming damaged layer thickness of ≈50 μm.

using non-destructive techniques such as photothermal methods that rely on layer thicknesses as input parameters for thermal property determination. They also show that the assumption of homogenous, damaged layers used in photothermal parameter estimation seems appropriate for proton-irradiated materials. Therefore, the results of the profile measurements justify the thermal model used for the tomographic PTR measurements to extract thermal property data.

CHAPTER 7

THERMAL CONDUCTIVITY DEGRADATION RESULTS

In the previous chapter, multiple approaches were taken to characterize the in-depth thermal property profile through the proton-damaged layer of ZrC. Each of these techniques were explored in terms of their ability to distinguish features of a spatial profile. They all have characteristic difficulties related to quantitative interpretation of the measured signal. Still, the precise level of degradation in the thermal profile is a requisite objective to identify the level of proton-irradiation-induced degradation of thermal transport. In this chapter, the thermal conductivity profile measured in Chapter 6 is to be quantified. First, the measurements from spatial-scanning techniques of Chapter 6 are quantified; then frequency-domain PTR is used to provide a more reliable estimation of thermal conductivity in the damaged zone. These results have been published in [130, 131].

Quantitative interpretations of the signals measured from the spatial profiling techniques are first presented for the spatial-scanning methods which are used as validation of the frequency-scanned FD-PTR results presented in the second section of this chapter. As discussed in Chapter 6, each of the spatial measurements was performed on the polished cross-section of the irradiated ZrC sample. The results presented in this chapter demonstrate the ability of each technique to extract quantitative data. Using a model from literature, the Wollaston-wire probe signal is calibrated with several materials used as references of thermal conductivity. Some discussion of calibration uncertainty follows as is related to the measurements on ZrC. For the IR techniques, the measured signal amplitude is used to extract quantitative information. The uncertainty of this procedure arises due to the fact that the measured amplitude is dependent on surface radiation properties. The results obtained from these measurements are presented in terms of a ratio of thermal conductivities between the damaged/undamaged zones.

The second part of this chapter presents results for tomographic (frequency-scanned) PTR measurements. To ensure unique fitting results for the damaged layer of ZrC, an undamaged ZrC sample was first measured using frequency-scanned FD-PTR to obtain thermal parameters for the virgin material. The FD-PTR measurements were then made on the irradiated face of the ZrC sample. Using the thermal profile obtained in Chapter 6 to identify the layered geometry, a full thermal model is described for the case of periodic heating. The model is used to illuminate limiting heating frequency regimes providing specific parameter sensitivities. Additionally, a sensitivity study is performed to ensure uniqueness of fitted parameters. Using the FD-PTR measurement results, the thermal properties of the irradiated layer were fit from the complete thermal model.

The final section of the chapter draws conclusions regarding the measured thermal degradation in relation to previous works and to the measured irradiation-damage level for similar samples [78]. A brief description of the influence of the particle-irradiation effects on energy carriers is provide. Finally, a discussion regarding the assumption of a thermal resistance at the damaged/undamaged interface is also provided.

7.1. Spatial-Scanning Measurement Quantification

The methods used to spatially profile the ZrC cross section were selected due to their high spatial resolution. Each has their own particular set of weaknesses and strengths. Quantitative measurement is a weakness for each of these techniques. For SThM, quantitative interpretation of measured signals remains a great challenge for the technique even after over two decades of research in the area (Section 4.2.3). In this section, the results from the Wollaston wire probe given in Chapter 6 are used to quantify thermal conductivity changes in the irradiated ZrC. The IR techniques rely on amplitude data, which is generally disadvantageous when using such techniques due to the dependency on material surface characteristics such as emissivity. This section presents the quantitative results of each of the aforementioned spatial profiling approaches. Although uncertainties in each measurement are difficult to quantify, the strength of approach presented is the complementary comparisons that result from multiple approaches, which provide better confidence of measurement accuracy.

7.1.1. Thermal Conductivity Estimation from SThM Signal

The measured thermal power from SThM measurement is the combination of heat loss into the sample through the tip-sample thermal conductance, as well as all other heat losses from the exposed wire (heating) tip. Because every tip has unique physical characteristics (shape, contact surface, etc), each tip should be calibrated (basically a calibration of contact area) using samples of known k. Clearly, from SThM results presented in the Chapter 6, a step-like profile of thermal conductivity exists between the irradiated and non-irradiated zones. Therefore, the purpose of this section is to provide an estimation of the relative change of k that this step represents.

Compared with results from other tested probes, the results from the Wollaston wire probe proved to be the most stable in terms of providing clear contrast between the irradiated/non-irradiated zones of the ZrC. In an effort to quantify the k degradation in the damaged layer, the measured thermal signal is compared to modeling and calibration work reported in the literature. Lefevre et al. [124] proposed a DC model of one side of the exposed, symmetric, V-shaped tip of the Wollaston probe using a steady-state 1D fin equation. To simplify the problem, they neglect the heat contributions from losses to air and variations of the Joule heating caused by temperature resistance changes in the platinum/rhodium wire of the probe (estimated to be ~10-20% of the total). The resulting formula relates the sample conductance to the difference, ΔP, of dissipated tip Joule power between sample contact, P_c, and in air, P_a, normalized to dissipated power with sample contact,

$$\Delta P / P_c = \left(P_c - P_a\right) / P_c \cong 0.75 \cdot G \cdot 2\pi \cdot b \cdot k_s \cdot (2G \cdot G_{Pt} + (2G_{Pt} + G) 2\pi \cdot b \cdot k_s)^{-1}. \tag{7.1}$$

G is tip-sample thermal conductance (assumed constant in [124]); $G_{\mathrm{Pt}} = k_{\mathrm{Pt}} \cdot S/L$ is the thermal conductance of one leg of the platinum/rhodium wire tip; k_{s} is the contact surface thermal conductivity; and b is the thermal exchange radius. The quantity $2\pi \cdot b \cdot k_{\mathrm{s}}$ is the thermal constriction conductance assuming a constant temperature hemisphere of radius b at the probe contact. Equation (7.2) was also used by David et al., with the following adaptation made for the variation of tip-sample conductance with sample thermal conductivity, k_{s} [132],

$$G = G_g + 2\pi \cdot a_c \cdot k_{Pt} \cdot k_s \cdot (k_{Pt} + k_s)^{-1}. \tag{7.2}$$

G_{g} is the tip-sample thermal conductance through a surrounding gas; a_{c} is the tip-sample physical contact radius.

Because of the large uncertainty involved with quantitative interpretation of SThM measurements, a calibration was made using several materials listed in Table 7.1, to obtain the approximate *relative* change of thermal conductivity of the irradiated ZrC.

Table 7.1. Reference materials used to obtain SThM calibration curve.

Material	*k* $\mathrm{W \cdot m^{-1} \cdot K^{-1}}$	*Material*	*k* $\mathrm{W \cdot m^{-1} \cdot K^{-1}}$
Glass	1.05	Ti	21.9
Quartz	1.4	Sapphire	25
ZrO2	1.7	Ta	57.5
Pyrolytic Carbon I	4	Ni	90
TiAlV	6.4	SiC	160
Pyrolytic Carbon II	10	Diamond	900+

The results of the calibration are shown in Fig. 7.1 with the best fit of Eq. (7.1) using G_{Pt} = 5.9 W·K^{-1} [124]. Resulting best fit parameters in Eq. (7.1) and Eq. (7.2) are G_g = 4.5 W·K^{-1}, a_c = 8 nm, and b = 1.1 µm. Due to the uncertainties related to these parameters, the primary use of the fit is to provide a calibrated trend from which the relative change of k for the ZrC sample may be extracted. From the calibration curve, the found k value of the bulk ZrC is ≈30 W·m^{-1}K^{-1} and that representative of the damaged layer is ≈ 10 W·m^{-1}K^{-1}. The resulting degradation of k induced by the proton damage is then ≈ 66%.

Regarding the uncertainty of these estimations, the calibration curve clearly reveals the difficulty of such quantitative interpretation, especially with materials of high k where the sensitivity to k becomes diminishingly small. However, particular care was taken on several of the calibration sample measurements to ensure more identical conditions between different materials. For example, for glass (low k), diamond (high k), and both ZrC materials, measurements were performed after scanning to select random locations of extremely flat, smooth, and homogeneous regions (free of defects). For a minimum of 10 samples points, the

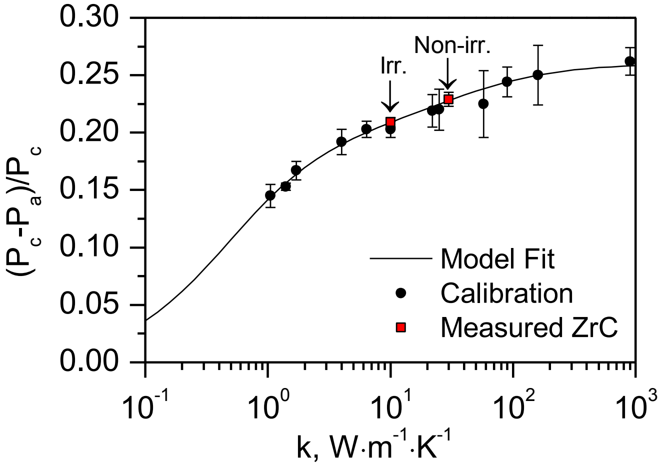

Fig. 7.1. SThM calibration curve made using Lefevre's model [119], Eq. (7.1), with the measured irradiated and non-irradiated ZrC. Error bars represent measurement precision at ± 2·St.Dev.

resulting relative standard deviations (σ_i) were: 3.45% for glass, 2.3% for diamond, 1% for irradiated ZrC, and 1.3% for non-irradiated ZrC.

Without doing a detailed uncertainty analysis of the entire measurement, the uncertainty of the found k value related to the sensitivity of Eq. (7.1) to k is equal to the standard deviation of the measurement multiplied by the inverse of the slope of the calibration curve evaluated at the found k, $(2 \cdot \sigma_{\Delta P/P_c} \cdot k) \cdot (\partial k_s / \partial(\Delta P/P_c))$, (factor of 2 is for 95% confidence). The resulting uncertainty is 30 ± 10 $\mathrm{W \cdot m^{-1} \cdot K^{-1}}$ and 10 ± 2.4 $\mathrm{W \cdot m^{-1} \cdot K^{-1}}$ for non-irradiated and irradiated ZrC, respectively. Because the relative change of the irradiation damaged material is of particular interest, the low deviations between materials and the good agreement of the measurements on the virgin ZrC material with values from literature, greater confidence is taken for the estimation of relative degradation of thermal conductivity in the proton-irradiated ZrC.

7.1.2. Spatial-Scanning IR Techniques

The thermal profile results in Chapter 6 were presented as a demonstration of relative thermal property variation in the ZrC cross section. In the limit of a thermally thick sample for thermal wave methods, the measured amplitude is $\propto e^{-1}$. Therefore, the normalized profile should also represent the ratio of the local thermal effusivity of the sample to the effusivity of the bulk, virgin ZrC, e_{ZrC}.

In the case of the PTR profiles, the heating frequency was 1 MHz or μ = 1-2 μm, corresponding to a thermally thick case. In the damaged layer, a normalized peak of 2 in Fig. 6.11 represents the ratio $e_{\mathrm{irr}}/e_{\mathrm{ZrC}}$. Assuming the same volumetric heat capacity (discussed in Section 7.2.3.2), this means that the conductivity ratio of the $k_{\mathrm{ZrC}}/k_{\mathrm{irr}}$ is ~ 4.

For the lock-in IRT results, the maximum heating frequency was 40 Hz or μ = 0.198 mm. The thermal diffusion length is on the order of the sample cross-section thickness and greater than the irradiated zone thickness and thus not at a high frequency limit. For this reason, quantitative interpretation is more difficult to extract from the measurement. The normalized amplitude peak of ~1.2, much less than the PTR result, is expected due to the increased heat spreading due to the large thermal diffusion length, whereas the PTR measurement is confined to a depth of ~1-2 μm from the surface. Assuming amplitude is $\propto e^{-1}$, results in a ratio of conductivities of $k_{\mathrm{ZrC}}/k_{\mathrm{irr}} \sim 1.5$.

In regards to the extraction of quantitative information, none of the spatial profiling methods used, provide a reliable extraction of k independently. The value extracted for k_{ZrC} is at the upper limit of typical SThM sensitivity, and thus, uncertainty becomes increasingly large for this range. For the PTR spatial scans, ratio of effusivities was extracted although again with large uncertainty, primarily related to the variations of thermal radiation properties (optical reflectivity and IR emissivity) across the sample surface. Still, the high emissivity (~0.9) [133] of ZrC is favorable for such analysis especially comparing between two zones of the "same" material. The results extracted from SThM and PTR are comparable and especially interesting when viewed from the perspective of measurement probing depth in the two measurements. For the PTR at 1MHz heat modulation and the SThM, the probing depths are both on the order of a few microns. Therefore, the effects of the (larger) grain boundaries in the material are not measured. As was previously described, the irradiated zone shows no evidence of grain boundaries while the virgin ZrC is characterized by grain of ~25 μm size. The virgin material would be expected to have a higher measured thermal conductivity (excluding longer scale effects due to boundary thermal resistance). Assuming $k_{\mathrm{irr}} \sim 10\ \mathrm{W\cdot m^{-1}\cdot K^{-1}}$, a value of $k_{\mathrm{ZrC}}/k_{\mathrm{irr}} = 4$ is not unreasonable for this measurement.

7.2. Tomographic PTR Measurements

This section presents the frequency-scanned PTR results measured directly (and non-destructively) on the irradiated face of the ZrC sample as shown in Fig. 7.2. The presentation is divided into three main sections. First, a thermal model is presented stemming from the cross-

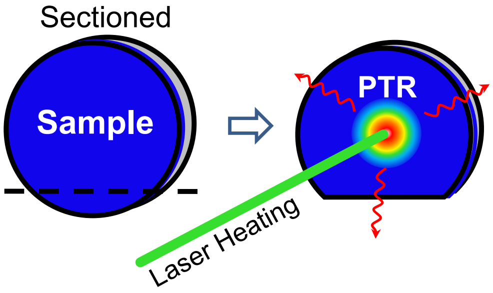

Fig. 7.2. Sample configuration for tomographic (frequency-scanned) PTR measurements

section profiling results. A complete theoretical description of the model is presented along with important limiting cases. Next, a sensitivity study is used to estimate the frequency sensitivity of important parameters and ensure unique parameter dependencies. Finally, measured amplitude and phase spectra are used to fit desired parameters using the derived thermal model.

7.2.1. Frequency Response of a Two-Layer Sample

As with other works, the continuously varying damage in the irradiated zone (Fig. 4.1) is approximated as a multilayered structure [83, 87, 88]. As compared to other types of ions, proton irradiation lends particularly well to a structure approximated by discrete layers due to the relatively thick and uniform damage level spanning most of the damaged zone in the sample as described in Section 3.2.2. From the measured profile obtained from SThM measurements (Chapter 6), the proton-irradiated ZrC sample is modeled as a homogeneous damaged layer on the bulk, virgin ZrC material as seen in Fig. 7.3. An interfacial thermal resistance, R_{th}, is placed between the two materials to account for the possibility of a greater damaged zone, seen in the numerically calculated damage profile and/or the presence of void space at the interface (discussed in more detail in Section 7.2.3.2). The spatial profiling measurements shown in Chapter 6 showed no evidence of a secondary layer as the calculated damage profile seen in Fig. 4.1(a) may suggest by the sharp damage peak located at the back of the profile. However, even if a thin layer exists, using R_{th} is also mathematically appropriate.

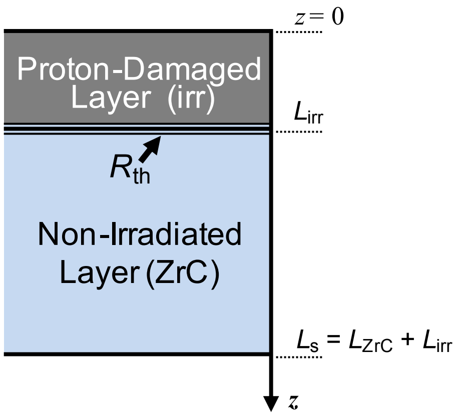

Fig. 7.3. Schematic of heat model geometry used for frequency-scanning FD-PTR for irradiated ZrC sample.

Following the theory developed in Section 3.3.3.1, the thermal quadrupoles method has been used to model the irradiated ZrC sample [39]. The sample is considered adiabatic (heat losses neglected) and opaque to the 532nm laser heat source (absorption calculated from the dielectric constant of $ZrC_{0.96}$ results in a penetration depth of < 50nm). In the simplified case of the ZrC sample under plane illumination (1D), a matrix relationship between the temperature and heat flux at the front and at the rear of the sample may be found as:

$$\begin{pmatrix} T_{irr}(z=0) \\ \varphi_{irr}(z=0) \end{pmatrix} = \begin{pmatrix} A_{irr} & B_{irr} \\ C_{irr} & D_{irr} \end{pmatrix} \cdot \begin{pmatrix} 1 & 1 \\ 1 & R_{th} \end{pmatrix} \cdot \begin{pmatrix} A_{ZrC} & B_{ZrC} \\ C_{ZrC} & D_{ZrC} \end{pmatrix} \cdot \begin{pmatrix} T_{ZrC}(z=L_s) \\ \varphi_{ZrC}(z=L_s) \end{pmatrix} \tag{7.3}$$

where $A_i = D_i = \cosh(\sigma_i L_i)$, Bi = $\sinh(\sigma_i L_i)/(k_i \cdot \sigma_i)$, $C_i = k_i \cdot \sigma_i \cdot \sinh(\sigma_i L_i)$ for layer "i." σ_i is the complex thermal wave vector, $\sigma_i = (i\omega/\alpha_i)^{1/2} = (1+i)/\mu_i$, where $\mu_i = (\alpha_i/\pi f)^{1/2}$ is the thermal diffusion length. The depth sensitivity controlled by μ makes frequency-based thermal-wave techniques powerful for non-destructively probing the in-depth properties of materials. $\alpha_i = k_i/(\rho_i \cdot c_{pi})$ is thermal diffusivity with thermal conductivity, k_i, density, ρ_i, and specific heat capacity, c_{pi} for material "i." The term "$k_i \cdot \sigma_i$" may be simplified to $e_i \cdot (i \cdot \omega)^{1/2}$ where $e_i = (k_i \cdot \rho_i \cdot c_{pi})^{1/2}$ is the thermal effusivity.

Assuming the heat losses at the rear are negligible so that $\varphi_{\mathrm{ZrC}}(z = L_s) = 0$, the thermal impedance of the sample in a front detection configuration (FD-PTR) may be found as

$$Z_{irrZrC} = \frac{T_{irr}(z=0)}{\varphi_{irr}(z=0)} = \frac{A_{irr} \cdot A_{ZrC} + B_{irr} \cdot C_{ZrC} + A_{irr} \cdot C_{ZrC} \cdot R_{th}}{C_{irr} \cdot A_{ZrC} + D_{irr} \cdot C_{ZrC} + C_{irr} \cdot C_{ZrC} \cdot R_{th}}, \tag{7.4}$$

or in an explicit form as

$$\begin{gathered} Z_{irrZrC} = \frac{1-i}{e_{irr}\sqrt{2\omega}} \times \\ \times \frac{1 + (e_{ZrC}/e_{irr})\tanh(\sigma_{irr}L_{irr})\tanh(\sigma_{ZrC}L_{ZrC}) + \sqrt{i\omega}e_{ZrC}R_{th}\tanh(\sigma_{ZrC}L_{ZrC})}{\tanh(\sigma_{irr}L_{irr}) + (e_{ZrC}/e_{irr})\tanh(\sigma_{ZrC}L_{ZrC}) + \sqrt{i\omega}e_{ZrC}R_{th}\tanh(\sigma_{irr}L_{irr})\tanh(\sigma_{ZrC}L_{ZrC})}. \end{gathered} \tag{7.5}$$

At low frequencies the whole sample is thermally thin ($L_{\mathrm{irr}}/\mu_{\mathrm{irr}} << L_{\mathrm{ZrC}}/\mu_{\mathrm{ZrC}} << 1$). The thin irradiated layer can be incorporated in the bulk and in a first approximation Eq. (7.5) yields

$$Z_{ZrC} = -i/\left(\omega\left(L_{irr} + L_{ZrC}\right)\rho_{ZrC}c_{pZrC}\right), \tag{7.6}$$

meaning that the PTR signal amplitude is $\propto f^{-1}$ and the phase is -90°. There is no influence from the parameters of the irradiated layer or from R_{th}. The sample is equivalent to the homogeneous bulk ZrC.

At intermediate frequencies the bulk ZrC is thermally thick ($L_{\mathrm{irr}}/\mu_{\mathrm{irr}} \leq 1 << L_{\mathrm{ZrC}}/\mu_{\mathrm{ZrC}}$). Then $\tanh(\sigma_{ZrC}L_{\mathrm{ZrC}}) \approx 1$ and Eq. (7.5) reduces to

$$Z_{irrZrC} = \frac{1-i}{e_{irr}\sqrt{2\omega}} \frac{1 + (e_{ZrC}/e_{irr})\tanh(\sigma_{irr}L_{irr}) + \sqrt{i\omega}e_{ZrC}R_{th}}{\tanh(\sigma_{irr}L_{irr}) + (e_{ZrC}/e_{irr}) + \sqrt{i\omega}e_{ZrC}R_{th}\tanh(\sigma_{irr}L_{irr})}. \tag{7.7}$$

This frequency range offers the most information on the irradiated layer. Referring to the bulk layer, Eq. (7.7) contains only its effusivity, e_{ZrC}.

At high frequencies both layers become thermally thick ($1 << L_{\mathrm{irr}}/\mu_{\mathrm{irr}} << L_{\mathrm{ZrC}}/\mu_{\mathrm{ZrC}}$) and Eq. (7.7) further simplifies to

$$Z_{irr} = (1-i)/\left(e_{irr} \cdot \sqrt{2\omega}\right), \tag{7.8}$$

meaning that the amplitude is $\propto f^{-1/2}$ and the phase is -45°. The only accessible parameter is e_{irr}, via the amplitude. There is no influence from the bulk layer. Equation (7.8) is applicable for the spatial-scanning PTR on very shallow depths. It allows measuring relative effusivity variations over the sample cross-section.

Depending on boundary conditions, a layer manifests either its capacitive impedance component Z_C (like Eq. (7.6)) under quasi-isothermal conditions, or rather its resistive component $R = L/k$ under temperature gradients between the two faces. In the quadrupole formalism the two components appear in parallel. As long as $Z_C >> R_{th}$, Z_C can be neglected and L can be set to zero. In a multilayer system, such a layer can be replaced by an interfacial thermal resistance R_{th} having the same value as R. Note that the condition for this equivalence depends on frequency. In Section 7.2.3.2 it will be shown that this condition is fulfilled in the present study.

7.2.2. Sensitivity Analysis

From the theoretical model presented above, the dependence of the complex impedance to ω is a function of five independent parameters: $L_{irr}\alpha_{irr}^{-1/2}$, $L_{ZrC}\alpha_{ZrC}^{-1/2}$, e_{irr}, e_{ZrC}, and R_{th}. The parameters related to the virgin material are measured independently so that the independent parameters to be determined are $L_{irr}\alpha_{irr}^{-1/2}$, e_{irr}, and R_{th}. To ensure unique fitting results, the relative sensitivity of the thermal parameters to be fitted has been studied. The relative sensitivity of a function, $F(p)$, to parameter "*p*" is defined as

$$S_p = \frac{\partial F/F}{\partial p/p} = \frac{\partial(\ln F)}{\partial(\ln p)} \tag{7.9}$$

In the case of complex quantities, $F=Amp\cdot\exp(i\psi)$, it can be shown that $S_p=S_{Amp,p}+iS_{\psi,p}$ where $S_{\psi,p} = \partial\psi/\partial(\ln p)$ [61]. A value $S_{A,p} = -1$ implies $F\propto p^{-1}$. The relative sensitivities for A and ψ to the three parameters related to the irradiated layer are plotted in Fig. 7.4. Their sensitivity

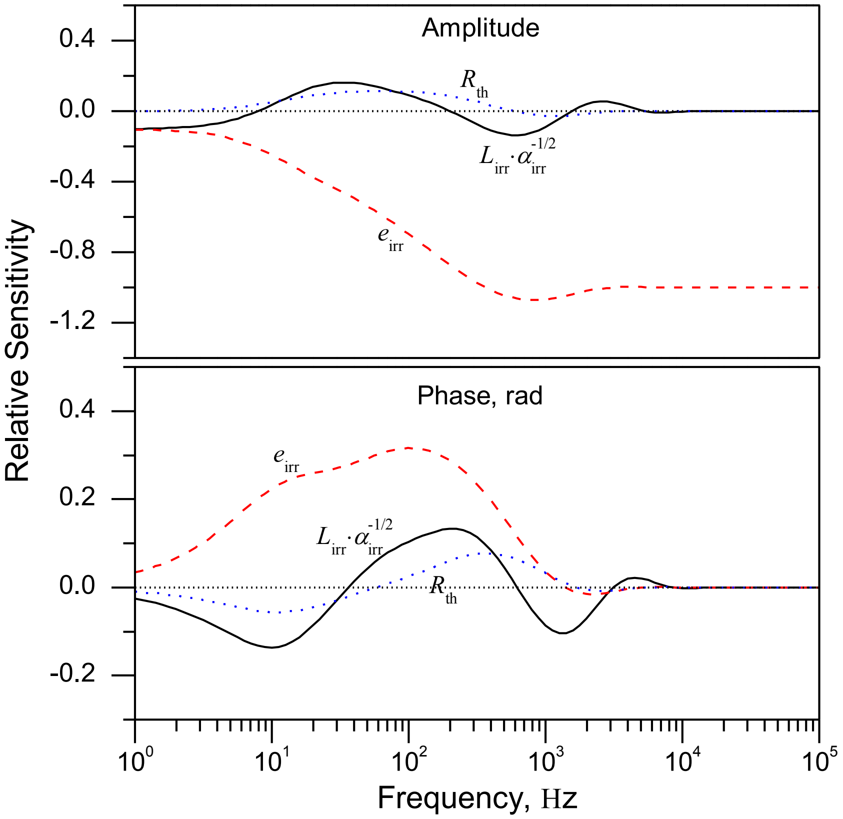

Fig. 7.4. Relative sensitivities of the (top) amplitude and (bottom) phase to independent parameters for proton-irradiated ZrC using the values for parameters shown in Table 7.2.

spectra are different indicating that the respective parameters are not correlated. Therefore, the fit of this parameter set is feasible. Moreover, the features of the spectra are consistent with the discussion of Eqs. (7.6)-(7.8). At low frequency there is practically no sensitivity to the plotted parameters (Eq. (7.6)), while at high frequency there is only amplitude sensitivity to e_{irr} ($S_{Amp,eirr}$ = -1) as predicted by Eq. (7.8). All three parameters reveal strongest sensitivity from 8 Hz to 8 kHz providing the range of frequencies selected for fitting them in the thermal model to the FD-PTR results. This range encompasses the more restrictive interval of 17.5-580 Hz set by the thermally thin-thick limits of the two layers (Fig. 7.5 and Table 7.2). The parameter of interest k_{irr} is embedded in $L_{irr}\alpha_{irr}^{-1/2}$ and in e_{irr}. It will be eventually determined using other complementary data (Section 7.2.3.2).

7.2.3. Frequency-Scanning PTR Results

Equation (7.5) describes the thermal impedance of the ZrC sample, which is proportional to the sample surface temperature measured by the PTR system. The sensitivity analysis showed that the parameters, $L_{irr}\alpha_{irr}^{-1/2}$, e_{irr} and R_{th}, are decorrelated and can be simultaneously fitted. Prior to that, the other two parameters $L_{ZrC}\alpha_{ZrC}^{-1/2}$ and e_{ZrC} were determined from a sample of undamaged ZrC material. Both amplitude and phase data were used for extracting the thermal parameters of interest. However, because the amplitude is dependent on instrumental factors, only relative values were used.

7.2.3.1. Thermal Diffusivity of Virgin ZrC

A non-irradiated sample of ZrC with known thickness L_{s}' was used to measure its thermal diffusivity from frequency-scanning FD-PTR. The direct transition between Eq. (7.6) and Eq. (7.8) (with e_{ZrC} replacing e_{irr}) occurs at frequency, $f_{T,}$ when $\mu_{ZrC} = L_{\mathrm{s}}'$, whence $L_s'\alpha_{ZrC}^{-1/2} = (\pi f_T)^{-1/2}$. The PTR obtained spectrum and the f_T marker are similar to that obtained for the irradiated ZrC below ~100 Hz. Next the measured value of ρ and the literature value of c_{p} (Section 4.1.2) were used to extract k_{ZrC}. The result is a bulk value of $k_{\mathrm{ZrC}} = 26.7\pm1$ $\mathrm{W\cdot m^{-1}\cdot K^{-1}}$ (Table 7.2). For comparison, thermal conductivity of ZrC reported in the literature varies from 17 to 40 $\mathrm{W\cdot m^{-1}\cdot K^{-1}}$ with [80, 134-137] higher stoichiometry resulting in the higher values. Finally, e_{ZrC} could also be determined. Using electrical resistivity values of 65-75 $\mu\Omega\cdot$cm from the literature for similar stoichiometry (~1) and hot-pressed ZrC [80, 134], the Wiedemann-Franz Law (Eq. (3.3)) predicts an electronic contribution to k of ~ 9-11$\mathrm{W\cdot m^{-1}\cdot K^{-1}}$.

7.2.3.2. k_{irr} & R_{th}

Frequency scanning FD-PTR measurements were made on the irradiated face of the ZrC sample. Multiple measurement spectra were obtained over the span of a few months finding very consistent results. Amplitude (*Amp*) and phase (ψ) results measured on the irradiated face of the ZrC sample along with the model results (Eq. (7.5)) are presented in Fig. 7.5. A summary of key parameter values are found in Table 7.2. For visual purposes, the amplitude data is plotted as $Amp{\cdot}f^{1/2}$. This subtracts the overall amplitude slope of $f^{-1/2}$ found in the pre-factor of Eq. (7.5). At low frequencies, the results are characteristic of a thermally thin sample ($\mu > L_s$) where *Amp*

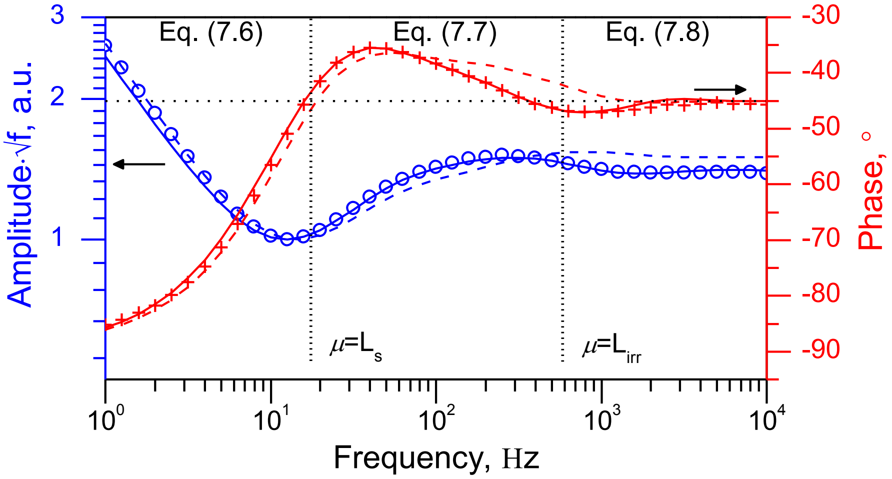

Fig. 7.5. FD-PTR amplitude and phase for proton-irradiated ZrC. Points, experiment; solid lines, fit with Eq. (7.5) and $L_{irr}\alpha_{irr}^{-1/2}$, e_{irr} and R_{th} as free parameters; dashed lines, Eq. (7.5) with $R_{th} = 0$. Key parameter values are listed in Table 7.2. The thermally thin-thick vertical markers (f_T given in Table 7.2) delimit three frequency sub-ranges and the respective theoretical special cases.

Table 7.2. Key sample parameters derived from independent fit parameters ($L_{irr}\alpha_{irr}^{-1/2}$, e_{irr} and R_{th}) and from additional measurements: (m) denotes previously measured, (SThM) denotes SThM measurement, (PTR) denotes FD-PTR measurement. Transition frequencies f_T for thermally thin-thick ($\mu = L$) irradiated and bulk layers are also given.

Layer	f_T, Hz	L, μm	k, W·m^{-1}·K^{-1}	$\rho c_p\cdot10^{-6}$, J·m^{-3}·K^{-1}	$R_{th}\cdot10^{6}$, m^2·K·W^{-1}
Bulk ZrC	17.1	453±2 (SThM & m)	26.7±1 (m)	2.42 (lit) [80,85]	1.58±0.1 (PTR)
Irr. ZrC	579	52±2 (SThM)	11.9±0.5 (PTR)	2.42±0.1 (PTR)	

demonstrates f^{-1} dependence and ψ approaches –90° (cf. Eq. (7.6)). For high frequencies ($\mu < L_s$), $Amp{\cdot}f^{1/2}$ is flat while $\psi \rightarrow -45°$ (cf. Eq. (7.8)). The dashed lines are plots of Eq. (7.5) for $R_{th} = 0$. The differences relative to the full model are relatively small in the mid-frequency range, and vanish outside this range. This behavior is consistent with the low sensitivity spectra to R_{th} from Fig. 7.4.

The simultaneous fit of the independent parameters: $L_{irr}\alpha_{irr}^{-1/2}$, e_{irr}, and R_{th} to Amp and ψ with Eq. (7.5)) provides the results shown in Table 7.2. Using the measured values of L_{irr}, from α_{irr} and e_{irr}, results in $k_{irr} = 11.9\pm0.5$ W·m^{-1}·K^{-1} and $(\rho{\cdot}c_p)_{irr} = (2.42\pm0.1){\cdot}10^6$ J·m^{-3}·K^{-1}. The fit value of interfacial resistance is $R_{th} = (1.58\pm0.1){\cdot}10^{-6}$ m^2·K·W^{-1}. k_{irr} is dependent on L_{irr} of the sample due to the parameter dependency of the model. The resulting value of $(\rho{\cdot}c_p)_{irr}$ is nearly identical to the value of the non-irradiated material. Irradiation effect on heat capacitance is not expected to be great and for a similar material, SiC, was found to be practically non-existent for neutron irradiation [138]. As further validation, image analysis was performed on an optical micrograph of the sample cross section (e.g. Fig. 7.6). Comparing the number of pixels related to defect areas (appear porous) between the two zones, indicates a 5% possible density change (decrease). This result validates the fit procedure. The irradiation-induced degradation of k is then ~55%.

7.3. Particle-Radiation-Induced Degradation of Thermal Conductivity

From the SThM signal calibration, k_{irr} was found to be 10 ± 2.4 W·m^{-1}·K^{-1} while the k_{ZrC} was 30 ± 10 W·m^{-1}·K^{-1}, comparing favorably with the PTR measurements of $k_{irr} = 11.9 \pm0.5$ W·m^{-1}·K^{-1} and $k_{ZrC} = 26.7\pm1$ W·m^{-1}·K^{-1}. The result for the bulk ZrC is in the higher range of most values reported in the literature (17-40 W·m^{-1}K^{-1} from [80, 134, 135, 137, 139]) but is consistent with high carbon content in the ZrC sample (C/Zr = 1.01). The significant degradation level of k was similar to that reported by David et al. [83] (stoichiometry not specified) and greater than that reported by Snead et al. [79] (C/Zr = 0.87, irradiated at higher temperatures). The SThM-measured k_{ZrC} showed relatively more variability that was attributed to both decreased sensitivity and the localized measurement, not capturing longer scale effects such as grain boundaries (grain size ≈ 24 μm). However in the irradiated zone the dominant mechanism of thermal transport degradation is a high concentration of nanometer-sized Frank loops that would be manifest in both SThM and PTR. Grain boundaries were not found in the irradiated zone of the ZrC sample [78].

Clarke [140] developed a model to estimate the minimum k for a material in an amorphous state at high temperatures. The model only accounts for acoustic phonon modes and is formulated based on expressions for minimum phonon mean free path and mean phonon velocities. The mean free path is formulated from the cube root of the volume of a molecule. Using this expression, the minimum calculated thermal conductivity, k_{min}, of ZrC is 1.6 $\mathrm{W{\cdot}m^{-1}{\cdot}K^{-1}}$. Snead et al. found little change of electrical resistivity in ZrC resulting from fast neutron irradiation. The small changes of thermal conductivity were then attributed to phonon scattering from irradiation-induced defects [79]. While no measurements of electrical resistivity were made in this work for comparison, assuming the change of the electronic contribution to k is relatively small as is common in ceramic material [26], the measured k_{irr} compared to the electronic contribution calculated in Section 7.2.3.1 evidences a drastic reduction of the phonon contribution of k, to the order of k_{min}.

From R_{th} and an approximate thickness for the secondary layer as 5 μm from the TRIM profile, k for such a layer would be approximately L/R_{th} = 3.2 $\mathrm{W{\cdot}m^{-1}{\cdot}K^{-1}}$, comparable to what others have found for k of regions of peak damage [83, 87]. On the other hand, the capacitive impedance Z_C of the same layer satisfies the condition $Z_C >> R_{\mathrm{th}}$ for frequencies up to 8.3 kHz. The sensitivity of PTR method to R_{th} is situated below this frequency limit and therefore the effect of R_{th} is indistinguishable from that of an equivalent 5 μm thick layer (Section 7.2.2). With the other methods, the spatial profiles made of the irradiation-damaged profile reveal no evidence of a region of peak damage (sharp degradation of *k*). Although in such a configuration, the excitation thermal gradients are oriented primarily parallel to the interface, which is unfavorable for the detection of R_{th}. Yet, from the frequency-based FD-PTR measurements, the shape of the profiles shows the existence of a strong resistance at the rear of the irradiated layer. One theory to explain this resistance is that it may not actually be due to the damaged microstructure as suggested by the TRIM results. Instead, evidence supports the possibility of small voids in the material that have been pushed by the proton irradiation to congregate at the backside of the damaged zone.

An optical micrograph of the sample cross-section is shown in Fig. 7.6; in which, the damaged layer is apparent. In the micrograph, the polished sample has many "defect" structures (void space based on topographic measurements from SThM) that appear as dark regions. The irradiated layer is clearly visible due to less defects and a higher concentration of defects at the rear of the layer. In some regions, "crack"-like structures are visible, running primarily

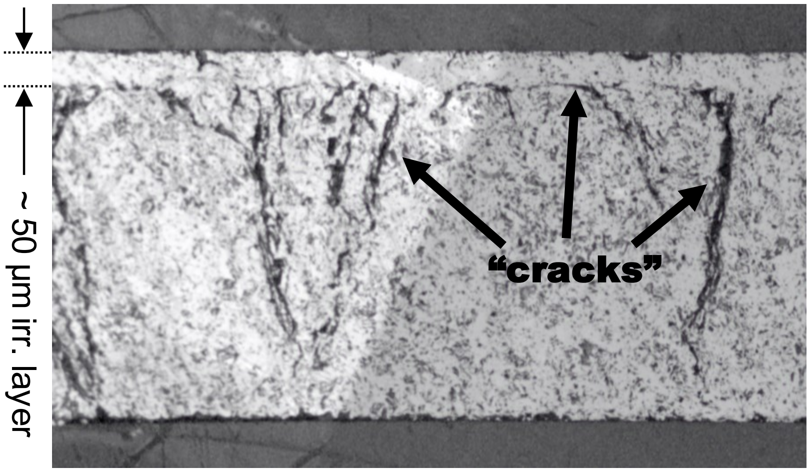

Fig. 7.6. Optical micrograph of irradiated-ZrC cross section. Irradiated layer has ~50µm thickness. "Cracks" are clearly visible, terminating at depth of irradiation penetration. In some locations, showing evidence of having been pushed by proton front to form a boundary between the two zones.

perpendicular to the irradiated surface. All of these “cracks” (appear to be aligned void space, originating from the material formation process), terminate at the backside of the irradiated zone. For some, they have the appearance of being bent into the plane of the backside of the irradiated layer. In the extreme case, the irradiated layer completely delaminated off the bulk layer when mechanical stress was applied to the sample during the procedures of sample preparation.

Similar effects were documented in a study of proton-irradiated ZrN, where they hypothesized that voids in the material had been moved through the material by the proton beam front and coalesced at the peak of the damage profile [141]. The result was transgranular cracking with void surfaces having silicon rich oxides. No composition analysis was performed on the ZrC sample studied here. Although, the SThM measurements found the defect regions to be of lower thermal conductance, even though, such “hole”-like regions would typically increase contact surface area with the thermal probe, indicative of lower conductivity material such as oxides.

Further support of the non-existence of a region of peak damage of the material microstructure as seen in the TRIM results can be inferred from molecular dynamics simulations done by Brutzel et al. [142]. Their simulations of collision cascades found that point defects are primarily created while no amorphization was observed. For the given conditions, the damage level in the ZrC may be saturated through proton-damaged zone. Yang et al. showed consistent findings with this ZrC sample in an experimental study, with no evidence of amorphization, but high concentrations of nanometer-sized Frank loops [78]. The primary contribution to the degradation of k_{irr} is attributed to these loop defects acting as phonon scattering sites.

CHAPTER 8

CONCLUSIONS

For the first time, the in-depth thermal conductivity profile of an ion-irradiated material was directly measured. The primary objectives of this work were met through a multi-measurement approach to characterizing the thermal property changes in proton-irradiated ZrC.

8.1. Multi-Measurement Approach

Multiple, high-resolution thermal measurement techniques were used to map the thermal conductivity, *k*, profile of a cross section of a proton-irradiated ZrC sample. Each of the measurement techniques employed were able to capture the thermal property profile induced by the irradiation damage. However each method comes with its own advantages and disadvantages. Also for the first time such methodology has been applied to an irradiated sample. The methods complement and validate each other

- Frequency scanning provides more straightforward thermophysical quantification but requires knowledge of the in-depth profile.
- SThM profiling provides good resolution for estimating irradiation penetration depth and relative characteristics of the profile.
- Possible artifact on R_{th} detection: the used spatial scanning methods involved excitation thermal gradients oriented parallel to the interface with R_{th} (unfavorable configuration for R_{th} detection); in the FD-PTR method, the R_{th} detection is based on the "reflection" of thermal waves traveling perpendicular to the interface with R_{th} (favorable configuration).

Spatial scanning PTR resolution is limited by heating spot size. Lock-in IRT is frequency limited, thus having thermal diffusion lengths too large for good spatial resolution, but has the advantage of quickly imaging the entire cross-section in a single measurement. SThM has the best resolution and gives a good approximation of the profile of thermal conductivity degradation.

However due to difficulties associated with exact reproducibility of tip-sample contact conditions, it requires careful interpretation of results. A summary of the characteristics of each of the measurement techniques used is found in Table 8.1.

Due to the complexity of experimental parameters, the uncertainty contributors of all the measured results are difficult to identify and quantify. One of the strengths of the approach developed in this work is the complementarity of the techniques used. The results of several independent measurements and measurement types corroborate and justify the reported findings from each measurement.

8.2. Thermal Conductivity Degradation in Proton-Irradiated ZrC

The overall *k* profile shape is found to be consistent with numerical predictions being nearly constant over most of the damaged zone, with a thin transition zone to the non-irradiated material. In spite of imperfections in topography, the SThM measured profile is shown to be independent of topography. A calibration of the probe signal was made indicating greater than ≈ 66% reduction of *k* between the damaged and undamaged material. In interpreting the results, it

Table 8.1. Characteristics of thermal conductivity profiling methods used on proton-irradiated ZrC and measured degradation of thermal conductivity.

Method	*Scanning Type*	*Lateral Resolution*	*Probing Depth*	k_{irr} W·m^{-1}·K^{-1}	k_{ZrC} W·m^{-1}·K^{-1}
SThM	Spatial	~ contact radius (~ 1 μm)	~contact radius (~1 μm)	10±2.4	30±10
Lock-in IR Thermography	Spatial	pixel size = 5 μm μ ~ 300 μm	μ ~ 300 μm	(2/3)·k_{ZrC}	-
PTR	Spatial	heating spot size ~50 μm	$\mu \approx$ 1-2 μm	(1/4)·k_{ZrC}	-
PTR	Frequency	measured spot size ~1 mm	$\mu \approx$ 1 mm - 1 μm	11.9±0.5	26.7±1

should be remembered that SThM measurement occurs on a localized area of < 1 μm radius. The measured profiles should not reflect the larger thermal barriers such as grain boundaries found in the non-irradiated ZrC. The results from the spatial scans by PTR show ≈ 75% reduction of *k,* however they are somewhat less reliable due to measuring absolute values of thermal wave amplitude influenced by spatial variabilities of sample surface properties.

Spatial scanning techniques of cross-sections prove valuable when combined with tomographic frequency scanning techniques. Using the measured spatial profile, tomographic PTR results show 55% degradation of thermal conductivity ($k_{\mathrm{irr}} = 11.9\ \mathrm{W \cdot m^{-1} \cdot K^{-1}}$ and $k_{\mathrm{ZrC}} = 26.7\ \mathrm{W \cdot m^{-1} \cdot K^{-1}}$) in ZrC irradiated to 1.75 dpa @ 600°C by a 2.6 MeV proton beam.

The proton-irradiated ZrC has a damage profile lending itself well to a discrete layered approximation used in FD-PTR. The damaged layer is ~52±2 μm thick with a relatively uniform thermal profile. A rather sharp transition to the virgin material was found at the back side of the radiation damaged layer. However, as evidenced by visual study and the tomographic profiles, a thermal resistance exists in the transition zone. Evidence suggests that the thermal resistance is due to the coalescence of void space driven by the proton irradiation front. The existence of such an effect merits further study.

Although SEM images and optical observation provide no indication of grain boundary separation, no irradiation-induced amorphization has been observed in similar ZrC samples [78, 143]. Study of ZrC irradiated after similar irradiation conditions has shown a high concentration of Frank (dislocation) loops in the damaged zone [78]. Therefore, degradation of thermal conductivity in the irradiation-damaged zone is primarily attributed to the presence of a high concentration of Frank loops that act to scatter phonon energy carriers.

8.3. Future Work

The results of this work provide a footing for continued work in investigating thermal degradation of ion-irradiated materials. The methodology used here can be applied to a more systematic study of ZrC or other samples subjected to varying irradiation doses and at various temperatures. The ultimate goal of these studies would be to identify and quantitatively correlate the mechanisms of thermal transport degradation. Proton-irradiated materials seem particularly advantageous for such studies to the uniformity and relatively long depth of the damage profiles, lending themselves well to layered structure approximations.

Additional work continues in the topic of quantitative measurement of thermal conductivity using SThM. In particular, the tuning-fork feedback system at USU is being explored for its potential due to its capability of dual-tip operation as well as vacuum operation.

REFERENCES

[1] Cahill, D. G.,Ford, W. K.,Goodson, K. E.,Mahan, G. D.,Majumdar, A.,Maris, H. J.,Merlin, R., and Phillpot, S. R., 2003, "Nanoscale Thermal Transport," J. App. Phys., 93(2), pp. 793-818.

[2] Cahill, D. G.,Braun, P. V.,Chen, G.,Clarke, D. R.,Fan, S.,Goodson, K. E.,Keblinski, P.,King, W. P.,Mahan, G. D., and Majumdar, A., 2014, "Nanoscale Thermal Transport. II. 2003–2012," Appl. Phys. Rev., 1(1), p. 011305.

[3] Was, G., 2007, *Fundamentals of Radiation Materials Science: Metals and Alloys*, Springer, New York.

[4] Snead, L.,Zinkle, S., and White, D., 2005, "Thermal Conductivity Degradation of Ceramic Materials due to Low Temperature, Low Dose Neutron Irradiation," J. Nucl. Mater., 340(2), pp. 187-202.

[5] Was, G., and Allen, T., 2007, "Radiation Damage from Different Particle Types," Proc. NATO Advanced Study Institute on Radiation Effects in Solids, K. E. Sickafus,E. A. Kotomin, and B. P. Uberuaga, eds., Springer-Verlag, Berlin, pp. 65-98.

[6] Wei, C.,Zheng, X.,Cahill, D. G., and Zhao, J.-C., 2013, "Invited Article: Micron resolution spatially resolved measurement of heat capacity using dual-frequency time-domain thermoreflectance," Rev. Sci. Instrum., 84(7), p. 071301.

[7] Huxtable, S.,Cahill, D. G.,Fauconnier, V.,White, J. O., and Zhao, J.-C., 2004, "Thermal Conductivity Imaging at Micrometre-Scale Resolution for Combinatorial Studies of Materials," Nat. Mater., 3(5), pp. 298-301.

[8] Kim, K.,Jeong, W.,Lee, W., and Reddy, P., 2012, "Ultra-High Vacuum Scanning Thermal Microscopy for Nanometer Resolution Quantitative Thermometry," ACS Nano, 6(5), pp. 4248-4257.

[9] 2004, "Gas-cooled Faster Reactor (GFR) FY04 Annual Report," No. INEEL/EXT-04-02361.

[10] Salazar, A., 2003, "On Thermal Diffusivity," Eur. J. Phys., 24(4), pp. 351-358.

[11] Marin, E., 2007, "The Role of Thermal Properties in Periodic Time-Varying Phenomena," Eur. J. Phys., 28(3), pp. 429-445.

[12] Yovanovich, M. M., 2005, "Four Decades of Research on Thermal Contact, Gap, and Joint Resistance in Microelectronics," IEEE T. Compon. Pack. T., 28(2), pp. 182-206.

[13] Pollack, G. L., 1969, "Kapitza Resistance," Rev. Mod. Phys., 41(1), pp. 48-81.

[14] Chen, G., 2005, *Nanoscale Energy Transport and Conversion: A Parallel Treatment of Electrons, Molecules, Phonons, and Photons*, Oxford University Press, New York.

[15] Zhang, Z. M., 2007, *Nano/Microscale Heat Transfer*, McGraw-Hill, New York.

[16] Touloukian, Y. S., and Ho, C. Y., 1970-1977, "Thermophysical Properties of Matter, The TPRC Data Series (13 Volumes)," Plenum Press, New York.

[17] Maglic, K. D.,Cezairliyan, A., and Peletsky, V. E., 1984, *Compendium of Thermophysical Property Measurement Methods*, Plenum Press, New York.

[18] Maglic, K. D.,Cezairliyan, A., and Peletsky, V. E., 1992, *Compendium of Thermophysical Property Measurement Methods*, Plenum Press, New York.

[19] Swartz, E., and Pohl, R., 1987, "Thermal Resistance at Interfaces," Appl. Phys. Lett., 51(26), pp. 2200-2202.

[20] Swartz, E. T., and Pohl, R. O., 1989, "Thermal Boundary Resistance," Rev. Mod. Phys., 61(3), pp. 605-668.

[21] Kapitza, P., 1941, "The Study of Heat Transfer in Helium II," J. Phys. (USSR), 4(3), pp. 181-210.

[22] Kittel, C., 2005, *Introduction to Solid State Physics*, Wiley, Hoboken, New Jersey.

[23] Ziman, J. M., 2001, *Electrons and Phonons: The Theory of Transport Phenomena in Solids*, Oxford University Press, New York.

[24] Snead, L. L.,Nozawa, T.,Katoh, Y.,Byun, T.-S.,Kondo, S., and Petti, D. A., 2007, "Handbook of SiC Properties for Fuel Performance Modeling," J. Nucl. Mat., 371(1-3), pp. 329-377.

[25] Clinard, F. W., and Hobbs, L. W., 1986, "Radiation Effects in Non-Metals,," *Physics of Radiation Effects in Crystals*, R. A. Johnson and A. N. Orlov, eds., Elsevier Science Publishers, Amsterdam, pp. 387-471.

[26] Hobbs, L. W.,Clinard, F. W.,Zinkle, S. J., and Ewing, R. C., 1994, "Radiation Effects in Ceramics," J. Nucl. Mater., 216, pp. 291-321.

[27] Fink, D., 2004, *Fundamentals of Ion-Irradiated Polymers*, Springer-Verlag, Berlin.

[28] Was, G.,Busby, J.,Allen, T.,Kenik, E.,Jensson, A.,Bruemmer, S.,Gan, J.,Edwards, A.,Scott, P., and Andreson, P., 2002, "Emulation of Neutron Irradiation Effects with Protons: Validation of Principle," J. Nucl. Mater., 300(2), pp. 198-216.

[29] Almond, D. P., and Patel, P., 1996, *Photothermal Science and Techniques*, Chapman and Hall, London, UK.

[30] Angstrom, A. J., 1861, "Bestimmung der warme leitung durch periodische temperaturanderung," Ann. Phys. Chem., 114, pp. 513-530.

[31] Rosencwaig, A., and Gersho, A., 1976, "Theory of the Photoacoustic Effect with Solids," J. Appl. Phys., 47(1), pp. 64-69.

[32] Cahill, D. G., 1990, "Thermal Conductivity Measurement from 30 to 750 K: the 3ω Method," Rev. Sci. Instrum., 61(2), pp. 802-808.

[33] Glorieux, C.,Fivez, J., and Thoen, J., 1993, "Photoacoustic Investigation of the Thermal Properties of Layered Materials: Calculation of the Forward Signal and Numerical Inversion Procedure," J. Appl. Phys., 73(2), pp. 684-690.

[34] Lan, T.,Seidel, U., and Walther, H., 1995, "Theory of Microstructural Depth Profiling by Photothermal Measurements," J. Appl. Phys., 77(9), pp. 4739-4745.

[35] Matvienko, A.,Mandelis, A., and Abrams, S., 2009, "Robust Multiparameter Method of Evaluating the Optical and Thermal Properties of a Layered Tissue Structure using Photothermal Radiometry," Appl. Opt., 48(17), pp. 3192-3203.

[36] Celorrio, R.,Apiñaniz, E.,Mendioroz, A.,Salazar, A., and Mandelis, A., 2010, "Accurate Reconstruction of the Thermal Conductivity Depth Profile in Case Hardened Steel," J. Appl. Phys., 107(8), p. 083519.

[37] Kuriakose, M.,Depriester, M.,Mascot, M.,Longuemart, S.,Fasquelle, D.,Carru, J., and Sahraoui, A. H., 2013, "Thermal Parameter Extraction of a Multilayered System by a Genetic Algorithm," Int. J. Thermophys., 34(8-9), pp. 1569-1578.

[38] Mandelis, A., 2001, *Diffusion-Wave Fields: Mathematical Methods and Green Functions*, Springer, New York.

[39] Maillet, D.,André, S.,Batsale, J.-C.,Degiovanni, A., and Maillet, D., 2000, *Thermal Quadrupoles: Solving the Heat Equation through Integral Transforms*, Wiley, Chichester, UK.

[40] Salazar, A.,Fuentes, R.,Apinaniz, E.,Mendioroz, A., and Celorrio, R., 2011, "Simultaneous measurement of thermal diffusivity and optical absorption coefficient using photothermal radiometry. II Multilayered solids," J. Appl. Phys., 110(3), pp. 033516-033516-033518.

[41] Chirtoc, M., 2009, "Investigation of Layered Systems by Photothermal Methods with Periodic Excitation," *Thermal Wave Physics and Related Photothermal Techniques: Basic Principles and Recent Developments*, E. Marin, ed., Transworld Research Network, Kerala, India, pp. 29-63.

[42] Marin, E., 2009, *Thermal Wave Physics and Related Photothermal Techniques: Basic Principles and Recent Developments*, Transworld Research Network, Kerala, India.

[43] Vargas, H., and Miranda, L., 2003, "Photothermal Techniques Applied to Thermophysical Properties Measurements," Rev. Sci. Instrum., 74(1), pp. 794-799.

[44] Bialkowski, S. E., 1996, *Photothermal Spectroscopy Methods for Chemical Analysis*, Wiley, New York.

[45] Bell, A. G., 1880, "On the Production and Reproduction of Sound by Light," Am. J. Sci., 20(118), pp. 305-324.

[46] Kreuzer, L., 1971, "Ultralow Gas Concentration Infrared Absorption Spectroscopy," J. Appl. Phys., 42(7), pp. 2934-2943.

[47] Rosencwaig, A., 1973, "Photoacoustic Spectroscopy of Solids," Opt. Commun., 7(4), pp. 305-308.

[48] Olmstead, M.,Amer, N.,Kohn, S.,Fournier, D., and Boccara, A., 1983, "Photothermal Displacement Spectroscopy: An Optical Probe for Solids and Surfaces," Appl Phys. A, 32(3), pp. 141-154.

[49] Nordal, P. E., and Kanstad, S. O., 1979, "Photothermal Radiometry," Phys. Scripta, 20(5-6), pp. 659-662.

[50] Nordal, P. E., and Kanstad, S. O., 1985, "New Developments in Photothermal Radiometry," Infrared Phys., 25(1), pp. 295-304.

[51] Coufal, H., 1984, "Photothermal Spectroscopy using a Pyroelectric Thin-Film Detector," Appl. Phys. Lett., 44(1), pp. 59-61.

[52] Mandelis, A., 1984, "Frequency-Domain Photopyroelectric Spectroscopy of Condensed Phases (PPES): A New, Simple and Powerful Spectroscopic Technique," Chem. Phys. Lett., 108(4), pp. 388-392.

[53] Dădârlat, D.,Chirtoc, M.,Candea, R., and Bratu, I., 1984, "Direct Pyroelectric Detection of Optical Absorption in Non-Transparent Materials," Infrared Phys., 24(5), pp. 469-471.

[54] Boccara, A.,Jackson, W.,Amer, N. M., and Fournier, D., 1980, "Sensitive Photothermal Deflection Technique for Measuring Absorption in Optically Thin Media," Opt. Lett., 5(9), pp. 377-379.

[55] Jackson, W. B.,Amer, N. M.,Boccara, A., and Fournier, D., 1981, "Photothermal Deflection Spectroscopy and Detection," Appl. Opt., 20(8), pp. 1333-1344.

[56] Rosencwaig, A.,Opsal, J.,Smith, W., and Willenborg, D., 1985, "Detection of Thermal Waves through Optical Reflectance," Appl. Phys. Lett., 46(11), pp. 1013-1015.

[57] Paddock, C. A., and Eesley, G. L., 1986, "Transient Thermoreflectance from Thin Metal Films," J. Appl. Phys., 60(1), pp. 285-290.

[58] Williams, C., and Wickramasinghe, H., 1986, "Scanning Thermal Profiler," Appl. Phys. Lett., 49(23), pp. 1587-1589.

[59] Dinwiddie, R.,Pylkki, R., and West, P., 1993, "Thermal Conductivity Contrast Imaging with a Scanning Thermal Microscope," *Thermal Conductivity 22*, T. W. Wong, ed., Tecnomic Publishing Company, Lancaster, PA, pp. 668-668.

[60] Majumdar, A.,Carrejo, J., and Lai, J., 1993, "Thermal Imaging Using the Atomic Force Microscope," Appl. Phys. Lett., 62(20), pp. 2501-2503.

[61] Chirtoc, M.,Antoniow, J.,Henry, J.,Dole, P., and Pelzl, J., 2008, "1ω, 2ω, 3ω Scanning Thermal Microscopy (SThM) and Combinations with Thermographic, Radiometric, Pyroelectric and Thermoelastic Techniques; Principles and Applications," *Advanced Techniques and Applications on Scanning Probe Microscopy*, F. Lei and J. L. Bubendorff, eds., Transworld Research Network, Kerala, India, pp. 197-247.

[62] Hammiche, A.,Price, D.,Dupas, E.,Mills, G.,Kulik, A.,Reading, M.,Weaver, J., and Pollock, H., 2000, "Two New Microscopical Variants of Thermomechanical Modulation: Scanning Thermal Expansion Microscopy and Dynamic Localized Thermomechanical Analysis," J. Microsc-Oxford, 199(3), pp. 180-190.

[63] Bolte, J.,Niebisch, F.,Pelzl, J.,Stelmaszyk, P., and Wieck, A., 1998, "Study of the Hot Spot of an In-Plane Gate Transistor by Scanning Joule Expansion Microscopy," J. Appl. Phys., 84(12), pp. 6917-6922.

[64] Varesi, J., and Majumdar, A., 1998, "Scanning Joule Expansion Microscopy at Nanometer Scales," Appl. Phys. Lett., 72(1), pp. 37-39.

[65] Pelzl, J.,Chirtoc, M., and Meckenstock, R., 2013, "Thermal Wave-Based Scanning Probe Microscopy and Its Applications," Int. J. Thermophys., 34(8-9), pp. 1353-1366.

[66] Dietzel, D.,Chotikaprakhan, S.,Bein, B., and Pelzl, J., 2005, "Analysis of Active Semiconductor Structures by Combined SThM and SThEM," J. Phys. IV, 125, pp. 87-91.

[67] Gurrum, S. P.,King, W. P.,Joshi, Y. K., and Ramakrishna, K., 2008, "Size Effect on the Thermal Conductivity of Thin Metallic Films investigated by Scanning Joule Expansion Microscopy," J. Heat Transf., 130(8), p. 082403.

[68] Grosse, K. L.,Bae, M.-H.,Lian, F.,Pop, E., and King, W. P., 2011, "Nanoscale Joule heating, Peltier Cooling and Current Crowding at Graphene-Metal Contacts," Nat. Nanotechnol., 6(5), pp. 287-290.

[69] Jensen, C.,Xing, C.,Folsom, C.,Ban, H., and Phillips, J., 2012, "Design and Validation of a High-Temperature Comparative Thermal-Conductivity Measurement System," Int. J. Thermophys., 33(2), pp. 311-329.

[70] Xing, C.,Jensen, C.,Ban, H., and Phillips, J., 2011, "Uncertainty Analysis on the Design of Thermal Conductivity Measurement by a Guarded Cut-Bar Technique," Meas. Sci. Technol., 22(7), p. 075702.

[71] Xing, C.,Jensen, C.,Folsom, C.,Ban, H., and Marshall, D. W., 2014, "An Optimal Guarding Scheme for Thermal Conductivity Measurement using a Guarded Cut-Bar Technique, Part 1 Experimental Study," Appl. Therm. Eng., 62(2), pp. 850-857.

[72] Xing, C.,Jensen, C.,Folsom, C.,Ban, H., and Marshall, D. W., 2013, "An Optimal Guarding Scheme for Thermal Conductivity Measurement using a Guarded Cut-Bar Technique, Part 2 Guarding Mechanism," Appl. Therm. Eng., 59(1), pp. 504-514.

[73] Xing, C.,Folsom, C.,Jensen, C.,Ban, H., and Marshall, D. W., 2014, "A Correction Scheme for Thermal Conductivity Measurement using the Comparative Cut-Bar Technique Based on 3D Numerical Simulation," Meas. Sci. Technol., 25(5), p. 055602.

[74] Xing, C.,Jensen, C.,Hua, Z.,Ban, H.,Hurley, D.,Khafizov, M., and Kennedy, J. R., 2012, "Parametric Study of the Frequency-Domain Thermoreflectance Technique," J. Appl. Phys., 112(10), p. 103105.

[75] Antoniow, J.,Maigret, J.-E.,Jensen, C.,Trannoy, N.,Chirtoc, M., and Beaugrand, J., 2012, "Glass-Transition Temperature Profile Measured in a Wood Cell Wall Using Scanning Thermal Expansion Microscope (SThEM)," Int. J. Thermophys., 33(10-11), pp. 2167-2172.

[76] Antoniow, J.,Chirtoc, M.,Drevet, R.,Jensen, C., and Benhayoune, H., 2012, "A Simple Method to Assess Surface Roughness by Photothermal Investigation (PTR) Using an Effective Semitransparent Layer," Int. J. Thermophys., 33(10-11), pp. 1960-1965.

[77] Katoh, Y.,Vasudevamurthy, G.,Nozawa, T., and Snead, L. L., 2013, "Properties of Zirconium Carbide for Nuclear Fuel Applications," J. Nucl. Mater., 441(1), pp. 718-742.

[78] Yang, Y.,Dickerson, C. A.,Swoboda, H.,Miller, B., and Allen, T. R., 2008, "Microstructure and Mechanical Properties of Proton Irradiated Zirconium Carbide," J. Nucl. Mater., 378(3), pp. 341-348.

[79] Snead, L. L.,Katoh, Y., and Kondo, S., 2010, "Effects of Fast Neutron Irradiation on Zirconium Carbide," J. Nucl. Mater., 399(2-3), pp. 200-207.

[80] Taylor, R., and Storms, E., 1976, "Thermal Transport in Refractory Carbides," *Thermal Conductivity 14*, P. G. Klemens and T. K. Chu, eds., Plenum Press, New York, pp. 161-174.

[81] Williams, W. S., 1998, "The Thermal Conductivity of Metallic Ceramics," JOM - J. Min. Met. Mat. S., 50(6), pp. 62-66.

[82] Taubin, M. L.,Fateev, S. V.,Ivanov, M. V., and Shutov, P. V., 1991, "Change of the Physical Properties of Zirconium Carbide in a Short Exposure to a Neutron Current," Atom Energy, 70(1), pp. 74-76.

[83] David, L.,Gomès, S.,Carlot, G.,Roger, J.,Fournier, D.,Valot, C., and Raynaud, M., 2008, "Characterization of Thermal Conductivity Degradation Induced by Heavy Ion Irradiation in Ceramic Materials," J. Phys. D Appl. Phys., 41(3), p. 035502.

[84] Touloukian, Y. S., and Buyco, E. H., 1970, *Thermohpysical Properties of Matter, vol. 5 Specific Heat Nonmetallic Solids*, IFI/Plenum Press, New York.

[85] Westrum Jr, E. F., and Feick, G., 1963, "Zirconium Carbide: Heat Capacity and Thermodynamic Properties from 5 to 350°K," J. Chem. Eng. Data, 8(2), pp. 176-178.

[86] Ziegler, J. F.,Biersack, J. P., and Ziegler, M. D., 2008, *SRIM: The Stopping and Range of Ions in Matter*, SRIM Company, Chester, MD.

[87] Cabrero, J.,Audubert, F.,Pailler, R.,Kusiak, A.,Battaglia, J., and Weisbecker, P., 2010, "Thermal Conductivity of SiC after Heavy Ions Irradiation," J. Nucl. Mater., 396(2-3), pp. 202-207.

[88] Horne, K.,Ban, H.,Mandelis, A., and Matvienko, A., 2012, "Photothermal Radiometry Measurement of Thermophysical Property Change of an Ion-Irradiated Sample," Mater. Sci. Eng., 177(2), pp. 164-167.

[89] David, L., 2006, "Développement de la microscopie thermique à sonde locale pour la détermination de la conductivité thermique de films minces: Application aux céramiques pour le nucléaire " PhD T, L'Institut National des Sciences Appliques de Lyon, France.

[90] Leung, W. P., and Tam, A. C., 1984, "Thermal Diffusivity in Thin Films Measured by Noncontact Single-Ended Pulsed-Laser-Induced Thermal Radiometry," Opt. Lett., 9(3), pp. 93-95.

[91] Santos, R., and Miranda, L., 1981, "Theory of the Photothermal Radiometry with Solids," J. Appl. Phys., 52(6), pp. 4194-4198.

[92] Tom, R. D.,O'Hara, E. P., and Benin, D., 1982, "A Generalized Model of Photothermal Radiometry," J. Appl. Phys., 53(8), pp. 5392-5400.

[93] Nicolaides, L.,Feng, C.,Mandelis, A., and Abrams, S. H., 2002, "Quantitative Dental Measurements by Use of Simultaneous Frequency-Domain Laser Infrared Photothermal Radiometry and Luminescence," Appl. Opt., 41(4), pp. 768-777.

[94] Fuentes, R.,Apinaniz, E.,Mendioroz, A., and Salazar, A., 2011, "Simultaneous Measurement of Thermal Diffusivity and Optical Absorption Coefficient Using Photothermal Radiometry. I. Homogeneous Solids," J. Appl. Phys., 110(3), pp. 033515-033519.

[95] Chirtoc, M.,Horny, N.,Henry, J.-F.,Turgut, A.,Kökey, I.,Tavman, I., and Omastová, M., 2012, "Photothermal Characterization of Nanocomposites Based on High Density Polyethylene (HDPE) Filled with Expanded Graphite," Int. J. Thermophys., 33(10-11), pp. 2110-2117.

[96] Hendler, E.,Crosbie, R., and Hardy, J. D., 1958, "Measurement of Heating of the Skin during Exposure to Infrared Radiation," J. Appl. Physiol., 12(2), pp. 177-185.

[97] Carlomagno, G., and Berardi, P., 1976, "Unsteady Thermotopography in Non-Destructive Testing," Proc. Infrared Information Exchange III, C. Warren, ed., St. Louis, MO, pp. 33-40.

[98] Busse, G.,Wu, D., and Karpen, W., 1992, "Thermal wave imaging with phase sensitive modulated thermography," J. Appl. Phys., 71(8), pp. 3962-3965.

[99] Choi, M.,Kang, K.,Park, J.,Kim, W., and Kim, K., 2008, "Quantitative determination of a subsurface defect of reference specimen by lock-in infrared thermography," NDT&E Int., 41(2), pp. 119-124.

[100] Montanini, R., 2010, "Quantitative Determination of Subsurface Defects in a Reference Specimen Made of Plexiglas by Means of Lock-in and Pulse Phase Infrared Thermography," Infrared Phys. Techn., 53(5), pp. 363-371.

[101] Bagavathiappan, S.,Lahiri, B.,Saravanan, T.,Philip, J., and Jayakumar, T., 2013, "Infrared Thermography for Condition Monitoring–A Review," Infrared Phys. Techn., 60, pp. 35-55.

[102] Binnig, G.,Rohrer, H.,Gerber, C., and Weibel, E., 1982, "Surface Studies by Scanning Tunneling Microscopy," Phys. Rev. Lett., 49(1), pp. 57-61.

[103] Binnig, G.,Rohrer, H., and Gerber, C., 1986, "Atomic Force Microscopy," Phys. Rev. Lett., 56(9), pp. 930-933.

[104] Nonnenmacher, M., and Wickramasinghe, H., 1992, "Scanning Probe Microscopy of Thermal Conductivity and Subsurface Properties," Appl. Phys. Lett., 61(2), pp. 168-170.

[105] Majumdar, A., 1999, "Scanning Thermal Microscopy," Annu. Rev. Mater. Sci., 29(1), pp. 505-585.

[106] Cretin, B.,Gomès, S.,Trannoy, N., and Vairac, P., 2007, "Scanning Thermal Microscopy," *Microscale and Nanoscale Heat Transfer*, S. Volz, ed., Springer-Verlag, Berlin, pp. 181-238.

[107] Gomès, S., and Lefèvre, S., 2008, "Scanning Thermal Microscopy: Advances of the Technique for the Characterization of the Thermophysical Properties of Solid Materials," *Advanced Techniques and Applications on Scanning Probe Microscopy*, F. Lei and J. L. Bubendorff, eds., Transworld Research Network, Kerala, India, pp. 157-195.

[108] Karrai, K., and Grober, R. D., 1995, "Piezoelectric Tip-Sample Distance Control for Near Field Optical Microscopes," Appl. Phys. Lett., 66(14), pp. 1842-1844.

[109] Nanonics Imaging, Ltd., 2014, http://www.nanonics.co.il/.

[110] Cretin, B., 2004, "Scanning Near-Field Thermal and Thermoacoustic Microscopy: Performances and Limitations," Superlattice Microst., 35(3), pp. 253-268.

[111] Kelvin Nanotechnology, 2014, http://www.kelvinnanotechnology.com/.

[112] Mills, G.,Zhou, H.,Midha, A.,Donaldson, L., and Weaver, J., 1998, "Scanning Thermal Microscopy using Batch Fabricated Thermocouple Probes," Appl. Phys. Lett., 72(22), pp. 2900-2902.

[113] Lieberman, K.,Lewis, A.,Fish, G.,Shalom, S.,Jovin, T. M.,Schaper, A., and Cohen, S. R., 1994, "Multifunctional, Micropipette Based Force Cantilevers for Scanned Probe Microscopy," Appl. Phys. Lett., 65(5), pp. 648-650.

[114] Fish, G.,Bouevitch, O.,Kokotov, S.,Lieberman, K.,Palanker, D.,Turovets, I., and Lewis, A., 1995, "Ultrafast Response Micropipette-Based Submicrometer Thermocouple," Rev. Sci. Instrum., 66(5), pp. 3300-3306.

[115] Dekhter, R.,Khachatryan, E.,Kokotov, Y.,Lewis, A.,Kokotov, S.,Fish, G.,Shambrot, Y., and Lieberman, K., 2000, "Investigating Material and Functional Properties of Static Random Access Memories using Cantilevered Glass Multiple-Wire Force-Sensing Thermal Probes," Appl. Phys. Lett., 77(26), pp. 4425-4427.

[116] Shi, L., and Majumdar, A., 2002, "Thermal Transport Mechanisms at Nanoscale Point Contacts," J. Heat Transf., 124(2), pp. 329-337.

[117] Nelson, B. A., and King, W. P., 2008, "Modeling and Simulation of the Interface Temperature Between a Heated Silicon Tip and a Substrate," Nanosc. Microsc. Therm., 12(1), pp. 98-115.

[118] Gomès, S.,Trannoy, N., and Grossel, P., 1999, "DC Thermal Microscopy: Study of the Thermal Exchange between a Probe and a Sample," Meas. Sci. Technol., 10(9), pp. 805-811.

[119] Lefèvre, S.,Volz, S., and Chapuis, P. O., 2006, "Nanoscale Heat Transfer at Contact between a Hot Tip and a Substrate," Int. J. Heat Mass Tran., 49(1-2), pp. 251-258.

[120] Chapuis, P.-O.,Greffet, J.-J.,Joulain, K., and Volz, S., 2006, "Heat Transfer Between a Nano-Tip and a Surface," Nanotechnology, 17(12), pp. 2978-2981.

[121] Kim, K.,Chung, J.,Won, J.,Kwon, O.,Lee, J. S.,Park, S. H., and Choi, Y. K., 2008, "Quantitative Scanning Thermal Microscopy Using Double Scan Technique," Appl. Phys. Lett., 93(20), p. 203115.

[122] Kim, K.,Chung, J.,Hwang, G.,Kwon, O., and Lee, J. S., 2011, "Quantitative Measurement with Scanning Thermal Microscope by Preventing the Distortion due to the Heat Transfer through the Air," ACS Nano, 5(11), pp. 8700-8709.

[123] Soudi, A.,Dawson, R. D., and Gu, Y., 2010, "Quantitative Heat Dissipation Characteristics in Current-Carrying GaN Nanowires Probed by Combining Scanning Thermal Microscopy and Spatially Resolved Raman Spectroscopy," ACS Nano, 5(1), pp. 255-262.

[124] Lefèvre, S.,Volz, S.,Saulnier, J. B.,Fuentes, C., and Trannoy, N., 2003, "Thermal Conductivity Calibration for Hot Wire Based dc Scanning Thermal Microscopy," Rev. Sci. Instrum., 74(4), pp. 2418-2423.

[125] Puyoo, E.,Grauby, S.,Rampnoux, J.-M.,Rouvière, E., and Dilhaire, S., 2011, "Scanning Thermal Microscopy of Individual Silicon Nanowires," J. Appl. Phys., 109(2), p. 024302.

[126] Altes, A.,Heiderhoff, R., and Balk, L., 2004, "Quantitative Dynamic Near-Field Microscopy of Thermal Conductivity," J. Phys. D Appl. Phys., 37(6), pp. 952-963.

[127] Chirtoc, M.,Gibkes, J.,Wernhardt, R.,Pelzl, J., and Wieck, A., 2008, "Temperature-Dependent Quantitative 3ω Scanning Thermal Microscopy: Local Thermal Conductivity Changes in NiTi Microstructures Induced by Martensite-Austenite Phase Transition," Rev. Sci. Instrum., 79(9), p. 093703.

[128] Bodzenta, J.,Juszczyk, J., and Chirtoc, M., 2013, "Quantitative Scanning Thermal Microscopy Based on Determination of Thermal Probe Dynamic Resistance," Rev. Sci. Instrum., 84(9), p. 093702.

[129] Bodzenta, J.,Kazmierczak-Balata, A.,Lorenc, M., and Juszczyk, J., 2010, "Analysis of Possibilities of Application of Nanofabricated Thermal Probes to Quantitative Thermal Measurements," Int. J. Thermophys., 31(1), pp. 150-162.

[130] Jensen, C.,Chirtoc, M.,Antoniow, J., and Ban, H., 2013, "In-Depth Thermal-Conductivity Profile of Ion-Irradiated Zirconium Carbide Using Scanning Thermal Microscopy," Int. J. Thermophys., 34(4), pp. 597-608.

[131] Jensen, C.,Chirtoc, M.,Horny, N.,Antoniow, J.,Pron, H., and Ban, H., 2013, "Thermal Conductivity Profile Determination in Proton-Irradiated ZrC by Spatial and Frequency Scanning Thermal Wave Methods," J. Appl. Phys., 114(13), p. 133509.

[132] David, L.,Gomès, S., and Raynaud, M., 2007, "Modelling for the Thermal Characterization of Solid Materials by DC Scanning Thermal Microscopy," J. Phys. D Appl. Phys., 40(14), pp. 4337-4346.

[133] Ozaki, Y., and Zee, R. H., 1995, "Investigation of Thermal and Hydrogen Effects on Emissivity of Refractory Metals and Carbides," Mat. Sci. Eng. A-Struct., 202(1), pp. 134-141.

[134] Lengauer, W.,Binder, S.,Aigner, K.,Ettmayer, P.,Guillou, A.,Debuigne, J., and Groboth, G., 1995, "Solid State Properties of Group IVb Carbonitrides," J. Alloy Compd., 217(1), pp. 137-147.

[135] Taylor, R., and Morreale, J., 1964, "Thermal Conductivity of Titanium Carbide, Zirconium Carbide, and Titanium Nitride at High Temperatures," J. Am. Ceram. Soc., 47(2), pp. 69-73.

[136] Touloukian, Y. S.,Powell, R. W.,Ho, C. Y., and Klemens, P. G., 1970, *Thermohpysical Properties of Matter, vol. 2 Thermal Conductivity Nonmetallic Solids*, IFI/Plenum Press, New York.

[137] Storms, E. K., and Wagner, P., 1973, "Thermal Conductivity of Substoichiometric ZrC and NbC," High Temp. Sci., 5(6), pp. 454-462.

[138] Lee, C. W., 1982, "Thermal Properties of Neutron-Irradiated SiC: Effects of Boron Doping," J. Nucl. Mater., 108-109, pp. 678-684.

[139] Touloukian, Y. S.,Powell, R. W.,Ho, C. Y., and Klemens, P. G., 1971, *Thermophysical Properties of Matter*, IFI/Plenum Press, New York.

[140] Clarke, D. R., 2003, "Materials Selection Guidelines for Low Thermal Conductivity Thermal Barrier Coatings," Surf. Coat. Tech., 163-164, pp. 67-74.

[141] Yang, Y.,Dickerson, C. A., and Allen, T. R., 2009, "Radiation Stability of ZrN under 2.6 MeV Proton Irradiation," J. Nucl. Mater., 392(2), pp. 200-205.

[142] Van Brutzel, L., and Crocombette, J., 2007, "Classical Molecular Dynamics Study of Primary Damage Created by Collision Cascade in a ZrC Matrix," Nucl. Instrum. Meth. B, 255(1), pp. 141-145.

[143] Gan, J.,Yang, Y.,Dickson, C., and Allen, T., 2009, "Proton Irradiation Study of GFR Candidate Ceramics," J. Nucl. Mater., 389(2), pp. 317-325.

CURRICULUM VITAE

COLBY JENSEN

Department of Mechanical & Aerospace Engineering
Utah State University
Phone: 435-512-1344
Email: colby.jensen@aggiemail.usu.edu

EDUCATION

2014 **Utah State University** Logan, Utah, USA
University of Reims Champagne-Ardenne Reims, France
Ph.D. in Mechanical Engineering **(Cotutelle Program)**
Dissertation: Bridging the Nano and Macro Worlds: Thermal Property Measurement using Scanning Thermal Microscopy and Photothermal Radiometry – Application to Particle-Irradiation Damage Profile in ZrC
Received highest French rating: “Très honorable avec les félicitations du jury”
“Very honorable with congratulations of the jury”
Co-Advisor (USU): Prof. Heng Ban
Co-Advisor (URCA): Prof. Mihai Chirtoc

2010 **Utah State University** Logan, Utah, USA
M.S. in Mechanical Engineering 4.0 GPA
Thesis: TRISO Fuel Compact Thermal Conductivity Measurement Instrument Development
Advisor: Prof. Heng Ban

2008 **Utah State University** Logan, Utah, USA
B.S. in Mechanical Engineering 3.98 GPA
Valedictorian of the College of Engineering
Successful Completion of the Fundamentals of Engineering Exam (2007)

FELLOWSHIPS, HONORS, AWARDS

2014 **Dissertation awarded highest French distinction**, “Très honorable avec les félicitations du jury – Very honorable with congratulations of the jury"
2014 **Dissertation Fellowship**, School of Graduate Studies, Utah State University
2014 **Outstanding Graduate Scholar**, College of Engineering., Utah State University
2014 **Outstanding Graduate Teaching Assistant**, Dept. of Mechanical & Aerospace Engr., Utah State University
2012 **Outstanding PhD Researcher**, Dept. of Mech. & Aerospace Engr., Utah State University
2011 **Chateaubriand Fellowship** from the Embassy of France in the United States
2011 **NSF International Research Fellowship** from the International Center for Materials Research, Silesian University of Technology, Gliwice, Poland

2010 **DOE Nuclear Energy University Program (DOE-NEUP) Graduate Fellowship** ($150,000 for 3 years)
2008 **Valedictorian, College of Engineering**, Utah State University
2008 **Valedictorian, Dept. of Mechanical & Aerospace Engineering**, Utah State University
2008 Rio Tinto-Kennecott Scholar
2007 Outstanding Junior, Dept. of Mechanical & Aerospace Engineering, Utah State University
2006 Pre-professional Academic Excellence Award, Dept. of Mechanical & Aerospace Engineering, Utah State University
2001 Presidential Scholarship (4 years), Utah State University

RESEARCH INTERESTS

Energy transport in condensed matter, liquids, gases, and material interfaces; nano/microscale heat transfer; thermophysical characterization of materials for energy transport, conversion, generation, and storage for various applications including nuclear energy and propulsion, solar energy, aerospace, semiconductor, biomaterials, and advanced manufacturing using:

- Atomic force microscope (AFM) based thermophysical characterization technique development including single and multiprobe approaches for quantifiable nanoscale thermal characterization
- Optical techniques such as photothermal radiometry and thermoreflectance techniques for microscale and bulk measurements of multilayered materials
- 3ω techniques for thin fibers and films, liquids, AFM
- Classic thermal property measurement techniques - steady-state guarded, transient hot-wire, differential scanning calorimetry for bulk measurements of solids, fluids, and composites

RESEARCH EXPERIENCE

2008-present **Utah State University** Logan, Utah, USA

Graduate Research Assistant: Multiscale Thermophysics Laboratory

- Leadership role/student advisement in thermal properties measurement laboratory
- Development of scanning thermal microscopy for quantitative measurement
- Photothermal measurements of multilayered materials
- Characterization of ion-irradiated material
- Performed measurements on surrogate nuclear fuel sample
- Various thermal property measurement techniques (3ω, hot-wire, steady-state)

2011-2012 **University of Reims Champagne-Ardenne** Reims, France

Graduate Research Assistant: Multiscale Thermophysics Group (GRESPI-CATHERM)

- Atomic force microscopy (AFM) to characterize samples
- Development of scanning thermal microscopy for quantitative thermal measurements
- Photothermal radiometry for thermal measurements of layered materials
- Characterization of thermal contact resistance

2011 **Silesian University of Technology** Gliwice, Poland

Guest Researcher: Department of Applied Physics

- Characterized nanoscale topography and thermal properties using atomic force microscopy (AFM) based scanning thermal microscopy (SThM) and photothermal techniques

TEACHING EXPERIENCE

2014 & 2013 **Utah State University** Logan, Utah, USA

Instructor: Undergraduate Heat and Mass Transfer Course (MAE 3440)

- Full responsibility in designing and teaching core, required course 100+ students
- Teaching rating comparable to average MAE

2008 **Utah State University** Logan, Utah, USA

Project Advising Assistant: Senior Capstone Design Project

- Served as an advisor to a group of seniors building a dynamometer for a small bio-diesel engine

2007 **Utah State University** Logan, Utah, USA

Teaching Assistant: Undergraduate Engineering Dynamics Course

- Conducted help sessions in classroom setting for 2+ hours/week and grading

RELATED PROFESSIONAL EXPERIENCE

2007-2008 **Young Electric Sign Company** Logan, Utah, USA

Design Engineer: Engineering Department

- Assisted in manufacturing processes and design of various mechanical systems
- Compiled documentation for product lifecycle management system
- Created CAD models and drawings

2006 & 2007 **ATK Launch Systems**: Promontory, Utah, USA

Engineering Intern: Thermal Insulation Design & Analysis Group

- Assisted in designing, assembling, & post-fire analysis of test rocket motors
- Characterized mechanical property of rocket insulator material
- Formal presentations of test results to multiple customers

PROPOSAL EXPERIENCE

Chateaubriand Fellowship, "Bridging the Nano and Macro Worlds: Nanoscale Thermal Property Measurement using Scanning Thermal Microscopy," Office of Science and Technology, Embassy of France in the United States, Awarded, September 2011 - August 2012, $20,000

NSF International Research Fellowship, "Nanoscale Thermal Property Measurement using Scanning Thermal Microscopy," NSF - International Center for Materials Research, Awarded, July 2011 - August 2011, $5,000

DOE Graduate Fellowship, "Irradiation Damage and Thermomechanical and Thermophysical Properties of ZrC," DOE Nuclear Energy University Program, Awarded, September 2010 - August 2013, $150,000

JOURNAL PUBLICATIONS

1. C. Xing, C. Jensen, T. Munro, B. White, H. Ban, and M. Chirtoc, “Accurate Thermal Property Characterization of Fine Fibers by the 3-omega Technique,” Appl. Therm. Engr., *Accepted* (2014).

2. C. Xing, C. Jensen, T. Munro, B. White, H. Ban, and M. Chirtoc, “Thermal Property Characterization of Fine Fibers by the 3-omega Technique,” Appl. Therm. Engr., *Accepted* (2014).

3. C. Xing, T. Munro, C. Jensen, B. White, and H. Ban, “Thermal Characterization of Fine Fibers using an Improved Direct Electrical Heating Method,” Int. J. Thermophys., *Accepted* (2014).

4. C. Xing, C. Folsom, C. Jensen, H. Ban, and D. Marshall, "A Correction Scheme for Thermal Conductivity Measurement Using the Comparative Cut-bar Technique Based on 3D Numerical Simulation," Meas. Sci. Technol. **25** 055602 (2014).

5. C. Jensen, M. Chirtoc, J.S. Antoniow, N. Horny, H. Pron and H. Ban, "Thermal Conductivity Profile Determination in Proton-Irradiated ZrC by Spatial and Frequency Scanning Thermal Wave Methods," J. Appl. Phys. **114** 133509 (2013).

6. C. Xing, T. Munro, C. Jensen, and H. Ban, "Analysis of the Electrothermal Technique for Thermal Property Characterization of Thin Fibers," Meas. Sci. Technol. **24** 105603 (2013).

7. C. Xing, C. Jensen, C. Folsom, H. Ban, and D. Marshall, "An Optimal Guarding Scheme for Thermal Conductivity Measurement Using a Guarded Cut-Bar Technique, Part 2 Guarding Mechanism," Appl. Therm. Engr. **59** 504 (2013).

8. C. Xing, C. Jensen, C. Folsom, H. Ban, and D. Marshall, "An Optimal Guarding Scheme for Thermal Conductivity Measurement Using a Guarded Cut-Bar Technique Part I: Experimental Study," Appl. Therm. Engr. **62** 850 (2013).

9. C. Jensen, M. Chirtoc, J.S. Antoniow, and H. Ban, "In-Depth Thermal Conductivity Profile of Ion-Irradiated Zirconium Carbide using Scanning Thermal Microscopy", Int. J. Thermophys. **34** 597 (2012).

10. J.S. Antoniow, M. Chirtoc, R. Drevet, C. Jensen, and H. Benhayoune, "A Simple Method to Assess Surface Roughness by Photothermal Investigation (PTR) by Means of an Effective Semitransparent Layer," Int. J. Thermophys. **33** 1960 (2012)

11. J.S. Antoniow, J.E. Maigret, C. Jensen, N. Trannoy M. Chirtoc, and J. Beaugrand, "Glass Transition Temperature Profile Measured in a Wood Cell Wall Using Scanning Thermal Expansion Microscopy (SThEM)," Int. J. Thermophys. **33** 2167 (2012)

12. C. Xing, C. Jensen, Z. Hua, H. Ban, D. Hurley, and J.R. Kennedy, "Parametric Study of the Frequency-Domain Thermoreflectance Technique," J. Appl. Phys. **112** 103105 (2012).

13. C. Jensen, C. Xing, C. Folsom, H. Ban, and J. Phillips, "Design and Validation of a High-Temperature Comparative Thermal-Conductivity Measurement System," Int. J. Thermophys., **33** 311 (2012).

14. C. Xing, C. Jensen, H. Ban, and J. Phillips, "Uncertainty Analysis on the Design of Thermal Conductivity Measurement by a Guarded Cut-Bar Technique," Meas. Sci. Technol. **22** 075702 (2011).

PEER-REVIEWED PAPERS IN PROCEEDINGS

1. C. Jensen, C. Xing, H. Ban, C. Barnes, and J. Phillips, "Validation of a Thermal Conductivity Measurement System for Fuel Compacts," Proceedings of the 8th ASME/JSME Thermal Engineering Joint Conference, Honolulu, HI, USA, March 2011.

2. C. Jensen, C. Xing, H. Ban, C. Barnes, and J. Phillips, "A Thermal Conductivity Measurement System for Fuel Compacts," Proceedings of the International Mechanical Engineering Congress and Exposition, Vancouver, British Columbia, Canada, Nov. 2010.

3. C. Xing, C. Jensen, H. Ban, R. Mariani, and J.R. Kennedy, "An Electromotive Force Measurement System for Alloy Fuels," Proceedings of the International Mechanical Engineering Congress and Exposition, Vancouver, British Columbia, Canada, Nov. 2010.

PEER-REVIEWED SUMMARIES IN PROCEEDINGS

1. C. Jensen, M. Chirtoc, J.S. Antoniow, N. Horny, and H. Ban, 2013, "Thermal Wave Techniques for Thermophysical Properties Characterization for Ion-Irradiation Studies," Proceedings of the 2013 ANS Winter Meeting, Washington D.C., USA.

2. C. Jensen, M. Chirtoc, and H. Ban, 2013, "Thermophysical Property Characterization of Nuclear Materials," Proceedings of the 2013 ANS Winter Meeting, Washington D.C., USA.

3. C. Jensen, M. Chirtoc, J.S. Antoniow, N. Horny, and H. Ban, 2013, "Photothermal Radiometry and Scanning Thermal Microscopy for In-depth Thermal Conductivity Characterization of Proton-Irradiated ZrC," Proceedings of the 2013 Annual ANS Meeting, Atlanta, GA, USA.

4. C. Folsom, C. Xing, C. Jensen, and H. Ban, 2013, "Numerical Modeling of the TRISO Fuel Effective Thermal Conductivity," Proceedings of the 2013 Annual ANS Meeting, Atlanta, GA, USA.

5. C. Folsom, C. Xing, C. Jensen, H. Ban, and D. Marshall, 2012, "Effective Thermal Conductivity of TRISO Fuel Compacts," Proceedings of the 2012 ANS Winter Meeting, San Diego, CA, USA.

6. C. Jensen, C. Xing, H. Ban, and J. Phillips, 2011, "Finite Element Analysis for the TRISO Fuel Compact Thermal Conductivity Measurement System," Proceedings of the 2011 Annual ANS Meeting, Hollywood, FL, USA.

7. C. Xing, C. Jensen, H. Ban, and J. Phillips, 2011, "Experimental Error Evaluation of a Thermal Conductivity Measurement System for TRISO Fuel Compacts," Proceedings of the 2011 Annual ANS Meeting, Hollywood, FL, USA.

8. C. Jensen, C. Xing, H. Ban, C. Barnes, and J. Phillips, 2010, "Thermal Conductivity of Surrogate TRISO Fuel Compacts," Proceedings of the 2010 ANS Winter Meeting and Nuclear Technology Expo, Las Vegas, NV, USA.

9. C. Jensen, C. Xing, H. Ban, C. Barnes, and J. Phillips, 2010, "A Thermal Conductivity Measurement System for TRISO Fuel Compacts," Proceedings of the 2010 Annual ANS Meeting, San Diego, CA, USA.

CONFERENCE ABSTRACTS

1. T. Munro, C. Xing, C. Jensen, C. Copeland, H. Ban, and R. Lewis, "Characterizing Thermal Diffusivity of Synthetic Spider Silk using Improved Transient Electrothermal Technique," Nanotech 2013, Washington D.C., USA, May 12-16, 2013.

2. C. Xing, T. Munro, C. Jensen, and H. Ban, "Parametric Study on the Effect of Radiation Heat Loss and Non-Constant Heating in the Electrothermal Technique for Thermal Property Measurement of Micro/Nanoscale Fibers," Nanotech 2013, Washington D.C., USA, May 12-16, 2013.

3. C. Jensen, M. Chirtoc, J.S. Antoniow, N. Horny, and H. Ban, "Thermal Microscopy for Sub-Micron Characterization of Material Thermal Conductivity," 8th Annual NanoUtah Nanotechnology Conference & Exhibition, Salt Lake City, UT, USA, October 11-12, 2012.

4. C. Jensen, M. Chirtoc, J.S. Antoniow, N. Horny, and H. Ban, "Complementary Scanning Thermal Microscopy and Photothermal Radiometry Depth Profiling of Thermal Conductivity in Ion-Irradiated ZrC," Phonons & Fluctuations 3 Workshop, Sant Feliu de Guixols, Girona, Spain, May 21-24, 2012.

5. C. Jensen, M. Chirtoc, J.S. Antoniow, N. Horny, and H. Ban, "Thermal Conductivity of Proton-Irradiated ZrC using Scanning Thermal Microscopy and Photothermal Radiometry," 2nd Mediterranean International Workshop on Photoacoustic & Photothermal Phenomena, Erice, Italy, April 19-26, 2012.

6. M. Chirtoc, L. Thiery, J.F. Henry, J.S. Antoniow, C. Jensen, J. Bodzenta, J. Juszczyk, H. Ban, and B. Cretin, "Comparison of Microthermocouple, Resistive Wire and Thin Film Thermal Probes for ac Scanning Thermal Microscopy," 17th Workshop on Photoacoustics and Thermal Wave Methods, Szczyrk , Poland, February 27-March 2, 2012.

7. C. Jensen, M. Chirtoc, J.S. Antoniow, N. Horny, and H. Ban, "Thermophysical Properties Characterization of Proton-Irradiated ZrC using Scanning Thermal Microscopy and Photothermal Radiometry," 17th Workshop on Photoacoustics and Thermal Wave Methods, Szczyrk , Poland, February 27-March 2, 2012.

DOE REPORTS

1. C. Jensen, C. Xing, C. Folsom, H. Ban, and J. Phillips, "TRISO Fuel Compact Thermal Conductivity Measurement Development," INL/MIS-09-16998, (2011).

2. C. Jensen, C. Xing, H. Ban, J. Phillips, and C. Barnes, "TRISO Fuel Compact Thermal Conductivity Measurement Development," INL/EXT-10-19227, (2010).

3. C. Xing, C. Jensen, H. Ban, R. Mariani, and J.R. Kennedy, "Electromotive Force Measurement," DOE, (2010).

4. C. Jensen, H. Ban, and J.R. Kennedy, "TRISO Fuel Thermal Conductivity Measurement," DOE/INL, (2008).

INVITED TALKS

1. C. Jensen and H. Ban, "Multiscaled Measurement Techniques for Thermophysical Characterization," Dept. of Mech. & Energy Engineering, University of North Texas, Denton, Texas, June 21, 2013.

2. C. Jensen, M. Chirtoc, N. Horny, J.S. Antoniow, C. Xing, and H. Ban, "Thermal Wave Methods for Thermal Conductivity Profile Determination in Proton-Irradiated ZrC," European Commission joint Research CeInstitute for Transuranium Elements, Karlsruhe, Germany, July 16, 2012.

3. M. Chirtoc, N. Horny, J.S. Antoniow, J.F. Henry, J. Randrianalisoa, Ph. Grossel, C. Jensen, and H. Ban, "Combined Scanning Thermal Microscopy Photothermal Radiometry and 3ω Hot Wire Approaches to Heat Transport Characterization at Interfaces," Phonons & Fluctuations 3 Workshop, Sant Feliu de Guixols, Girona, Spain, May 21-24, 2012.

4. M. Chirtoc, L. Thiery, J.F. Henry, J.S. Antoniow, B. Cretin, J. Bodzenta, J. Juszcyk, C. Jensen, and H. Ban, "Thermophysical Properties Characterization of Proton-Irradiated ZrC using Scanning Thermal Microscopy and Photothermal Radiometry," 17th Workshop on Photoacoustics and Thermal Wave Methods, Szczyrk , Poland, February 28, 2012.

5. C. Jensen, M. Chirtoc, J.S. Antoniow, N. Horny, and H. Ban, "Comparison of Microthermocouple, Resistive Wire and Thin Film Thermal Probes for Scanning Thermal Microscopy in Active Mode," 17th Workshop on Photoacoustics and Thermal Wave Methods, Szczyrk , Poland, February 28, 2012.

6. C. Jensen, C. Xing, H. Ban, and J. Phillips, "Thermal Conductivity Measurement System for TRISO Fuel Compacts," 4th Annual Very High Temperature Reactor (VHTR) R&D Technical Review Meeting, Albuquerque, NM, USA, April 26, 2011.

OTHER PROFESSIONAL PRESENTATIONS

Oral Presentations

1. Thermal Wave Techniques for Thermophysical Properties Characterization for Ion-Irradiation Studies
    - 2013 ANS Winter Meeting, Washington D.C., USA, November 14, 2013.

2. Thermophysical Property Characterization of Nuclear Materials
    - 2013 ANS Winter Meeting, Washington D.C., USA, November 14, 2013.

3. Photothermal Radiometry and Scanning Thermal Microscopy for In-depth Thermal Conductivity Characterization of Proton-Irradiated ZrC
    - 2013 ANS Annual Meeting, Atlanta, GA, USA, June 17, 2013.

4. Thermal Conductivity of Proton-Irradiated ZrC using Scanning Thermal Microscopy and Photothermal Radiometry
    - 2nd Mediterranean International Workshop on Photoacoustic & Photothermal Phenomena, Erice, Italy, April 19, 2012.

5. Finite Element Analysis for the TRISO Fuel Compact Thermal Conductivity Measurement System
    - 2011 ANS Annual Meeting, Hollywood, FL, USA, June 29, 2011.

6. Validation of a Thermal Conductivity Measurement System for Fuel Compacts
    - 8th ASME/JSME Thermal Engineering Joint Conference, Honolulu, HI, USA, March 2011.

7. A Thermal Conductivity Measurement System for Fuel Compacts
    - International Mechanical Engineering Congress and Exposition, Vancouver, British Columbia, Canada, November 14, 2010.

8. Thermal Conductivity of Surrogate TRISO Fuel Compacts
    - 2010 ANS Winter Meeting and Nuclear Technology Expo, Las Vegas, NV, USA, November 7, 2010.

9. Thermal Conductivity of TRISO Fuel Compacts.
    - The 13th Annual Intermountain Graduate Research Symposium of 2010, Logan, Utah, USA, March 31, 2010.

10. Bulk Thermal Conductivity Measurement of TRISO Fuel Compacts.
    - The 12th Annual Intermountain Graduate Research Symposium of 2009, Logan, Utah, USA, April 3, 2009.

Poster Presentations

1. In-Depth Thermal Conductivity Profile of Ion-Irradiated Materials using a Multiscaled Approach
    - UNLV/USU Mini-Symposium on Biotechnology, Energy, and Materials, May 6, 2014

2. Scanning Thermal Microscopy and Photothermal Radiometry for Thermal Transport Characterization in Ion-Irradiated Materials
    - NSF ICMR Summer School on Materials in 3D: Modeling and Imaging at Multiple Length Scales, August 19-30, 2013

3. Thermal Microscopy for Sub-Micron Characterization of Material Thermal Conductivity
    - 8th Annual NanoUtah Nanotechnology Conference & Exhibition, Salt Lake City, UT, USA, Oct 11-12, 2012.

4. Complementary Scanning Thermal Microscopy and Photothermal Radiometry Depth Profiling of Thermal Conductivity in Ion-Irradiated ZrC
    - Phonons & Fluctuations 3 Workshop, Sant Feliu de Guixols, Girona, Spain, May 21-24, 2012.

5. A Thermal Conductivity Measurement System for TRISO Fuel Compacts
    - 2010 ANS Annual Meeting, San Diego, CA, USA, June 16, 2010.

6. Thermal Conductivity of TRISO Fuel Compacts.
    - The 13th Annual Intermountain Graduate Research Symposium of 2010, Logan, Utah, USA, March 31, 2010.

PROFESSIONAL SUMMER SCHOOLS AND WORKSHOPS ATTENDED

Aug. 2013 NSF ICMR Summer School Santa Barbara, CA
Materials in 3D: Modeling and Imaging at Multiple Length Scales
(Competetive Application)

Feb. 2013 Grant Writers' Seminars & Workshops Logan, UT
Getting Started as a Successful Proposal Writer and Academician Workshop

June 2011 Center for Material Science of Nuclear Fuel Summer School Idaho Falls, ID
Microstructural Development in Systems exposed to Extreme Environments

PROFESSIONAL SOCIETY ACTIVITIES & SERVICES

Membership
- American Society of Mechanical Engineers (ASME)
- American Nuclear Society (ANS)

Leadership
- **Founder & President** of the USU Student Section of the American Nuclear Society 2012-2013
- Led foundation of the student section at USU to a formal petition and official ANS status
- Organized engineering outreach tours and displays
- Served on Engineering leadership council helping plan student events throughout the year

Reviewer
- Applied Thermal Engineering (primary reviewer)
- Journal of Thermophysics and Heat Transfer (primary reviewer)
- Review of Scientific Instruments (primary reviewer)
- Thermochimica Acta (primary reviewer)
- Journal of Fluids
- ASME IMECE 2013

SPOKEN LANGUAGES

Spanish (Fluent) / French (Learning)